UC San Diego

UC San Diego Electronic Theses and Dissertations

Title

Atmospheric Noble Gases As Geochemical Tracers In The Earth System

Permalink

https://escholarship.org/uc/item/1m2643q7

Author

Birner, Benjamin

Publication Date

2020

Peer reviewed|Thesis/dissertation

eScholarship.org Powered by the California Digital Library
University of California

UNIVERSITY OF CALIFORNIA SAN DIEGO

Atmospheric Noble Gases As Geochemical Tracers In The Earth System

A dissertation submitted in partial satisfaction of the
requirements for the degree
Doctor of Philosophy

in

Earth Sciences

by

Benjamin Birner

Committee in charge:

Professor Ralph Keeling, Co-Chair
Professor Jeff Severinghaus, Co-Chair
Professor Ian Eisenman
Professor Sarah Purkey
Professor Mark Thiemens
Professor Shang-Ping Xie

2020

Copyright
Benjamin Birner, 2020
All rights reserved.

The dissertation of Benjamin Birner is approved, and it is acceptable in quality and form for publication on microfilm:

_____

_____

_____

_____

_____
Co-Chair

_____
Co-Chair

University of California San Diego

2020

DEDICATION

To my family and in memory of Ernst Birner who always believed in me and made sure I never forget life is for living.

TABLE OF CONTENTS

Signature Page iii

Dedication iv

Table of Contents v

List of Figures viii

List of Tables x

Acknowledgements xi

Vita and Publications xiii

Abstract xiv

Introduction 1

Chapter 1 The influence of layering and barometric pumping on firn air transport in a 2-D model 7

1.1 Abstract 7

1.2 Introduction 8

1.3 Methods 14

1.3.1 Governing equation and firn properties 14

1.3.2 Advection velocity and barometric pumping 16

1.3.3 Firn layering 17

1.3.4 Dispersive mixing 18

1.3.5 Molecular diffusion 19

1.3.6 Thermal fractionation and temperature model . . . 21

1.4 Results 22

1.4.1 WAIS Divide 22

1.4.2 Law Dome DSSW20K 28

Law Dome DSSW20K 28

1.5 Discussion 30

1.5.1 Differential kinetic isotope fractionation 30

1.5.2 Diffusive fractionation 35

1.5.3 Predicting disequilibrium 37

1.6 Conclusions . . . 39
1.7 Appendix A: An analytical solution for simplified firn air transport . . . 40
1.8 Appendix B: Differential kinetic isotope fractionation in ratios of two different elements . . . 42
1.9 Supplement availability . . . 44
1.10 Acknowledgements . . . 44

Chapter 2 Gravitational separation of Ar/N_2 and age of air in the lowermost stratosphere in airborne observations and a chemical transport model . . . 52
2.1 Abstract . . . 52
2.2 Introduction . . . 53
2.3 Methods . . . 56
2.3.1 Measurements . . . 56
2.3.2 AoA calculation . . . 59
2.3.3 TOMCAT/SLIMCAT model . . . 63
2.3.4 NIES TM model . . . 65
2.4 Results . . . 65
2.4.1 N_2O-AoA calibration . . . 65
2.4.2 The relationship between mean AoA and GS in models and observations . . . 68
2.4.3 GS and AoA in TOMCAT . . . 71
2.5 Discussion . . . 71
2.5.1 Difference between TOMCAT and the NIES TM . . . 71
2.5.2 Estimating mean AoA from observed $\delta(Ar/N_2)$ . . . 73
2.5.3 Future directions . . . 74
2.6 Conclusions . . . 76
2.7 Appendix A: Description of the Markov chain Monte Carlo algorithm . . . 77
2.8 Appendix B: Derivation of Eq. (2.4) from the Maxwell–Stefan equations . . . 79
2.9 Appendix C: Calculating $\delta(Ar/N_2)$ from δ(GST) . . . 84
2.10 Data availability . . . 86
2.11 Supplement availability . . . 87
2.12 Acknowledgements . . . 87

Chapter 3 Measurements of atmospheric He/N_2 as an indicator of fossil fuel extraction and stratospheric circulation . . . 102
3.1 Abstract . . . 102
3.2 Introduction . . . 103
3.2.1 Gravitational fractionation of He/N_2 in the stratosphere . . . 105
3.2.2 Other controls on tropospheric He/N_2 . . . 107
3.3 Methods . . . 110
3.3.1 The Inlet system . . . 110
3.3.2 Continuous-flow gettering . . . 112
3.3.3 Inlet operation . . . 113
3.3.4 Gas handling and sample delivery systems . . . 114
3.4 Results . . . 115
3.4.1 Gettering performance . . . 115
3.4.2 Response time . . . 115
3.4.3 Analytical precision . . . 116
3.5 Discussion . . . 119
3.5.1 Potential applications . . . 120
3.6 Conclusions . . . 124
3.7 Supplement availability . . . 125
3.8 Acknowledgements . . . 125

Chapter 4 Increase in atmospheric He/N_2 from anthropogenic fossil fuel exploitation . . . 134
4.1 Abstract . . . 134
4.2 Introduction . . . 135
4.3 Methods . . . 136
4.3.1 Delta values definition . . . 136
4.3.2 Sampling . . . 136
4.3.3 Summary of analysis methods . . . 138
4.3.4 Helium leakage testing . . . 140
4.3.5 $^4He/N_2$ artifactual fractionation correction . . . 141
4.4 Results and Discussion . . . 142
4.5 Conclusions . . . 147
4.6 Appendix A: supplementary material . . . 148
4.7 Acknowledgements . . . 157

LIST OF FIGURES

Figure 1.1: Layering of firn photographed in a surface pit at WAIS Divide . . 9
Figure 1.2: Schematic depiction of a typical isotope profile in firn 12
Figure 1.3: Firn conditions and modeled velocities profiles at WAIS Divide . 15
Figure 1.4: Components of the velocity field in layered firn 16
Figure 1.5: The CO_2 diffusivity profile at WAIS Divide 20
Figure 1.6: Simulated and observed CO_2 and CH_4 concentrations in the firn at WAIS Divide 23
Figure 1.7: Horizontally averaged $\delta^{15}N$ at WAIS Divide 24
Figure 1.8: Simulated $\delta^{15}N$ in a part of the lock-in zone at WAIS Divide from the 2-D model not including barometric pumping 25
Figure 1.9: Simulated CO_2 and CH_4 concentrations in the firn at Law Dome DSSW20K 29
Figure 1.10: Horizontally averaged $\delta^{15}N$ at Law Dome DSSW20K 30
Figure 1.11: Horizontally averaged isotope ratios at WAIS Divide in the 2-D model including barometric pumping and horizontal layers 31
Figure 1.12: Differential kinetic isotope fractionation profiles for different isotope pairs at WAIS Divide 32
Figure 1.13: The balance of fractionating and non-fractionating mixing at WAIS Divide 34
Figure 1.14: Diffusive fractionation effect at the time of sampling at WAIS Divide on $\delta^{13}C$ of (a) CO_2 and (b) CH_4 36

Figure 2.1: Location and potential temperature of airborne samples 58
Figure 2.2: Derivation of a tropical upper tropospheric reference time series . 61
Figure 2.3: Recalibration of N2O–AoA relationship 67
Figure 2.4: AoA and gravitational fractionation in the lowermost stratosphere in models and observations 69
Figure 2.5: AoA and gravitational fractionation in TOMCAT and the NIES TM 70
Figure 2.6: Annual and zonal means of $\delta(Ar/N_2)$ and AoA 72
Figure 2.7: Annual mean and zonally integrated Ar deficit in TOMCAT . . . 75

Figure 3.1: Schematic depiction of ^4He fluxes to and from the troposphere . . 107
Figure 3.2: Schematic depiction of the flow-stabilizing MS inlet system 111
Figure 3.3: Typical analysis results from the measurement of two high pressure cylinders 113

Figure 3.4: Mass scan of ambient air 115
Figure 3.5: Stacked switching events between SA and ST gas 116
Figure 3.6: Repeat δ(He/M) analysis of two high-pressure cylinders against ambient La Jolla air collected in 2019 117
Figure 3.7: Zero enrichment calibration 118

Figure 4.1: Repeat analysis of the same sample and standard cylinder combination 139
Figure 4.2: Atmospheric $^4He/N_2$ change 143
Figure 4.3: Predicted and observed trend in atmospheric $^3He/^4He$ with 2σ error bars 146
Figure 4.4: Relationship between pressure and the $^4He/N_2$ anomaly 149
Figure 4.5: Uncorrected timeseries of (a) He/N_2, (b) Ar/N_2, (c) O_2/N_2 and (d) CO_2 in our samples 150
Figure 4.6: Relationships between O_2/N_2 anomaly, $^4He/N_2$ anomaly, and Ar/N_2 anomaly 151
Figure 4.7: Cumulative global natural gas emissions 152

LIST OF TABLES

Table 1.1: ϵ' scaling factor in the 2-D model with barometric pumping between different element and isotope ratios from linear regression of ϵ' value pairs at all depths 38

Table 2.1: Molecular diffusion volumes and masses 80
Table 2.2: Characteristic values of variables in Eqs. (2.26) and (2.27). 83

Table 3.1: Processes contributing to variations in the tropospheric and stratospheric $^4He/N_2$ ratio 108
Table 3.2: Observed ion beam intensities 122

Table 4.1: Summary of experimental conditions for helium permeation experiments with high-pressure cylinders 141
Table 4.2: Summary of old air sample information 153

ACKNOWLEDGEMENTS

The five years of my PhD have been made truly special by all the wonderful people around me. Scripps Institution of Oceanography has some of the greatest minds I have ever encountered. Ralph and Jeff, you were outstanding mentors and allowed me the greatest creative freedom to pursue my interests. Your passion and dedication to science greatly inspired me. Ian, you were willing and able to engage with any problem I brought to you, regardless of how far out there it might seem. My other doctoral committee members, you provided great council and were always available when I needed advice. My collaborators, your scientific excellent showed me what it means to be a scientist. Current and former members of the Keeling and Severinghaus lab group, you exemplify why SIO is such a welcoming place. I could always count on you! Ross and Bill, you showed me how to work in a lab and taught me how to think like an engineer. Chris, I could not ask for a better person to brainstorm crazy new designs with. My family, you made sure I would always have something to smile about and not forget to take a break from time to time. My friends, you have gone with me through the good and bad days of pursuing a PhD and many of you have contributed important ideas when I got stuck. You are my family away from home. Without all of you I could not have made it this far!

Chapter 1, in full, is a reprint of the material as it appears in Birner, B., Buizert, C., Wagner, T.J.W., Severinghaus, J.P., 2018. The influence of layering and barometric pumping on firn air transport in a 2-D model. Cryosphere 12, 2021–2037. https://doi.org/10.5194/tc-12-2021-2018.The dissertation author was the primary investigator and author of this paper.

Chapter 2, in full, is a reprint of the material as it appears in Birner, B., Chipperfield, M.P., Morgan, E.J., Stephens, B.B., Linz, M., Feng, W., Wilson, C., Bent, J.D., Wofsy, S.C., Severinghaus, J., Keeling, R.F., 2020. Gravitational separation of Ar/N_2 and age of air in the lowermost stratosphere in airborne observations and a chemical transport model. Atmospheric Chemistry and Physics 1–34.

https://doi.org/https://doi.org/10.5194/acp-2020-95. The dissertation author was the primary investigator and author of this paper.

Chapter 3, in full, has been submitted for publication of the material as it may appear in Birner, B., Paplawsky, W., Severinghaus, J., Keeling, R.F., 2020. Measurements of atmospheric He/N_2 as an indicator of fossil fuel extraction and stratospheric circulation. Atmospheric Measurement Techniques Discussions 1–25. https://doi.org/10.5194/amt-2020-313. The dissertation author was the primary investigator and author of this paper.

Chapter 4, in part, is currently being prepared for publication of the material and is coauthored with Jeffrey Severinghaus, and Ralph Keeling. The dissertation author was the primary investigator and author of this material.

VITA

2014	B. S. in Earth and Space Sciences, Jacobs University Bremen, Germany
2015	M. Phil in Earth Sciences, Kings College, University of Cambridge, UK
2018	M. S. in Oceanography, University of California San Diego, USA
2020	Ph. D. in Earth Sciences, University of California San Diego, USA

ABSTRACT OF THE DISSERTATION

Atmospheric Noble Gases As Geochemical Tracers In The Earth System

by

Benjamin Birner
Doctor of Philosophy in Earth Sciences

University of California San Diego 2020

Professor Ralph Keeling, Co-Chair
Professor Jeff Severinghaus, Co-Chair

Measurements of noble gas in the atmosphere are a powerful tool to study natural and anthropogenic changes in the Earth system. The chemically inert nature of noble gases means that they are only impacted by physical processes, greatly simplifying the interpretation of observations. Furthermore, fast atmospheric mixing intrinsically integrates global signals on time scales beyond one year allowing local records to capture global changes. Air samples can be obtained in a variety of ways including directly from the atmosphere, from reservoirs intentionally archived by humans, or from small bubbles trapped naturally in ancient ice, enabling the reconstruction of atmospheric changes over a wide range of timescales. However, atmospheric noble

gas measurements are challenging because the signals we chase are often small, and analytical methods are still being developed and improved upon.

In four chapters, this dissertation aims to deepen our understanding of noble gases as geochemical tracers and highlights new methods and applications of noble gas analyses. Chapter 1 explores the processes that cause small offsets between atmospheric air and air preserved in ice using a 2-D numerical model of air transport through snow. Chapter 2 demonstrates a connection between atmospheric circulation in the upper atmosphere and the *in-situ* argon-to-nitrogen (Ar/N_2) ratio using samples collected by aircraft. Chapter 3 introduces a novel mass spectrometric technique for the precise measurement of small changes in the atmospheric helium abundance and outlines potential scientific applications. Finally, Chapter 4 builds on Chapter 3 and presents the first record of an atmospheric helium build-up which can be linked directly to anthropogenic fossil fuel activity.

Introduction

Samples of old air can document natural and anthropogenic processes that change the composition of our atmosphere over time. The most well known records of ancient air are from ice cores. Air is trapped in bubbles as snow turns into ice, in which the air is preserved over millennia. More recently, humans have begun to archive air for future study. Scripps Institution of Oceanography is home to an impressive collection of old air stored in high-pressure cylinders. The inherent inertness of noble gases makes them uniquely suitable for long-term preservation in these archives, and ensures that the gases are not affected by biological and chemical phenomena. This makes precise measurements of atmospheric noble gas elemental ratios a unique tracer of physical processes with important climatic implications.

One of the most intriguing applications of atmospheric noble gas measurements is the determination of changes in mean ocean temperature. Ocean temperature is a powerful indicator of climate because about 93% of all excess heat trapped by greenhouse gases is taken up by the ocean (Intergovernmental Panel On Climate Change, 2013). Differences in the solubilities of noble gases in seawater cause small changes in their atmospheric concentrations as the ocean warms or cools, allowing noble gas records to be used as a proxy for ocean temperature. While using noble gases to determine ongoing changes in ocean heat remains challenging due to a poor signal-to-noise ratio, mean ocean temperature reconstructions since the last glacial maximum have been successfully performed with ice core samples (Baggenstos et al.,

2019; Bereiter et al., 2018; Headly and Severinghaus, 2007).

The interpretation of ice core noble gas records is complicated by fractionation processes that occur in the firn column (i.e., the roughly 50–100 m of snow atop an ice sheet). Gravitational fractionation describes the separation of air components under vertical pressure gradients induced by gravity, with enrichment of heavy gases in the higher-pressure region (i.e., closer to Earth). Similarly, temperature gradients can lead to a fractionation of noble gases with an enrichment of heavy noble gases in cold regions. Thermal and gravitational fractionation both occur by molecular diffusion and are therefore only observable in stagnant air, where turbulent mixing is too weak to erase the small gradients set up by diffusion. The firn matrix usually prevents fast air movement and allows air to come very close to gravitational-thermal equilibrium. However, the equilibrium is occasionally disrupted by passing storm systems. Storm-related pressure variability leads to airflow in or out of the firn, called barometric pumping. Barometric pumping produces mixing in the firn and leads to small deviations from the expected equilibrium gradients in noble gases, termed kinetic fractionation (Buizert and Severinghaus, 2016). Thermal, gravitational, and kinetic fractionation obscure the true atmospheric signal in the ice core record and need to be corrected for. Chapter 1 explores these processes in a 2-D firn air transport model to improve our fundamental understanding and investigate the role of horizontal layers in amplifying mixing by barometric pumping. In the stratosphere, gravitational fractionation is the primary cause of observed gradients in noble gas ratios. While mixing in the troposphere is much too strong to allow fractionation, the moderate degree of stratification in the stratosphere allows small vertical and horizontal gradients to emerge which are observable and have been linked to the circulation indicator "age of air" (AoA, i.e., the time air spent since entry into the stratosphere) (Belikov et al., 2019). Previous measurements were made using balloon-sampling systems but were limited in precision because the gravitational signal is easily dwarfed by artifactual fractionation during sampling (Ishidoya et al., 2013, 2008; Sugawara et al., 2018).

In Chapter 2, I use high precision Ar/N_2 data from multiple airborne campaigns to study the relationship between Ar/N_2 and AoA. The observations were successfully replicated in modeling results from the 3-D atmospheric transport model TOMCAT, demonstrating the potential use of Ar/N_2 as a tracer of stratospheric circulation. The validated model will also enable follow-on studies of a potential stratospheric influence on tropospheric noble gas concentrations.

Another noble gas ratio with previously unexplored applications is He/N_2. Tropospheric He/N_2 must be particularly sensitive to stratospheric influence because He is generally more strongly fractionated by gravity than Ar, and He is faster diffusing, allowing it to approach gravitational equilibrium more closely in the stratosphere. In addition, tropospheric He/N_2 is expected to increase over time due to the human extraction and usage of helium-rich fossil fuels (Oliver et al., 1984; Pierson-Wickmann et al., 2001; Sano et al., 1989). However, no He/N_2 measurements have been previously made with sufficient precision to capture either of these processes.

A novel measurement technique for changes in the tropospheric He abundance over time is introduced in Chapter 3. Previously, proxy-measurements of changing He concentrations were made using helium isotopes ($^3He/^4He$), but analyses were fundamentally limited in precision by the great rarity of ^3He (Boucher et al., 2018; Lupton and Evans, 2013; Mabry et al., 2015). The new method instead relies on stabilizing and gettering the flow of air to a mass spectrometer that collects the $^4He^+$ ion beam while switching between a sample and standard gas. As the same amount of air is delivered to the mass spectrometer at any given time, differences in the $^4He^+$ beam are directly related to differences in the He mole fraction of sample and standard gas. The helium mole fraction can then be corrected mathematically for changes in O_2, N_2 and CO_2 to yield He/N_2. This has the advantage that N_2 concentrations in the atmosphere are rather stable, making He/N_2 an accurate and well-measurable indicator of atmospheric He abundance.

Chapter 4 ultimately capitalizes on the methodological advances shown in Chap-

ter 3, and presents a record of the atmospheric ^{4}He build-up using old air samples available at SIO. The samples have been carefully screened for leakage and clearly demonstrate a rise of ∼1.9 per mille in He/N_2 since 1974 that can be attributed to fossil fuel activity. In combination with previous measurements of ^{3}He/^{4}He, which show a near-zero change, the He/N_2 trend furthermore implies a currently unknown additional source of ^{3}He to the atmosphere that warrants further investigation.

References

Baggenstos, D., Häberli, M., Schmitt, J., Shackleton, S. A., Birner, B., Severinghaus, J. P., Kellerhals, T., and Fischer, H.: Earth's radiative imbalance from the Last Glacial Maximum to the present, Proceedings of the National Academy of Sciences of the United States of America, 116, 14 881–14 886, doi:10.1073/pnas.1905447116, 2019.

Belikov, D., Sugawara, S., Ishidoya, S., Hasebe, F., Maksyutov, S., Aoki, S., Morimoto, S., and Nakazawa, T.: Three-dimensional simulation of stratospheric gravitational separation using the NIES global atmospheric tracer transport model, Atmospheric Chemistry and Physics, 19, 5349–5361, doi:10.5194/acp-19-5349-2019, 2019.

Bereiter, B., Shackleton, S., Baggenstos, D., Kawamura, K., and Severinghaus, J.: Mean global ocean temperatures during the last glacial transition, Nature, 553, 39–44, doi:10.1038/nature25152, 2018.

Boucher, C., Marty, B., Zimmermann, L., and Langenfelds, R.: Atmospheric helium isotopic ratio from 1910 to 2016 recorded in stainless steel containers, Geochemical Perspectives Letters, 6, 23–27, doi:10.7185/geochemlet.1804, 2018.

Buizert, C. and Severinghaus, J. P.: Dispersion in deep polar firn driven by synoptic-

scale surface pressure variability, The Cryosphere, 10, 2099–2111, doi:10.5194/tc-2016-148, 2016.

Headly, M. A. and Severinghaus, J. P.: A method to measure Kr/N2 ratios in air bubbles trapped in ice cores and its application in reconstructing past mean ocean temperature, Journal of Geophysical Research, 112, 1–12, doi:10.1029/2006JD008317, 2007.

Intergovernmental Panel On Climate Change: Climate Change 2013: The Physical Science Basis. Contribution of Working Group I to the Fifth Assessment Report of the Intergovernmental Panel on Climate Change, Tech. rep., Cambridge, United Kingdom and New York, NY, USA, doi:10.1017/CBO9781107415324, 2013.

Ishidoya, S., Sugawara, S., Morimoto, S., Aoki, S., and Nakazawa, T.: Gravitational separation of major atmospheric components of nitrogen and oxygen in the stratosphere, Geophysical Research Letters, 35, doi:10.1029/2007GL030456, 2008.

Ishidoya, S., Sugawara, S., Morimoto, S., Aoki, S., Nakazawa, T., Honda, H., and Murayama, S.: Gravitational separation in the stratosphere - A new indicator of atmospheric circulation, Atmospheric Chemistry and Physics, 13, 8787–8796, doi:10.5194/acp-13-8787-2013, 2013.

Lupton, J. and Evans, L.: Changes in the atmospheric helium isotope ratio over the past 40 years, Geophysical Research Letters, 40, 6271–6275, doi:10.1002/2013GL057681, 2013.

Mabry, J. C., Lan, T., Boucher, C., Burnard, P. G., Brennwald, M. S., Langenfelds, R., and Marty, B.: No evidence for change of the atmospheric helium isotope composition since 1978 from re-analysis of the Cape Grim Air Archive, Earth and Planetary Science Letters, 428, 134–138, doi:10.1016/j.epsl.2015.07.035, 2015.

Oliver, B. M., Bradley, J. G., and Farrar IV, H.: Helium concentration in the Earth's lower atmosphere, Geochimica et Cosmochimica Acta, 48, 1759–1767, doi:10.1016/0016-7037(84)90030-9, 1984.

Pierson-Wickmann, A. C., Marty, B., and Ploquin, A.: Helium trapped in historical slags: A search for temporal variation of the He isotopic composition of air, Earth and Planetary Science Letters, 194, 165–175, doi:10.1016/S0012-821X(01)00554-4, 2001.

Sano, Y., Wakita, H., Makide, Y., and Tominaga, T.: A ten-year decrease in the atmospheric helium isotope ratio possibly caused by human activity, Geophysical Research Letters, 16, 1371–1374, doi:10.1029/GL016i012p01371, 1989.

Sugawara, S., Ishidoya, S., Aoki, S., Morimoto, S., Nakazawa, T., Toyoda, S., Inai, Y., Hasebe, F., Ikeda, C., Honda, H., Goto, D., and Putri, F. A.: Age and gravitational separation of the stratospheric air over Indonesia, Atmospheric Chemistry and Physics, 18, 1819–1833, doi:10.5194/acp-18-1819-2018, 2018.

Chapter 1

The influence of layering and barometric pumping on firn air transport in a 2-D model

1.1 Abstract

Ancient air trapped in ice core bubbles has been paramount to developing our understanding of past climate and atmospheric composition. Before air bubbles become isolated in ice, the atmospheric signal is altered in the firn column by transport processes such as advection and diffusion. However, the influence of low permeability layers and barometric pumping (driven by surface pressure variability) on firn air transport is not well understood and cannot be captured in conventional 1-dimensional firn air models. Here we present a 2-dimensional (2-D) trace gas advection-diffusion-dispersion model that accounts for discontinuous horizontal layers of reduced permeability. We find that layering or barometric pumping individually yield too small a reduction in gravitational settling to match observations. In contrast, when both effects are active, the model's gravitational fractionation is suppressed as observed.

Layering focuses airflows in certain regions in the 2-D model which acts to amplify the dispersive mixing resulting from barometric pumping. Hence, the representation of both factors is needed to obtain a realistic emergence of the lock-in zone. In contrast to expectations, we find that the addition of barometric pumping in the layered 2-D model does not substantially change the differential kinetic fractionation of fast and slow diffusing trace gases. However, like 1-D models, the 2-D model substantially underestimates the amount of differential kinetic fractionation seen in actual observations, suggesting that further subgrid-scale processes may be missing in the current generation of firn air transport models. In spite of this deficiency, we find robust scaling relationships between kinetic isotope fractionation of different noble gas isotope and elemental ratios. These relationships may be used to correct for kinetic fractionation in future high precision ice core studies and can amount to a bias of up to 0.45 °C in noble gas based mean ocean temperature reconstructions at WAIS Divide, Antarctica.

1.2 Introduction

In the upper 50–130 m of consolidated snow above an ice sheet, known as the firn layer, atmospheric gases gradually become entrapped in occluded pores and are eventually preserved as bubbles in the ice below. Antarctic ice core records containing these trapped gases have been critical in informing our understanding of the interplay of past climate and atmospheric trace gas variability over the past 800,000 years (Petit et al., 1999; Lüthi et al., 2008). As atmospheric gases migrate through the firn, they are modified in elemental composition and isotopic signatures by several competing physical processes (Schwander et al., 1988, 1993; Trudinger et al., 1997; Buizert et al., 2012; Kawamura et al., 2013; Mitchell et al., 2015). Therefore, appropriate corrections must be applied to firn and ice core records to accurately reconstruct atmospheric trace gas histories.

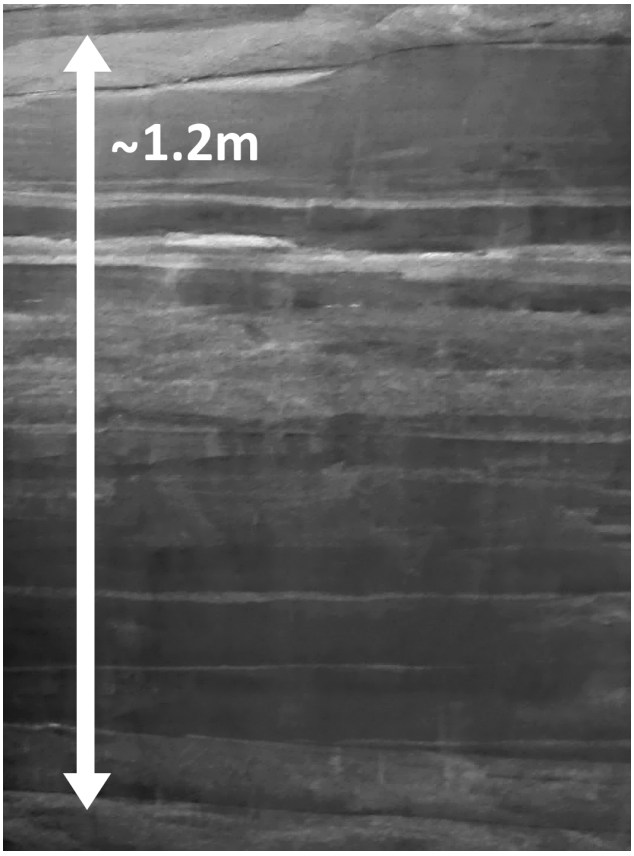

Figure 1.1: Layering of firn photographed in a surface pit at WAIS Divide. Image courtesy of Anaïs Orsi.

Firn is a layered medium, in which the denser layers can impede vertical diffusion and transport (Hörhold et al., 2012; Mitchell et al., 2015; Orsi et al., 2015) (Fig. 1.1). The significance of these layers for firn gas transport remains unclear and motivates this work. Readers who are familiar with the structure of firn and its air transport processes may wish to skip ahead to the last paragraph of this section. To build some intuition about firn transport processes, a simple analytical model of firn air transport is provided in Appendix A.

Box 1.1| Porous media terminology

Porosity: the fraction of (firn) volume filled by gas

Permeability: the degree to which a porous medium permits viscous flow to pass through

Fickian diffusion: molecular diffusion that is proportional to the concentration gradient as described by Fick's first law

Tortuosity: measure of the twistedness of pathways through a porous medium

We distinguish four main processes affecting the composition of air in firn: diffusion, advection, dispersion and convective mixing. Molecular diffusion, driven by concentration gradients in the firn, is the primary mode of horizontal and vertical transport. Molecular diffusion also enables gravitational fractionation, or "settling", of trace gases in proportion to their masses (Schwander, 1989; Sowers et al., 1989; Schwander et al., 1993; Trudinger et al., 1997). Gravitational settling leads to an enrichment of heavy isotopes with depth that is described in equilibrium by the barometric equation (Schwander, 1989; Sowers et al., 1989; Craig et al., 1988):

$$\delta_{grav} = \left[\exp\left(\frac{g\Delta m}{RT}z\right) - 1\right] \times 1000 \text{ per mille}, \tag{1.1}$$

where $\delta \equiv \frac{r_{sample}}{r_{standard}} - 1 \equiv q - 1$, with r being the isotope ratio (unitless), z the depth (m), T the absolute temperature (K), Δm the isotope mass difference (kg mol^{-1}), g the gravitational acceleration (m s^{-2}), and R the fundamental gas constant (J mol^{-1} K^{-1}).

Gradual accumulation of snow and air bubble trapping leads to a slow, downward advection of the enclosed air. The net air advection velocity is slower than the snow accumulation rate (yet still downward in the horizontal average in an Eulerian framework) because compression of the porous firn medium produces a flow of air upward relative to the firn matrix (Rommelaere et al., 1997).

Buoyancy-driven convection and brief pressure anomalies associated with wind

blowing over an irregular topography cause strong mixing between the near-surface firn and the unfractionated atmosphere, smoothing concentration gradients (Colbeck, 1989; Severinghaus et al., 2010; Kawamura et al., 2013). This mixing causes substantial deviations from the gravitational settling equilibrium (i.e., the solution to Eq. (1.1)) and leads to varying degrees of kinetic isotope fractionation because faster diffusing isotopes more readily return to thermal-gravitational equilibrium by diffusion (Buizert et al., 2012; Kawamura et al., 2013).

Lastly, surface barometric pressure variability on longer timescales (>1 hour) drives air movement down to the firn-ice transition. Building on work by Schwander et al. (1988), Buizert and Severinghaus (2016) suggest that surface pressure variability may produce significant pressure gradients in the firn that induce airflow. Porous firn has a high tortuosity, i.e., two points are typically connected by strongly curved paths, and the deep firn also contains many cul-de-sacs (Buizert and Severinghaus, 2016), their Fig. 2). Airflow through such a medium produces mass-independent, dispersive mixing. Dispersion in this context is an emergent macroscopic phenomenon that describes microscopic velocity deviations from Darcy's law of bulk fluid flow in different pores. This process may be accounted for by adding a dispersive mixing term to the advection-diffusion equation traditionally used for trace gas transport in firn (e.g., Buizert and Severinghaus, 2016).

Together, these four processes yield a firn column that is split into a surface mixed zone (SMZ, which has historically been labelled the convective zone), a diffusive zone (DZ) and a lock-in zone (LIZ) (Fig. 1.2). The close-off depth (COD) occurs where the air content becomes fixed and pressure in open porosity increases above hydrostatic pressure. We prefer the term "surface mixed zone" over the more commonly used terminology "convective zone" to acknowledge the dual nature of mixing driven by convection and high-frequency pressure variability in this region. The SMZ is rather well-mixed with a trace gas composition similar to the atmosphere. Nevertheless, large seasonal thermal gradients can lead to isotopic fractionation which is

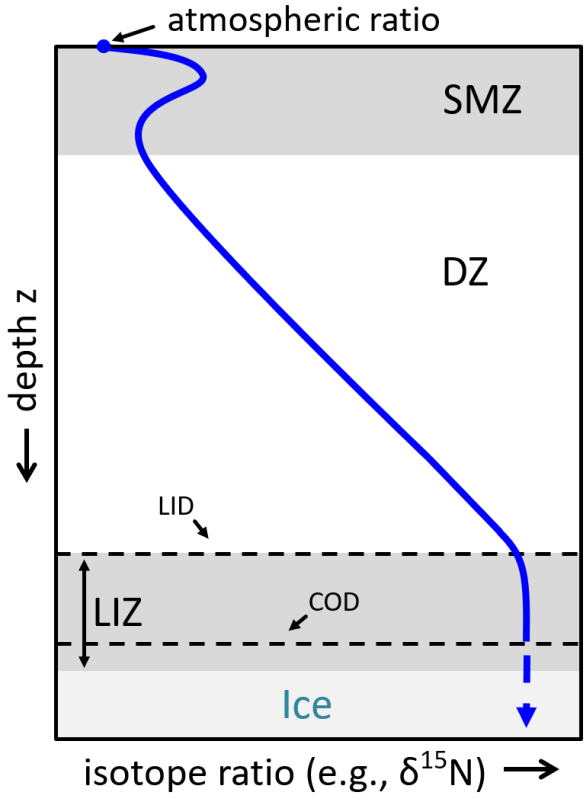

Figure 1.2: Schematic depiction of a typical isotope profile. The surface mixed zone (SMZ), the diffusive zone (DZ), the lock-in zone (LIZ) and the ice below are indicated by shading. Further indicated are the lock-in depth (LID) and the close-off depth (COD) (see text).

only partially attenuated (Severinghaus et al., 2001, 2010; Kawamura et al., 2013). Molecular diffusion dominates in the DZ but effective firn diffusivity decreases with depth due to the increasing influence of tortuosity hindering diffusion. Throughout the DZ, gravitational settling leads to an enrichment of all isotopes heavier than air in proportion to their mass difference. The top of the LIZ, the somewhat poorly defined lock-in depth (LID) horizon, is commonly deduced from a rather sudden change in the slope of the δ ^{15}N, CO_2 or CH_4 profiles. Gravitational enrichment of isotopes ceases in the LIZ and isotope ratios remain constant with depth. We

term any such deviation from gravitational equilibrium "disequilibrium" (without implying that such a situation is not in steady-state).

The physical mechanism responsible for the cessation of gravitational enrichment in the deep firn is still not fully understood. Since CFCs and other anthropogenic tracers have been detected in firn air measurements from the LIZ well below the depth expected from pure advection, it is clear that some amount of vertical transport by molecular diffusion or dispersion continues in the LIZ (Severinghaus et al., 2010; Buizert et al., 2012; Buizert and Severinghaus, 2016). However, no further gravitational settling of isotopes occurs in the LIZ as indicated by constant $\delta\ ^{15}N$ values. Furthermore, the vertical transport in the LIZ appears to be at least to some degree mass- and diffusivity-dependent since the faster diffusing CH_4 advances further in the LIZ than the slower diffusing gases CFC-113 or CO_2 (Buizert et al., 2012). Therefore, transport in the LIZ cannot be explained by either mass-indiscriminate dispersive mixing or molecular diffusion alone. Most current 1-D firn air models use a greatly reduced molecular diffusivity in the lock-in zone and simultaneously introduce a mass-independent mixing term tuned to match measured trace gas profiles (Buizert et al., 2012). A physical mechanism to justify these numerical methods remains elusive. An attempt at a physical explanation was given by Buizert and Severinghaus (2016), who introduced barometric pumping in a 1-D firn model.

Here, we explore the possibility that non-fractionating trace gas mixing in deep firn may be explained by the combination of barometric pumping and discontinuous horizontal layers that have nominal diffusivity. High density layers are empirically linked to low vertical permeability (and thus diffusivity), increasing the firn's tortuosity and forcing extensive horizontal transport. The influence of layering on firn gas transport is mostly untested in numerical models so far since previous firn air models were generally limited to one dimension. In particular, we will test two mechanisms by which density layering could influence isotope ratios in firn air: (i) Layering may reduce gravitational settling of isotopes because vertical settling of iso-

topes is absent during horizontal transport along layers; (ii) Layering may modulate the mass-independent dispersive mixing effect of barometric pumping. Our analyses will focus on two Antarctic high-accumulation sites, WAIS Divide and Law Dome DSSW20K (Trudinger et al., 2002; Battle et al., 2011).

1.3 Methods

1.3.1 Governing equation and firn properties

We model 2-D trace gas transport in firn by numerically solving the advection-diffusion-dispersion equation, known from hydrology (Freeze and Cherry, 1979), adapted to firn (following Schwander et al., 1993; Rommelaere et al., 1997; Trudinger et al., 1997; Severinghaus et al., 2010; Buizert et al., 2012; Kawamura et al., 2013; Buizert and Severinghaus, 2016),

$$\tilde{s}\frac{\partial q}{\partial t} = \nabla \cdot \left[\tilde{s}\mathbf{D}_m \left(\nabla q - \frac{\Delta m \mathbf{g}}{RT} q + \Omega \frac{\partial T}{\partial z} q \hat{\mathbf{k}} \right) + \tilde{s}\mathbf{D}_d \nabla q \right] - (\tilde{s}\mathbf{u}) \cdot \nabla q \qquad (1.2)$$

with $q \equiv \delta + 1$ the ratio of any isotope to $^{28}N_2$ compared to a standard material, $\tilde{s} \equiv s_{op} \exp\left(\frac{\Delta m g}{RT} z\right)$ the pressure-corrected open porosity (m^3 m^{-3}), T temperature (K), Ω thermal diffusion sensitivity (K^{-1}), and $\mathbf{u}$ the advection velocity (m s^{-1}). $\mathbf{D}_m$ and $\mathbf{D}_d$ are the 2-D molecular diffusion and dispersion tensors (m^2 s^{-1}). ∇q is the concentration gradient and $\nabla\cdot$ denotes the 2-D divergence operator. From left to right, the terms of Eq. (1.2) represent the rate of change in concentration/isotope ratio, Fickian diffusion, gravitational fractionation, thermal fractionation, dispersive mixing and advection. Since Eq. (1.2) is only valid for the binary diffusion of a trace gas into a major gas, ratios of any two isotopes of masses x and y are obtained by separately simulating the transport of each isotope into the major gas $^{28}N_2$ and using

the relationship

$$q_{x/y} = \frac{q_{x/28}}{q_{y/28}} \tag{1.3}$$

to calculate the isotope ratios of interest (Severinghaus et al., 2010).

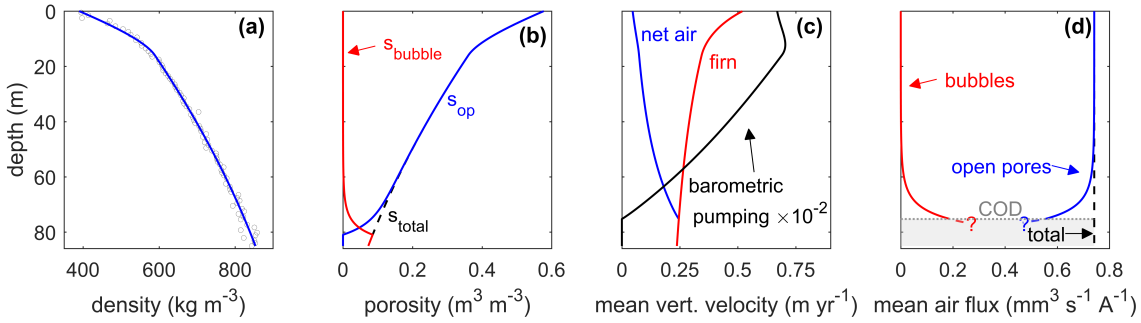

Figure 1.3: Firn conditions and modeled velocities profiles at WAIS Divide. (a) Density fit to observed data (data from Battle et al., 2011); (b) open, bubble (i.e., closed) and total porosity; (c) horizontally averaged barometric pumping velocity (i.e., time-mean horizontal average of $|\mathbf{u}_b|$, black), and horizontally averaged net air velocity ($\mathbf{w}_{firn} + \mathbf{w}_r$, blue) and firn velocity ($\mathbf{w}_{firn}$, red); (d) mean air flux in open pores (blue) and bubbles (red).

Isotope ratios are assumed to be constant at the surface (Dirichlet boundary) and reconstructions of atmospheric CO_2 and CH_4 concentrations over the last 200 years are used to force runs of these anthropogenic tracers (see Supplementary Information (SI)). The model time step is 3.5 days; smaller time steps make the model impractical to run due to computational costs. The bottom boundary is implemented by allowing only the advective flux to leave the domain (Neumann boundary). Diffusion and dispersive mixing cease below the COD. A periodic boundary condition is used in the horizontal direction. The horizontal extent of the model is varied between sites with differing snow accumulation rates to maintain a constant ratio of annual layer thickness to the model's spatial extent, which affects barometric pumping velocity. Firn density (Fig. 1.3a) is prescribed from a fit to the measured density profile at each site. Following Severinghaus et al. (2010) and Kawamura et al. (2013), empirical relationships are used to derive open and closed porosities from the density

profile (Fig. 1.3b). The pressure-corrected open porosity $\tilde{s}$ is assumed to be time independent.

1.3.2 Advection velocity and barometric pumping

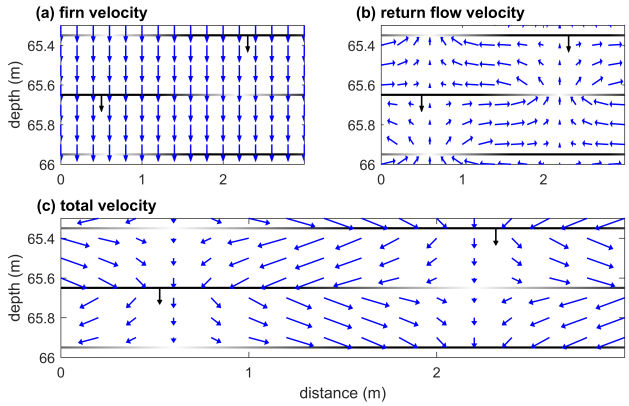

Figure 1.4: The different components of the velocity field. (a) firn velocity; (b) the velocity of air return flow to the atmosphere due to pore compression; (c) net firn air advection velocity (a linear combination of the fields in panels a ad b). Because of its alternating direction, barometric pumping yields no net flow but instantaneous flow field patterns look similar to panel (b). Black arrows indicate the downward advection of layers at the firn velocity.

The 2-D velocity field $\mathbf{u}$ is a result of a combination of (i) air migration with the firn ($\mathbf{w}_{firn}$), (ii) return flow of air from the firn to the atmosphere due to the gradual compression of pores ($\mathbf{u}_r$) , and (iii) airflow resulting from barometric pumping ($\mathbf{u}_b$) (Figs. 1.3c & 1.4). Details on the derivation of these velocities are provided in the SI. In short, $\mathbf{w}_{firn}$ is constrained by assuming a time-constant snow and ice mass flux at all depths. $\mathbf{u}_r$ is calculated based on the effective export flux of air in open and closed pores at the close-off depth (COD), imposing a constant mean vertical air flux throughout the firn column (Fig. 1.3d) (Rommelaere et al., 1997; Severinghaus and Battle, 2006). $\mathbf{u}_b$ is the airflow needed to re-establish hydrostatic balance in the firn in response to any surface pressure anomaly. Surface pressure variability is

represented by (pseudo-) red noise, mimicking observed pressure variability at both sites. The near-coast location Law Dome is more strongly affected by storm activity than WAIS Divide with pressure variability ∼11.2 hPa day^{-1} compared to ∼7 hP day^{-1} at WAIS Divide. $\mathbf{u}_r$ and $\mathbf{u}_b$ follow Darcy's law of flow through porous media (Darcy, 1856):

$$\mathbf{u} = -\frac{\kappa}{\tilde{s}\mu}\nabla P, \tag{1.4}$$

with ∇P the pressure gradient, κ the permeability of firn, and μ the viscosity of air (Fig. 1.4).

1.3.3 Firn layering

Idealized firn layering is implemented by forcing the vertical velocity components u_r and u_b, as well as all vertical diffusive fluxes between the grid boxes on either side of a layer to be zero. Only the advection of air with the firn ($\mathbf{w}_{firn}$) remains active at these grid box boundaries. Layering limits vertical gas migration and yields almost exclusively horizontal transport between layers. We assign layers an infinitesimal thickness because of the computationally limited spatial resolution of the model. Layers are repeatedly introduced at a specific depth and migrate down with the velocity of the firn. The vertical distance between layers is set to correspond to the snow accumulation of one year and the horizontal extent of layers increases linearly with depth until they cover the entire domain at the close-off depth (COD). The mean layer opening size is held proportional to the annual layer thickness to make the vertical advection velocities independent of the arbitrary horizontal extent of the model. To obtain more realistic flow fields, the permeability of layers increases gradually towards both ends of a layer.

1.3.4 Dispersive mixing

The dispersion tensor $\mathbf{D}_d$ is made up of two components, (i) non-fractionating mixing of air in the SMZ and (ii) dispersive mixing caused by barometric pumping in the tortuous firn medium. First, the SMZ is commonly represented by mass-independent ("eddy") diffusion acting in the vertical and horizontal directions. The corresponding diffusivity profile $D_{SMZ}(z)$ is prescribed as an exponential decay away from the snow-atmosphere interface (Kawamura et al., 2013). Its maximum surface value and the decay constant are chosen to match observed δ^{15}N values in the deep firn. After reaching a specified maximum depth of 8 m at WAIS Divide and 14 m at Law Dome DSSW20K, D_{SMZ} tapers linearly to zero over 2 m.

Second, airflow through any dispersive medium leads to mixing in the directions longitudinal and transverse to the flow. Because barometric pumping velocities are orders of magnitude faster than the return flow, dispersive mixing is dominated by barometric pumping. The degree of dispersive mixing in firn presumably depends on the direction of flow and differs between the longitudinal-to-flow and transverse-to-flow direction. However, the treatment of anisotropic media is complex and only one parametrization for vertical, longitudinal-to-flow dispersion in firn is currently available (Buizert and Severinghaus, 2016). Therefore, we assume that the dispersivity α of firn is isotropic and linearly dependent on the magnitude of the flow velocity vector ($v \equiv |\mathbf{u}_b + \mathbf{u}_r|$). In this case, the 2-D dispersion tensor becomes

$$\mathbf{D}_d = (\alpha v + D_{SMZ})\,\mathbf{I}, \tag{1.5}$$

with $\mathbf{I}$ the second order identity matrix (Freeze and Cherry, 1979; Buizert and Severinghaus, 2016). The dispersion flux term in Eq. (1.2) simplifies to

$$\tilde{s}\mathbf{D}_d\nabla q = \tilde{s}\,[\alpha v + D_{SMZ}]\,\nabla q. \tag{1.6}$$

The dispersivity parametrization of Buizert and Severinghaus (2016) is based on direct measurements of cylindrical firn samples from Siple Station, Antarctica, per-

formed by Schwander et al. (1988). The parameterization relates dispersivity to open porosity s_{op} as

$$\alpha\left(s_{op}\right) = \tilde{s}\left[1.26 \cdot \exp\left(-25.7 s_{op}\right)\right]. \tag{1.7}$$

A factor of $\tilde{s}$ was added to the original parameterization by Buizert and Severinghaus (2016) because α relates dispersive mixing to the velocity components u_n and w_n, that denote flow velocities per unit pore cross-section (w_{pores}). Schwander et al. (1988), however, originally measured the considerably slower bulk airflow per unit firn cross-section (i.e., $w_{bulk} = \frac{w_{pores}}{\tilde{s}}$). Since dispersivity is a scale dependent property, it is important to use parameterizations that are compatible with the resolution of the numerical model. The sample size of Schwander et al. (1988) (30 mm diameter & 50 mm length) approximately matches the resolution of our numerical model (30 $\times$ 40 mm) and thus should adequately approximate subgrid-scale (i.e., pore-scale) mixing processes that currently cannot be resolved. Spatial inhomogeneity of subgrid-scale firn dispersivity that was not captured by the sampling of Schwander et al. (1988) cannot be accounted for in the model. Dispersion on larger scales such as the interaction of flow and layers is explicitly represented in the model by the interplay of advection and diffusion. Thus, dispersive mixing is fully constrained in the model and based on empirical parameterizations that are not subject to tuning.

1.3.5 Molecular diffusion

The (effective) molecular diffusivity profile is established by simultaneously fitting the simulated CO_2 and CH_4 profile to real firn measurements at both sites. Effective vertical diffusivity decreases with depth to represent the subgrid-scale effect of decreasing pore connectivity and increasing firn tortuosity, which is not fully represented by the explicit macroscopic layers in our model. A spline function is used to obtain the effective vertical diffusivity profile, which decreases monotonically from the surface to zero at the COD (Fig. 1.5). Diffusivities for other trace

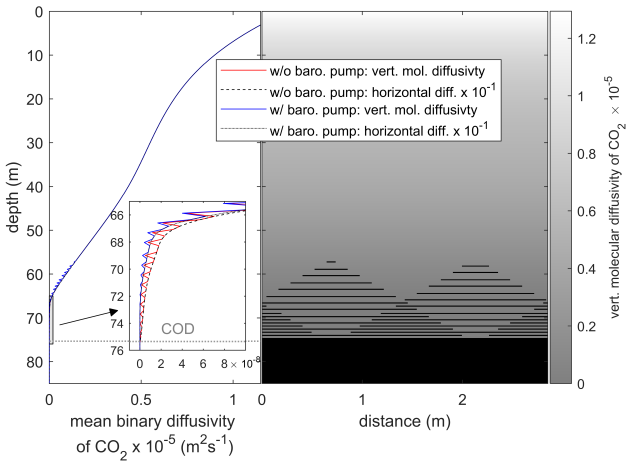

Figure 1.5: The CO_2 diffusivity profile at WAIS Divide. Left panel: Horizontally averaged, vertical and horizontal diffusivity in the model with and without barometric pumping. Right panel: map of diffusivity in the 2-D model without barometric pumping. Only every third layer present in the model is shown here for clarity.

gases are calculated by scaling the tuned CO_2 diffusivity by the free air diffusivity of each gas relative to CO_2 (Trudinger et al., 1997). The diffusivity tuning presents an underconstrained problem because horizontal and vertical molecular diffusivities are essentially free parameters. It is qualitatively evident from firn air sampling that horizontal connectivity/diffusivity is much higher than vertical diffusivity in deep firn, but no satisfactory quantification of this anisotropy is available. As a best guess estimate, we set horizontal molecular diffusivities equal to $10\times$ the vertical diffusivity at the same depth. There are many degrees of freedom in tuning molecular diffusivities and our diffusivity parameterization is therefore not unique. However, sensitivity tests with equal horizontal and vertical diffusivity in the model (compensated by shorter horizontal layers) yield comparable results.

1.3.6 Thermal fractionation and temperature model

Finally, a 1-D vertical thermal model by Alley and Koci (1990) is run separately to simulate the temperature evolution of the firn. The model is forced by a long-term surface temperature trend based on published records by Van Ommen et al. (1999); Dahl-Jensen et al. (1999); Orsi et al. (2012). A mean Antarctic seasonal cycle derived from a ∼8–10-year climatology of automatic weather station observations at WAIS Divide and Law Dome (Lazzara et al., 2012) is superimposed on this trend. Alley and Koci's temperature model is based on the heat transport equation for firn (Johnsen, 1977) with parameterizations for firn thermal properties from (Weller and Schwerdtfeger, 1977). Horizontal temperature gradients in firn are small at both sites and neglected in this study.

Considerable temperature gradients can exist in present-day firn because of recent global atmospheric warming and these gradients can lead to increased isotope thermal fractionation, in particular of δ^{15}N. The sensitivity of isotopes to diffuse in response to temperature gradients is captured by the thermal diffusion sensitivity Ω. The temperature dependence of Ω is approximated as a function of the effective average temperature T in Kelvin:

$$\Omega = \frac{a}{T} - \frac{b}{T^2} \tag{1.8}$$

or Ω is assumed to be temperature independent if the coefficients a and b are unknown for a specific isotope ratio (Severinghaus et al., 2001). Coefficients a and b were determined experimentally for different isotope ratios by Grachev and Severinghaus (2003a,b) and Kawamura et al. (2013).

A table of all model parameters and further details of the numerical realization of 2-D gas transport is provided in the SI.

1.4 Results

1.4.1 WAIS Divide

CO_2 and CH_4

A comparison of simulated and observed CO_2 and CH_4 profiles shows good agreement at WAIS Divide, supporting the plausibility of our layered diffusivity parameterization (Fig. 1.6). In line with observations, both CO_2 and CH_4 concentrations decrease slowly with depth until ∼68 m below the surface due to the gradually increasing gas age and the anthropogenic rise in atmospheric CO_2 and CH_4 concentrations. The more rapid decrease of CO_2 and CH_4 below ∼68 m is explained by a much slower vertical penetration of air and a faster increase of the gas age with depth in the LIZ.

In the following discussion we will examine and compare results from four different versions of the 2-D model: with or without impermeable layers and with activated or deactivated barometric pumping. In versions without layering, our 2-D model loses all horizontal heterogeneity and will thus be referred to as a "1-D model" in what follows. Since the explicitly implemented tortuosity from layering in the 2-D model affects molecular diffusion and dispersion equally it is represented by lowering the effective molecular diffusivity and dispersivity equally in the layered region of the 1-D version instead. Diffusivities are tuned such that the CO_2 profiles are (nearly) identical. The small remaining deviations in CO_2 and CH_4 concentrations between model versions ($< \pm 0.4$ ppm and $< \pm 9$ ppb, respectively) are illustrated in Fig. S12.

δ^{15}N and thermal fractionation

In all four model setups, the seasonal cycle of temperature dominates the shape of the δ^{15}N profiles in the top ∼30 m (Fig. 1.7). Warm summer temperatures drive the migration of heavy isotopes into the colder firn below and produce a δ^{15}N summer

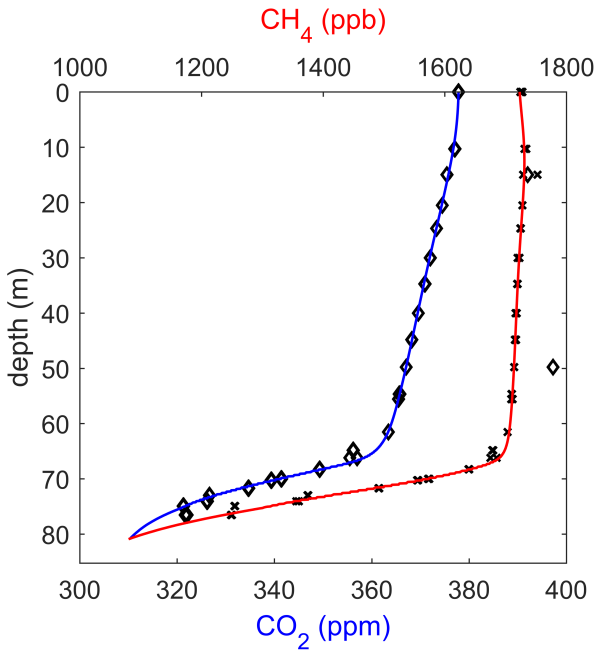

Figure 1.6: Simulated and observed CO_2 and CH_4 concentrations in the firn at WAIS Divide. The model is initialized with the recorded atmospheric trace gas concentrations in 1800 CE at all depths and is forced at the surface with histories of atmospheric CO_2 and CH_4 concentrations (Etheridge et al., 1996, 1998; Keeling et al., 2001; Buizert et al., 2012; Dlugokencky et al., 2016a,b). Markers indicate observed CO_2 (diamonds) and CH_4 (crosses) concentrations (Battle et al., 2011). Based on high CO_2 and CH_4, two samples at ∼15 m and ∼50 m depth were likely compromised by modern air during analysis and are thus ignored in the curve fit. Differences in the CO_2 and CH_4 profiles between the 1-D model and the 2-D model with or without barometric pumping are not visible at the resolution of this figure but are illustrated in the SI (Fig. S12).

peak just below the surface (Severinghaus et al., 2001). In contrast, a minimum of $\delta^{15}N$ occurred in this region during the previous winter season when the thermal gradients were reversed. The remnants of this winter minimum are still visible in the gas record as anomalously low $\delta^{15}N$ values below the summer peak. The differences between observations and simulated $\delta^{15}N$ values in the top of the firn column are likely caused by our idealized representation of the seasonal cycle in the model.

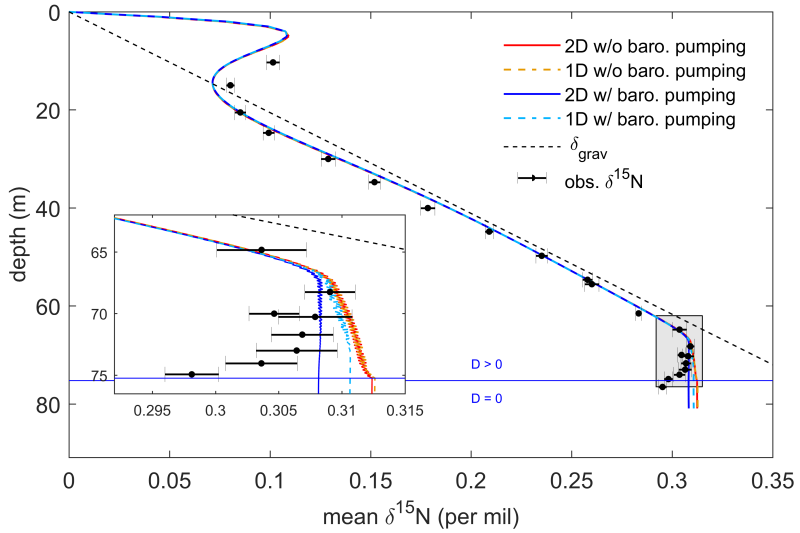

Figure 1.7: Horizontally averaged δ^{15}N at WAIS Divide. Model output is shown from four different versions of the 2-D model (see text). Black circles with error bars indicate the observed firn δ^{15}N (Battle et al., 2011). The dashed black line represents the equilibrium solution for pure gravitational settling (δ_{grav}). The horizontal blue line marks the depth where vertical diffusivity reaches zero. The inset shows a magnification of the lock-in zone.

Impact of reduced-permeability layers

In the layered 2-D model without barometric pumping, the simulated δ^{15}N values are close to observations at the top of the LIZ but continue to increase with depth (Fig. 1.7). This is contradicted by observational data even when the unusually low δ^{15}N values at the COD and below are not taken into consideration (near the COD, firn air sampling becomes more difficult in the field and the potential for fractionation during sampling is increased). A closer inspection of the lock-in zone in Figs. 1.7 and 1.8 reveals a zigzag pattern in the δ^{15}N profile where impermeable layers are present. Simulated isotope ratios are higher just above horizontal layers, where heavy isotopes can accumulate, and are anomalously low below layers where heavy isotopes are more readily removed than supplied by gravitational

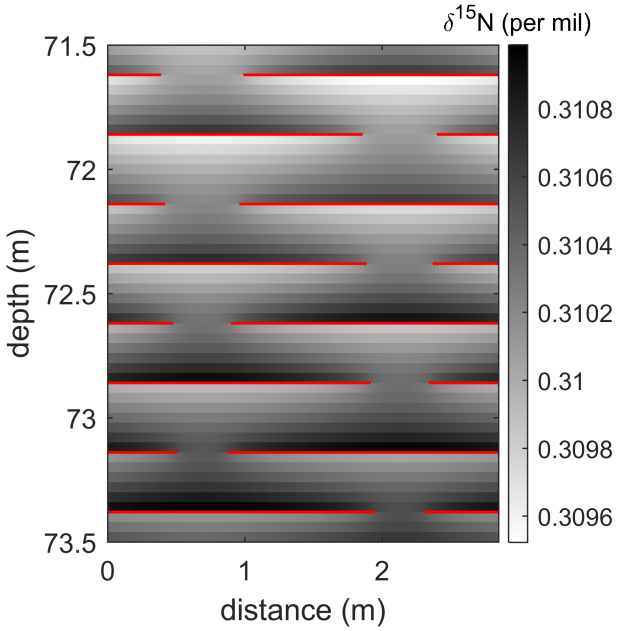

Figure 1.8: Simulated δ^{15}N in a part of the lock-in zone at WAIS Divide from the 2-D model not including barometric pumping. Impermeable horizontal layers are shown in red. The size of the openings in the layers shrink with increasing depth.

settling. Gravitational settling through gaps in the layers sets up small horizontal concentration gradients that drive horizontal Fickian diffusion. Layering increases the effective travel path length for molecules and reduces the effective vertical diffusivity by increasing the tortuosity. However, layering alone appears to be insufficient to prevent gravitational settling completely, with continued gravitational enrichment being observed in the LIZ in this model version.

Is the impact of layers on the firn trace gas profile larger for isotopes such as δ^{15}N than for anthropogenic tracers such as CO_2, CFCs, or CH_4? All three gases have experienced large atmospheric variability in the industrial era. Therefore, the migration of these gases into the firn is dominated by vertical and horizontal Fickian diffusion. For δ^{15}N, on the other hand, the effect of gravity is critical for transport. To answer the above question, we compare output from the layered 2-D model to the

1-D model without layers. We find that δ^{15}N values in the 1-D and 2-D model without barometric pumping are almost identical (Fig. 1.7). Layering in the 2-D model increases the effective transport distance for CO_2 just as much as for δ^{15}N and there is no disproportional impact of layering on gravitationally fractionated isotope ratios. Differences in explicitly represented tortuosity are automatically compensated in the 1-D model during tuning to the same CO_2 profile by reducing molecular diffusivities. Therefore, we conclude that layering alone cannot simultaneously explain the observed CO_2 and δ^{15}N patterns.

Barometric pumping and the emergence of the LIZ

δ^{15}N values simulated by the 1-D and 2-D model with barometric pumping are lower in the LIZ than in both model versions without barometric pumping (Fig. 1.7). Accounting for barometric pumping improves the agreement with observations throughout the lock-in zone. However, the reduction of gravitational fractionation is substantially stronger when layers are present. Only when both layering and barometric pumping are accounted for in the model simultaneously, does the δ^{15}N profile correctly indicate no further gravitational enrichment in the LIZ and match observations more closely. Dispersive mixing is nearly independent of molecular mass and does not lead to gravitational fractionation, but rather acts to eliminate the concentration gradients associated with gravitational settling. Although barometric pumping velocities are largest near the surface (Fig. 1.3c), significant dispersive mixing is generally limited to the LIZ because dispersivity of firn is inversely related to the open porosity in the parameterization of Buizert and Severinghaus (2016) and dispersion is overwhelmed by molecular diffusion in the DZ. Furthermore, molecular diffusivities drop rapidly in the LIZ in the model (Fig. 1.5). Because dispersion provides an additional transport mechanism for trace species, even less molecular diffusion is needed to match observed CO_2 and CH_4 concentrations in the LIZ when barometric pumping is active. Layering amplifies the importance

of barometric pumping because gravitational fractionation between annual layers is restricted into the small gaps in the LIZ (Fig. 1.8). Narrow pathways amplify barometric pumping flow velocities and thus dispersive mixing in these regions (Fig. 1.4), thus overwhelming the influence of gravitational fractionation more readily than in the 1-D model. This effect is responsible for the larger differences between the δ^{15}N profiles obtained from the two model versions with barometric pumping in Fig. 1.7. The strength of dispersive mixing in our layered 2-D model is physically motivated; thus, barometric pumping and layering together lead to a more natural emergence of the δ^{15}N-defined lock-in zone in the 2-D model.

The surface mixed zone depth

We estimate the depth of the SMZ at WAIS Divide to be ∼2.8 m. Multiple different procedures have been used to estimate SMZ thickness in the past, many of which rely on δ^{15}N data in the deep firn near the LIZ (Battle et al., 2011). However, if the deep firn is affected by dispersive mixing due to barometric pumping, these estimates may be falsely attributing some fraction of the dispersive mixing in the deep firn to the SMZ. To address this problem, we follow the method of Severinghaus et al. (2001) in calculating SMZ thickness. This approach compares the depth where δ^{15}N reaches a certain value in two different model configurations with zero and non-zero values of D_{SMZ}. Thermal effects are neglected. The first setup is the 2-D model with barometric pumping as presented above but the dispersivity is set to zero everywhere without retuning the model. The SMZ thickness is calculated from the depth difference between this model run and a second model run where barometric pumping is deactivated, $D_{SMZ} = 0$, and thus only advection and gravitational fractionation shape the profile of δ^{15}N. Our depth estimate of 2.8 m is within the range of values from 1.4 to 5.2 m published previously (Battle et al., 2011).

1.4.2 Law Dome DSSW20K

At Law Dome DSSW20K, the firn thickness is ∼20 m less than at WAIS Divide. Accumulation rates are comparable, but annual-mean temperatures are ∼10 K warmer. The SMZ is slightly deeper and barometric pumping is stronger at Law Dome, yielding more near-surface and dispersive mixing. Constraining the SMZ depth at DSSW20K is more difficult because fewer $\delta^{15}N$ measurements are available for this site, and their associated uncertainty is, at ±15 per meg, much larger than at the more recently sampled WAIS Divide site (Trudinger et al., 2002). Molecular diffusion generally takes a less important role at DSSW20K and molecular diffusivities obtained by tuning are about half or less than those at WAIS Divide for most of the firn column. Thermal fractionation has a weaker impact on the isotope record near the surface at Law Dome due to the smaller amplitude of the seasonal cycle and stronger near-surface mixing compared to WAIS Divide. Figures of molecular diffusivity, advection velocities and other firn properties at site DSSW20K are provided in the SI.

Simultaneously matching the $\delta^{15}N$, CO_2 and CH_4 profile at Law Dome DSSW20K has proven difficult in the past (Trudinger et al., 2002; Buizert and Severinghaus, 2016). Simulated $\delta^{15}N$ in the LIZ is typically substantially higher than in observations. Buizert and Severinghaus (2016) suggested that barometric pumping in the deep firn may be able to reconcile this contradiction. However, the mixing obtained from theoretical predictions was insufficient to achieve a satisfactory fit. Buizert and Severinghaus (2016) hypothesized that firn layering may play a critical role in amplifying the impact of barometric pumping. The authors used an idealized eddy and molecular diffusivity profile in the deep firn to simulate the effect of layers on firn air transport. Using these diffusivity profiles, they were able to obtain good agreement with observed $\delta^{15}N$, CH_4 and $^{14}CO_2$. Our 2-D model includes an explicit representation of layering and places similar physical constraints on barometric pumping as the 1-D model of Buizert and Severinghaus (2016). The model is tuned to optimize agree-

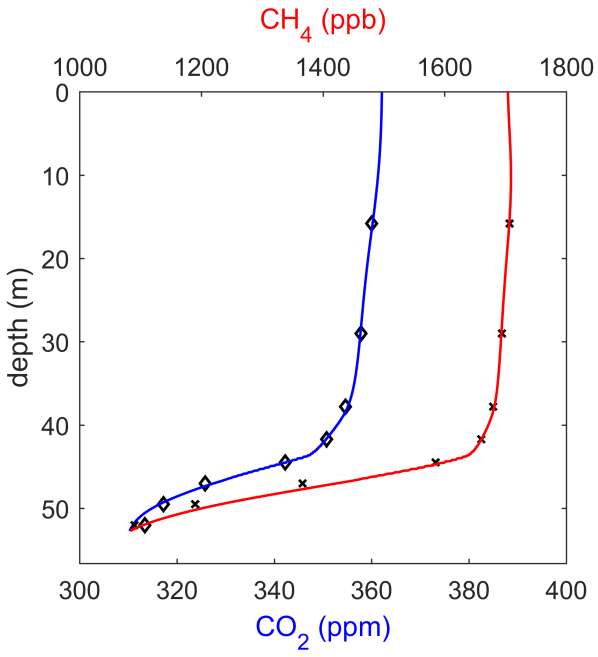

Figure 1.9: Simulated CO_2 and CH_4 concentrations in the firn at Law Dome DSSW20K. The model is forced with histories of atmospheric CO_2 and CH_4 concentrations from 1800 to 1998 CE (the date of sampling). Markers indicate observed CO_2 (diamonds) and CH_4 (crosses) concentrations (Trudinger et al., 2002).

ment with CO_2 and CH_4 and the patterns of both profiles are reproduced correctly (Fig. 1.9). But the disagreement between modeled and observed $\delta^{15}N$ in the deep firn remains despite barometric pumping producing substantial non-fractionating dispersive mixing in the region (Fig. 1.10). Simulated $\delta^{15}N$ values diverge from observations at ∼38 m, where gravitational enrichment seems to stop in observations but continues in the model. In contrast, the LIZ, as defined by CO_2 and CH_4, only starts at roughly 43 m depth. Such an early onset of dispersive mixing is not supported by the dispersivity parameterization. However, only the longitudinal-to-flow mixing in the vertical direction at Siple Station was used to develop the firn dispersivity parameterization, and the use of this parameterization may be inappropriate at Law Dome DSSW20K (Buizert and Severinghaus, 2016). Moreover, dispersivity typically

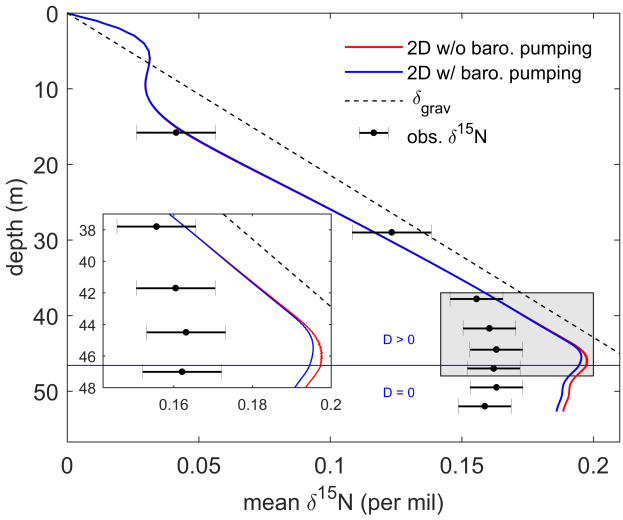

Figure 1.10: Horizontally averaged δ^{15}N at Law Dome DSSW20K. The solid lines show the results of the 2-D model (with layers), for the cases with (blue) and without (red) barometric pumping. Black circles with error bars indicate the observed firn δ^{15}N (Trudinger et al., 2002, 2013). The dashed black line represents the equilibrium solution for pure gravitational settling (δ_{grav}). The horizontal blue line marks the depth where vertical diffusivity reaches zero. The inset shows a magnification of the lock-in zone.

differs in the horizontal and vertical as well as the longitudinal- and the traverse-to-flow directions, an effect that is not accounted for in this study because of a lack of observational evidence to constrain anisotropic dispersivity.

1.5 Discussion

1.5.1 Differential kinetic isotope fractionation

Isotope ratios in firn typically do not reach values as high as predicted from gravitational equilibrium due to the influence of advection and non-fractionating dispersive mixing (Trudinger et al., 1997; Kawamura et al., 2013; Buizert and Severinghaus, 2016). Advection and mass-independent mixing transport less-fractionated air down

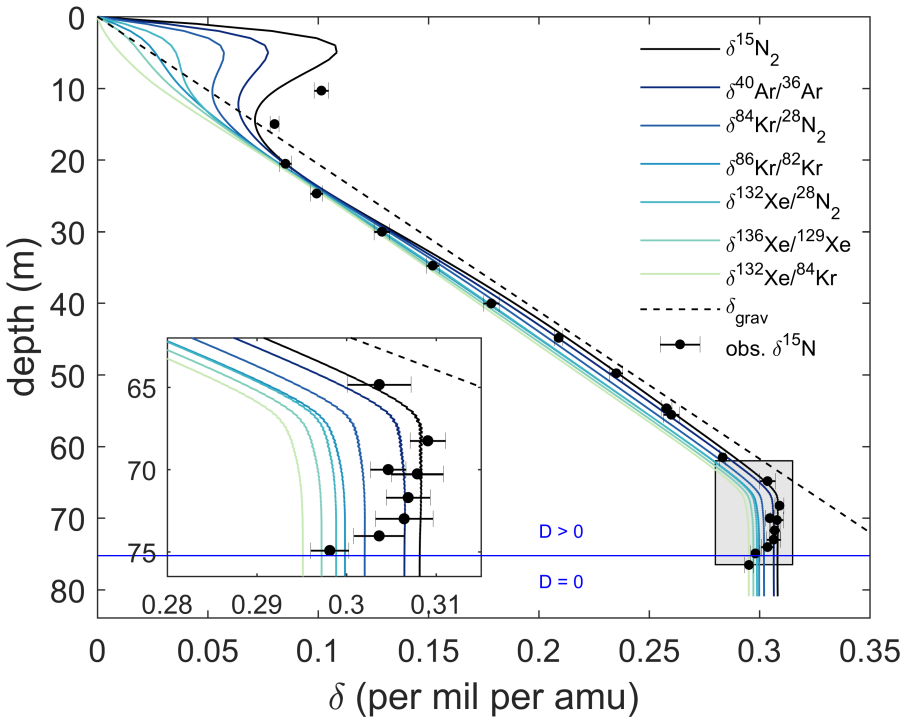

Figure 1.11: Horizontally averaged isotope ratios at WAIS Divide in the 2-D model including barometric pumping and horizontal layers. Isotope ratios are normalized to one atomic mass unit (amu) mass difference (SI). The dashed black line represents the equilibrium solution for pure gravitational settling (δ_{grav}). The horizontal blue line marks the depth where vertical diffusivity reaches zero. Observed δ^{15}N are shown as circles with horizontal error bars (Battle et al., 2011). The inset shows a magnification of the lock-in zone (gray patch).

in the firn column and act to counterbalance the enrichment of heavy isotopes by gravitational fractionation. As a result, all isotope ratios fall below the gravitational settling line δ_{grav} (Fig. 1.11) but the magnitude of the deviation depends on the specific isotope pair.

The magnitude of disequilibrium of different isotope and elemental ratios is quantified here by defining the (mass-normalized) kinetic fractionation ϵ' relative to δ^{15}N

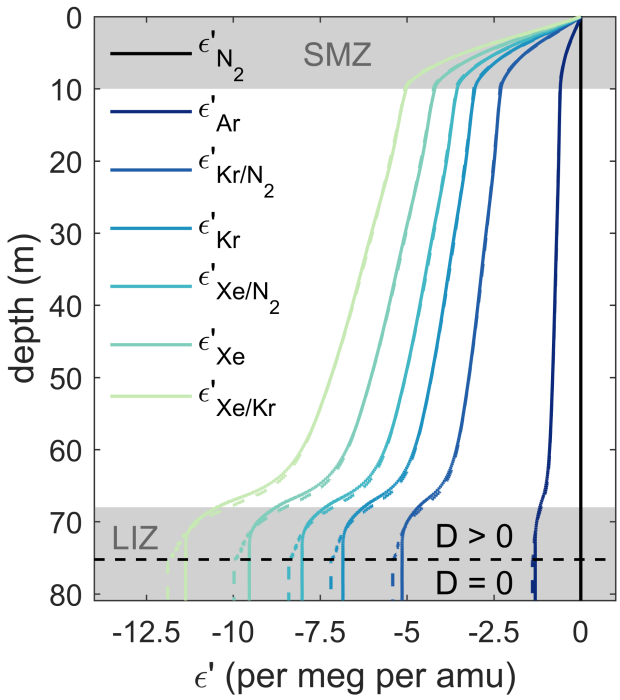

Figure 1.12: Differential kinetic isotope fractionation (ϵ') profiles for different isotope pairs at WAIS Divide. Colored solid and dashed lines show results from the 2-D model with and without barometric pumping, respectively. ϵ' is defined as the (typically negative) difference between any mass-normalized isotope ratio and δ^{15}N (see text). Subscripts of one or two element names identify ratios as isotope or elemental ratios, respectively. The dashed black line highlights where molecular diffusivity in the model reaches zero.

(Kawamura et al., 2013) as

$$\epsilon'_{x/y} \equiv \frac{1}{1000 \times \Delta m_{x/y}} \ln\left(\frac{q_{x/28}}{q_{y/28}}\right) - \ln\left(q_{^{15}N}\right), \tag{1.9}$$

where $\Delta m_{x/y}$ is the mass difference of isotopes x and y. This definition is similar to the ^{86}Kr excess terminology introduced by Buizert and Severinghaus (2016) but ϵ' is given in the more precise $\ln(q)$-notation and uses δ^{15}N as reference instead of δ^{40}Ar/^{36}Ar. To calculate $\epsilon'_{x/y}$, isotope ratios must have been previously corrected for the influence of thermal fractionation either through combined Ar and N_2 isotope

measurements on firn air (Grachev and Severinghaus, 2003a,b) or, as done here, by removing temperature effects with a suitable firn air transport model (Fig. 1.12).

The degree of disequilibrium, represented by ϵ', is caused by differential kinetic isotope fractionation. Heavy, slow-diffusing isotopes approach gravitational equilibrium more slowly than lighter, faster-diffusing isotopes. Therefore, slow-diffusing isotopes experience larger kinetic fractionation (i.e., deviations from gravitational equilibrium) in regimes with non-zero advection or dispersion. Consequently, ϵ' is more negative for heavier, slower diffusing isotopes. On its own, this rule of thumb cannot fully explain the pattern of ratios containing two different elements, such as $^{132}\mathrm{Xe}/^{28}\mathrm{N}_2$. The magnitude of disequilibrium in such mixed-element ratios is further discussed in Appendix B.

In the DZ, ϵ' decreases almost linearly with depth, while within the SMZ and LIZ ϵ' changes much more rapidly. Where molecular diffusivity is zero, ϵ' remains constant. This pattern is explained by the relative importance of advection and dispersive mixing compared to molecular diffusion in different regions of the firn column. The Péclet number (Pe) traditionally quantifies the ratio of the advective to the diffusive transport and is here defined as the ratio of the diffusive to the advective time scale (τ_{D_m} and τ_{adv}). We add the time scale of dispersive mixing (τ_{D_e}) to the numerator because the effect of advection and dispersive mixing on the isotope profiles is very similar although the physics differ (Kawamura et al., 2013).

$$Pe \equiv \frac{\tau_{adv} + \tau_{D_e}}{\tau_{D_m}} \sim \frac{\frac{W}{L} + \frac{D_e}{L^2}}{\frac{D_m}{L^2}} \sim \frac{WL + D_e}{D_m}, \tag{1.10}$$

where $L = 1$ m is the characteristic length scale of firn air transport, and D_m, W and D_e are characteristic values of the molecular diffusivity, the time mean vertical advection velocity, and the vertical dispersive or convective mixing at that depth, respectively.

This modified Péclet number varies in the model by many orders of magnitude through the firn column at WAIS Divide with peak values in the SMZ and the deep

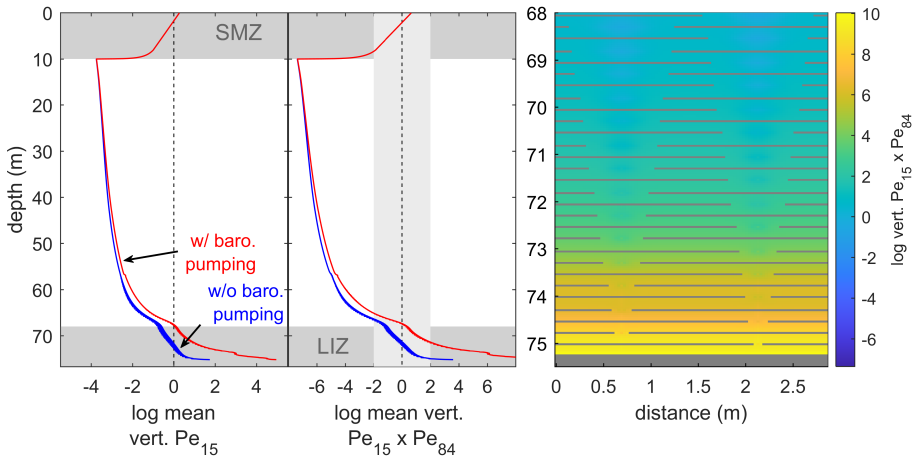

Figure 1.13: The balance of fractionating and non-fractionating mixing at WAIS Divide. The left panel illustrates the horizontally averaged modified Péclet number of δ^{15}N (Pe_{15}, see text). Blue and red lines show results from the 2-D models with and without barometric pumping. The strength of dispersive mixing in the calculations is given by the mean barometric pumping flow velocities at the site. The middle panel displays the product of the modified Péclet numbers for δ^{15}N and $^{84}\mathrm{Kr}/^{28}\mathrm{N}_2$ (Pe_{84}). The region where ϵ' changes with depth should be greatest (i.e., where the product of the modified Péclet numbers is near one) is highlighted by a gray bar. The right panel provides a magnified 2-D map of this Péclet number product in the LIZ.

firn (Fig. 1.13). High modified Péclet numbers in the SMZ are caused primarily by large D_e values, and high modified Péclet numbers in the LIZ are mostly the result of low molecular diffusivities. Kawamura et al. (2013) showed analytically that relative kinetic isotope fractionation depends on the ratio of eddy diffusivity to molecular diffusivity, but the role of advection was neglected due to near-zero accumulation rates at the Megadunes site. The absolute difference in kinetic isotope fractionation (i.e., ϵ') should be greatest when the product of the modified Péclet numbers of both isotopes is near one. In line with these theoretical predictions, we observe almost no further isotopic enrichment of δ^{15}N in the lock-in zone when barometric pumping is included in the model and $Pe \gg 1$ (Figs. 1.7 & 1.13). The largest changes of ϵ' occur in the 2-D model when the product of the modified Péclet numbers is within

approximately 1–2 orders of magnitude of unity. This region is illustrated by the vertical gray bar in Fig. 1.13, which contains the SMZ as well as the beginning of the LIZ where non-fractionating mixing is of similar magnitude as molecular diffusion.

With active barometric pumping and centimeter-scale layering, the product of the modified Péclet numbers at the bottom of the LIZ becomes so large that ϵ' stops to decrease entirely in our model. If barometric pumping is neglected instead, the modified Péclet numbers in the layered 2-D model are considerably lower in the LIZ and some gravitational and kinetic fractionation persists (i.e., δ^{15}N and ϵ' continue to change gradually). Therefore, barometric pumping leads to slightly weaker rather than stronger differential kinetic fractionation at the COD of WAIS Divide in contrast to expectations (Buizert and Severinghaus, 2016). Furthermore, layering and barometric pumping in the model seem to be insufficient to obtain the full ∼5–23 per meg per amu range of ϵ'_{Kr} values measured in the WAIS Divide ice core record (WAIS Divide Project Members, 2015; Bereiter et al., 2018). Instead, other, unresolved (i.e., subgrid-scale) processes may be the reason for the large observed disequilibrium. Establishing a straightforward relationship between disequilibrium and surface pressure variability using firn air models alone may not be possible without more observational data.

1.5.2 Diffusive fractionation

Strong kinetic isotope fractionation can also be observed for trace gases that experience large changes in the atmospheric mixing ratio while the atmospheric isotope ratios remain constant (Trudinger et al., 1997; Buizert et al., 2013). As the concentration of a trace gas increases, isotopologues of the gas migrate into the firn column at different speeds because of small differences in their masses and diffusivities. This results in a relative depletion of the slower diffusing isotopologue with depth called diffusive fractionation (Trudinger et al., 1997). During periods of abrupt CH_4 change,

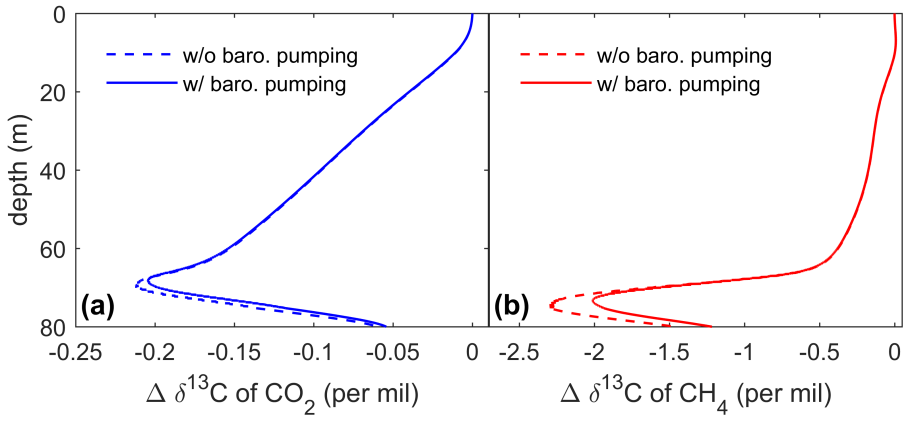

Figure 1.14: Diffusive fractionation effect at the time of sampling at WAIS Divide on δ^{13}C of (a) CO_2 and (b) CH_4. Atmospheric mixing ratios of $^{12}CO_2$, $^{13}CO_2$, $^{12}CH_4$ and $^{13}CH_4$ were obtained from atmospheric trace gas histories used to drive the firn air model (see SI) and assuming constant atmospheric isotope ratios of -8 per mille and -47 per mille for δ^{13}C-CO_2 and δ^{13}C-CH_4, respectively. Firn air values are presented as the difference from the constant atmospheric isotope ratios.

diffusive fractionation commonly amounts to a relevant correction in ice core studies (Trudinger et al., 1997; Buizert et al., 2013). Diffusive fractionation of δ^{13}C-CH_4 is strong, and poorly constrained by models, to the degree that it prohibits the reliable atmospheric reconstruction of this parameter from firn air measurements (Sapart et al., 2013). Since diffusive fractionation is a type of kinetic fractionation, it can be tested in our model. We assume a constant atmospheric $^{13}C/^{12}C$ isotope ratio of 1.1147302 % for CO_2 (i.e., δ^{13}C-CO_2 = -8 per mille) and 1.0709052 % for CH_4 (i.e., δ^{13}C-CH_4 = -47 per mille), respectively. Thermal fractionation and gravitational settling are neglected to isolate the impact of the atmospheric mixing ratio change. The model including barometric pumping calculates δ ^{13}C-CO_2 and δ^{13}C-CH_4 values depleted by up to $\sim$0.2 per mille and $\sim$2 per mille relative to the atmosphere in the WAIS Divide LIZ at the time of firn air sampling (Fig. 1.14). Without barometric pumping, delta values are notably higher because molecular diffusion is stronger, and

the dispersive mixing no longer smooths out the profile in the deep firn.

1.5.3 Predicting disequilibrium

Past mean ocean temperature can be estimated from the noble gas concentrations in ice core bubbles (Headly and Severinghaus, 2007; Ritz et al., 2011; Bereiter et al., 2018). On glacial-interglacial timescales, atmospheric concentrations of noble gases are primarily controlled by gas dissolution in the ocean. Because the temperature sensitivity of solubility is different for each gas, measurements of noble gas ratios in ice cores can be used to obtain a signal of integrated ocean temperature. However, as for any gas, the trace gas concentrations in bubbles must first be corrected for alterations of the atmospheric signal in the firn. In a recently published deglacial mean ocean temperature reconstruction, the WAIS Divide noble gas ice core record was corrected for gravitational fractionation and thermal fractionation using $\delta^{40}Ar/^{36}Ar$ measurements and a firn temperature gradient estimate (Bereiter et al., 2018). The authors further noted that different degrees of deviation from gravitational equilibrium (i.e., disequilibrium) can bias the gravitational fractionation correction applied to the raw noble gas record, which may lead to a cold bias of $\sim$0.3°C in Holocene and LGM temperatures. Disequilibrium effects of -287.5 per meg for Kr/N_2, -833.3 per meg for Xe/N_2 and -545.7 per meg for Xe/Kr simulated by our model correspond to absolute temperature biases of 0.33°C, 0.41°C, and 0.45°C, respectively, following the method of Bereiter et al. (2018). Because the magnitude of disequilibrium depends on firn properties and accumulation rate, glacial-interglacial changes in environmental boundary conditions may also affect the magnitude of disequilibrium in firn and thus the size of the relative deglacial temperature change estimated from noble gases.

In an attempt to compensate implicitly for disequilibrium effects and gravitational settling at the same time, it has been suggested that the elemental ratios Kr/N_2 and

Xe/N_2 in bubbles should be corrected by subtracting krypton or xenon isotope ratios, respectively (Headly, 2008). This would assume that krypton and xenon isotopes may be influenced similarly by the processes responsible for creating disequilibrium in Kr/N_2 and Xe/N_2. Therefore, this approach may compensate for disequilibrium effects and gravitational settling simultaneously, but it has been untested in models so far. The ϵ' values simulated here allow us to evaluate this method quantitatively. We use a linear fit to predict ϵ'_{Kr/N_2} from ϵ'_{Kr}. The linear fit yields good agreement with the modeled ϵ'_{Kr} over the whole firn column (R^2>0.998), indicating that the scaling between ϵ' values is nearly independent of depth. We find that (mass-normalized) ϵ'_{Kr/N_2} should be approximately 75 % of (mass-normalized) ϵ'_{Kr} at the WAIS Divide site. Scaling relationships for other isotope and element pairs are shown in Table 1.1 and are equally robust. Moreover, our results show that the source of disequilibrium is irrelevant for the correction for the macroscopic processes represented in our model. Advection and convective or dispersive mixing show the same scaling relationships for ϵ'. At Law Dome DSSW20K, the calculated ratio of ϵ'_{Kr/N_2} and ϵ'_{Kr} is at 75.9 % almost identical to the result at WAIS Divide. Sensitivity tests with the 1-D analytical model presented in Appendix A demonstrate that the disequilibrium scaling relationship between Kr isotopes and Kr/N_2 is robust to within ±5 % over a wide parameter range of molecular diffusivity, eddy diffusivity and advection velocity. Uncertainties become largest in the extreme case when ϵ'_{Ar}, the lowest simulated ϵ' value, is used to predict $\epsilon'_{Xe/Kr}$, the highest simulated ϵ' value, but they never exceed ±25 %.

Table 1.1: ϵ' scaling factor in the 2-D model with barometric pumping between different element and isotope ratios from linear regression of ϵ' value pairs at all depths. $R^2 > 0.996$ for all relationships.

Predictor:	**Response: time-variable atmospheric gas ratios**		
isotope ratio	ϵ'_{Kr/N_2}	$\epsilon'_{Xe/Kr}$	ϵ'_{Xe/N_2}
ϵ'_{Ar}	3.94	8.74	6.16
ϵ'_{Kr}	0.75	1.66	1.17
ϵ'_{Xe}	0.54	1.19	0.84

This suggests that the same scaling relationship between ϵ'_{Kr/N_2} and ϵ'_{Kr} may be assumed to hold for any ice core site without introducing large biases. ϵ'_{Kr} and ϵ'_{Xe} from combined measurements of δ^{15}N, δ^{86}Kr/^{82}Kr and δ^{136}Xe/^{129}Xe in ice cores could be used to predict the disequilibrium effects on noble elemental ratios (i.e., ϵ'_{Kr/N_2}, ϵ'_{Xe/N_2} and $\epsilon'_{Xe/Kr}$) and allows us to make a gas-specific gravitational correction. Although predicted ϵ'_{Kr} values at WAIS Divide are close to the current analytical uncertainty of the ^{86}Kr/^{82}Kr measurement, correcting for kinetic fractionation and disequilibrium will become advisable with future improvements in precision and may improve mean ocean temperature reconstructions.

1.6 Conclusions

We developed a two-dimensional firn air transport model that explicitly represents tortuosity in the firn column through migrating layers of reduced permeability. The idealized representation of firn layering is physically motivated and may illustrate the impact of firn density anomalies (i.e., summer vs winter firn or wind crusts) on gas transport. The model also accounts for thermal fractionation, a surface mixed zone, and surface pressure-forced barometric pumping. Dispersive mixing as a result of barometric pumping is constrained in the model by previously published parameterizations and not subject to tuning. Simulations of the δ^{15}N profile at WAIS Divide show that extensive horizontal diffusion through the tortuous firn structure is required by the discontinuous layers. This limits the effective vertical diffusion of gases at depth. However, layering alone does not fully prevent gravitational enrichment of isotopes in the deep firn. Similarly, the effect of barometric pumping alone is insufficient to obtain agreement with observations. The combination of barometric pumping with layering, in contrast, leads to amplified dispersive mixing. This is due to high velocity focusing in layer openings and leads to a more natural emergence of a lock-in zone in the model.

Previous studies have shown that downward advection, convective mixing and dispersive mixing all hinder trace gases in reaching the isotope ratios expected from gravitational settling (e.g., Severinghaus et al., 2010; Kawamura et al., 2013; Buizert and Severinghaus, 2016). Kinetic fractionation is strongest for slow-diffusing gases and increases with firn column depth. Our numerical experiments show that barometric pumping leads to increased isotopic disequilibrium in the firn column. However, our simulations fail to account for the full range of ^{86}Kr excess observed in the WAIS Divide core, as well as for the relatively weak δ^{15}N enrichment seen at DSSW20K, suggesting that these effects are not caused by the presence of layering (as previously suggested) and that their origin must be sought elsewhere. We further find robust scaling relationships between the magnitude of disequilibrium in different noble gas isotope and elemental ratios. Our results suggest that, to first order, these scaling relationships are independent of depth in the firn column and independent of the reason for disequilibrium for the process represented in the model (i.e., dispersive mixing, advection or convective mixing). Thus, a correction that accounts for differential kinetic fractionation may be applied to observed noble gas ratios in the reconstruction of mean ocean temperature.

1.7 Appendix A: An analytical solution for simplified firn air transport

Here, we seek an analytical solution to the following idealized scenario of firn air transport: firn air advection, diffusion, and dispersion in one dimension. In this case, vertical trace gas migration relative to the major gas nitrogen is governed by

$$\tilde{s}\frac{\partial q}{\partial t} = \frac{\partial}{\partial z}\left[\tilde{s}D_m\left(\frac{\partial q}{\partial z} - \frac{\Delta m g}{RT}q + \Omega\frac{\partial T}{\partial z}q\right) + \tilde{s}D_e\frac{\partial q}{\partial z}\right] - \tilde{s}w\frac{\partial q}{\partial z}, \tag{1.11}$$

with D_m and D_e the molecular and eddy diffusivity (m^2 s^{-1}) and w the effective vertical air advection velocity due to snow accumulation and pore compression (m s^{-1})

(e.g., Schwander et al., 1993; Rommelaere et al., 1997; Trudinger et al., 1997; Severinghaus et al., 2010; Buizert et al., 2012; Kawamura et al., 2013). The five terms on the right-hand side of Eq. (1.11) represent Fickian diffusion, gravitational settling, thermal fractionation, mass-independent dispersion and gas advection (from left to right). A Dirichlet boundary condition is chosen at the top of the firn column and represents the well-mixed atmosphere (i.e., $q\left(0\right) \equiv 0$). The bottom boundary condition is given by a Neumann boundary condition allowing only an advective flux to leave the domain ($\tilde{s}\left(D_m + D_e\right)\frac{\partial q}{\partial z} - sD_m\left(\frac{\Delta mg}{RT} - \Omega\frac{\partial T}{\partial z}\right)q \equiv 0 \;\; @\; z = z\left(COD\right)$).

Assuming steady-state and neglecting changes of $\tilde{s}$, D_m, D_e and w with depth, Eq. (1.11)) reduces to (Severinghaus et al., 2010)

$$\frac{\partial q}{\partial t} \equiv 0 = \left(D_m + D_e\right)\frac{\partial^2 q}{\partial z^2} - D_m\left(G - \mathcal{T}\right)\frac{\partial q}{\partial z} - w\frac{\partial q}{\partial z}, \tag{1.12}$$

where $G \equiv \frac{\Delta mg}{RT}$ and $\mathcal{T} \equiv \Omega\frac{\partial T}{\partial z}$ represent the constants in the gravitational and thermal fractionation term.

The solution to Eq. (1.12) yields trace gas profiles above the COD in delta notation

$$\delta = \frac{\exp\left(\frac{D_m(G-\mathcal{T})+w}{D_m+D_e}z\right) - 1}{\frac{w}{D_m(G-\mathcal{T})}\exp\left(\frac{D_m(G-\mathcal{T})+w}{D_m+D_e}z_{COD}\right) + 1}, \tag{1.13}$$

where $z_{COD} \equiv z\left(COD\right)$ (Fig. S2). δ values below the COD are constant. Note that Eq. (1.12) only applies to trace gas transport into N_2, not to transport of one trace gas into another trace gas, as discussed in the text. Because $\delta^{15}N$ only requires calculating the transport of the trace gas $^{15}N^{14}N$ into the major gas $^{28}N_2$, the equation can be used as is to calculate $\delta^{15}N$.

By evaluating some extreme cases, Eq. (1.13) illustrates a few key points about trace gas transport of $\delta^{15}N$ in firn. Under a large negative temperature gradient (i.e., atmospheric warming, $\mathcal{T} \to -\infty$), $\delta \to \infty$ and thermally sensitive gases are enriched in the firn because the numerator grows faster than the denominator. Similarly, heavier gases ($G \to \infty$) are more strongly fractionated ($\delta \to \infty$) than lighter

gases assuming they have the same molecular diffusivity. Advection ($w \to \infty$) and eddy mixing ($D_e \to \infty$) prevent the system from reaching the trace gas concentrations expected from gravitational settling and ultimately force concentrations to be constant ($\delta \to 0$). A lack of molecular diffusion ($D_m \to 0$) leads to the same result ($\delta \to 0$). Naturally, Eq. (1.13) reduces to the profile of a gravitationally settled gas (i.e., Eq. (1.1)) when $w \to 0$ and $D_e \to 0$.

1.8 Appendix B: Differential kinetic isotope fractionation in ratios of two different elements

Here we revisit the relative disequilibrium for ratios of two elements as seen in Figs. 1.11 and 1.12. First, recall the definition of ϵ' for a ratio of isotopes x and y (indicated by their nominal atomic masses)

$$\epsilon'_{x/y} \equiv \frac{10^{-3}}{m_x - m_y} \ln\left(q_{x/y}\right) - \ln\left(q_{29/28}\right) = \ln\left(\frac{q_{x/y}^{\frac{10^{-3}}{m_x - m_y}}}{q_{29/28}}\right). \tag{1.14}$$

Equation (1.3) shows that $q_{x/y}$ is the ratio of q values calculated for the transport of each isotope into $^{28}N_2$ ($q_{x/28}$ and $q_{y/28}$). $q_{x/28}$ (or $q_{y/28}$) may also be expressed in reference to nitrogen using the ϵ' value for the isotope

$$\frac{10^{-3}}{m_x - m_{28}} \ln\left(q_{x/28}\right) = \ln\left(q_{29/28}\right) + \epsilon'_{x/28}$$

$$\rightarrow \quad q_{x/28} = \left(q_{29/28} \cdot \exp\left(\epsilon'_{x/28}\right)\right)^{10^3 \times (m_x - m_{28})} \tag{1.15}$$

Note that ϵ' by definition is already mass-normalized. It follows from

Eqs. (1.3), (1.14) and (1.15) that

$$\epsilon'_{x/y} = ln\left(\frac{\left(\frac{q_{x/28}}{q_{y/28}}\right)^{\frac{10^{-3}}{m_x-m_y}}}{q_{29/28}}\right) = ln\left(\frac{\left(\frac{\left(q_{29/28}\cdot\exp\left(\epsilon'_{x/28}\right)\right)^{m_x-m_{28}}}{\left(q_{29/28}\cdot\exp\left(\epsilon'_{y/28}\right)\right)^{m_y-m_{28}}}\right)^{\frac{1}{m_x-m_y}}}{q_{29/28}}\right). \tag{1.16}$$

Equation (1.16) may be rewritten to yield

$$\epsilon'_{x/y} = \frac{m_x-m_{28}}{m_x-m_y}\left[\ln\left(q_{29/28}\right)+\epsilon'_{x/28}\right] - \frac{m_y-m_{28}}{m_x-m_y}\left[\ln\left(q_{29/28}\right)+\epsilon'_{x/28}\right] - \ln\left(q_{29/28}\right). \tag{1.17}$$

Because the terms containing $q_{29/28}$ cancel, we obtain a straightforward expression to find ϵ' for any isotope ratio from the ϵ' of two nuclides relative to $^{28}N_2$

$$\epsilon'_{x/y} = \frac{m_x-m_{28}}{m_x-m_y}\epsilon'_{x/28} - \frac{m_y-m_{28}}{m_x-m_y}\epsilon'_{y/28}. \tag{1.18}$$

Analysis of this relationship reveals that disequilibrium should most strongly affect ratios of two heavy isotopes, such as $^{132}Xe/^{84}Kr$, because heavy elements diffuse slower than N_2 (i.e., $\epsilon'_{x/28} \ll 0$) and the mass weighting factor is larger in the first than in the second term (i.e., $\frac{m_x-m_{28}}{m_x-m_y} \gg \frac{m_y-m_{28}}{m_x-m_y}$). Although this equation can theoretically predict ϵ' of any isotope ratio from ϵ' of the two isotopes x and y relative to $^{28}N_2$ (i.e., $\epsilon'_{x/28}$ and $\epsilon'_{y/28}$), in practice, this approach will not allow correcting for differential kinetic isotope fractionation. $\epsilon'_{x/28}$ cannot be measured directly and the atmospheric ratio of the noble gas x to nitrogen is not constant over long timescales. Thus, $\epsilon'_{x/28}$ will not only be affected by disequilibrium but will also be influenced by atmospheric variability resulting from gas specific solubility differences (i.e., precisely the mean ocean temperature signals we attempt to reconstruct). Instead we suggest that the scaling relationships provided in Sect. 1.5.3 can be used to predict the ϵ' of noble gas elemental ratios.

1.9 Supplement availability

The supplement related to this article is available online at: https://tc.copernicus.org/articles/12/2021/2018/tc-12-2021-2018-supplement.pdf.

1.10 Acknowledgements

We would like to thank Jakob Keck, Alan Seltzer and Ian Eisenman for providing computational resources and insightful discussions on the numerical implementation of firn air transport. Sarah Shackleton has provided helpful comments on the importance of disequilibrium in mean ocean temperature reconstruction. This work was supported by NSF grants PLR-1543229 and PLR-1543267.

Chapter 1, in full, is a reprint of the material as it appears in Birner, B., Buizert, C., Wagner, T.J.W., Severinghaus, J.P., 2018. The influence of layering and barometric pumping on firn air transport in a 2-D model. Cryosphere 12, 2021–2037. https://doi.org/10.5194/tc-12-2021-2018.The dissertation author was the primary investigator and author of this paper.

References

Alley, R. B. and Koci, B. R.: Recent warming in central Greenland?, Annals of Glaciology, 14, 6–8, 1990.

Battle, M. O., Severinghaus, J. P., Sofen, E. D., Plotkin, D., Orsi, A. J., Aydin, M., Montzka, S. A., Sowers, T., and Tans, P. P.: Controls on the movement and composition of firn air at the West Antarctic Ice Sheet Divide, Atmospheric Chemistry and Physics, 11, 11 007–11 021, doi:10.5194/acp-11-11007-2011, 2011.

Bereiter, B., Shackleton, S., Baggenstos, D., Kawamura, K., and Severinghaus, J.: Mean global ocean temperatures during the last glacial transition, Nature Publish-

ing Group, 553, 39–44, doi:10.1038/nature25152, URL http://dx.doi.org/10.1038/nature25152, 2018.

Buizert, C. and Severinghaus, J. P.: Dispersion in deep polar firn driven by synoptic-scale surface pressure variability, The Cryosphere, 10, 2099–2111, doi:10.5194/tc-2016-148, 2016.

Buizert, C., Martinerie, P., Petrenko, V. V., Severinghaus, J. P., Trudinger, C. M., Witrant, E., Rosen, J. L., Orsi, A. J., Rubino, M., Etheridge, D. M., Steele, L. P., Hogan, C., Laube, J. C., Sturges, W. T., Levchenko, V. A., Smith, A. M., Levin, I., Conway, T. J., Dlugokencky, E. J., Lang, P. M., Kawamura, K., Jenk, T. M., White, J. W. C., Sowers, T., Schwander, J., and Blunier, T.: Gas transport in firn: Multiple-tracer characterisation and model intercomparison for NEEM, Northern Greenland, Atmospheric Chemistry and Physics, 12, 4259–4277, doi:10.5194/acp-12-4259-2012, 2012.

Buizert, C., Sowers, T., and Blunier, T.: Assessment of diffusive isotopic fractionation in polar firn, and application to ice core trace gas records, Earth and Planetary Science Letters, 361, 110–119, doi:10.1016/j.epsl.2012.11.039, 2013.

Colbeck, S.: Air Movement in Snow due to Windpumping, Journal of Glaciology, 35, 209–213, 1989.

Craig, H., Horibe, Y., and T., S.: Gravitational separation of gases and isotopes in polar ice caps, Science, 242, 1675–1678, 1988.

Dahl-Jensen, D., Morgan, V. I., and Elcheikh, A.: Monte Carlo inverse modelling of the Law Dome (Antarctica) temperature profile, Annals of Glaciology, 29, 145–150, doi:10.3189/172756499781821102, 1999.

Darcy, H.: Les Fontaines Publiques de la Ville de Dijon, Victor Dalmont, Paris, 1856.

Dlugokencky, E. J., Lang, P. M., Crotwell, A. M., Mund, J. W., Crotwell, M. J., and Thoning, K. W.: Atmospheric Methane Dry Air Mole Fractions from the NOAA ESRL Carbon Cycle Cooperative Global Air Sampling Network, 1983-2015, Version: 2016-07-07, 2016a.

Dlugokencky, E. J., Lang, P. M., Mund, J. W., Crotwell, A. M., Crotwell, M. J., and Thoning, K. W.: Atmospheric Carbon Dioxide Dry Air Mole Fractions from the NOAA ESRL Carbon Cycle Cooperative Global Air Sampling Network, 1968-2015, Version: 2016-08-30, 2016b.

Etheridge, D. M., Steele, L. P., Langenfelds, R. L., Francey, R. J., Barnola, J. M., and Morgan, V. I.: Natural and anthropogenic changes in atmospheric CO2 over the last 1000 years from air in Antarctic ice and firn, Journal of Geophysical Research-Atmospheres, 101, 4115–4128, doi:10.1029/95JD03410, 1996.

Etheridge, D. M., Steele, L. P., Francey, R. J., and Langenfelds, R. L.: Atmospheric methane between 1000 A.D. and present: Evidence of anthropogenic emissions and climatic variability, Journal of Geophysical Research, 103, 15 979, doi:10.1029/98JD00923, 1998.

Freeze, R. and Cherry, J.: Groundwater, Prentice-Hall, Inc., Englewood Cliffs, New Jersey, 1979.

Grachev, A. and Severinghaus, J. P.: Laboratory determination of thermal diffusion constants for 29N2 /28N2 in air at temperatures from -60 to 0° C for reconstruction of magnitudes of abrupt climate changes using the ice core fossil – air paleothermometer, Geochimica et cosmochimica Acta, 67, 345–360, 2003a.

Grachev, A. M. and Severinghaus, J. P.: Determining the Thermal Diffusion Factor for 40Ar/ 36Ar in Air To Aid Paleoreconstruction of Abrupt Climate Change, The Journal of Physical Chemistry A, 107, 4636–4642, doi:10.1021/jp027817u, 2003b.

Headly, M.: Krypton and xenon in air trapped in polar ice cores: paleo-atmospheric measurements for estimating past mean ocean temperature and summer snowmelt frequency, Phd dissertation, University of California, San Diego, 2008.

Headly, M. A. and Severinghaus, J. P.: A method to measure Kr/N2 ratios in air bubbles trapped in ice cores and its application in reconstructing past mean ocean temperature, Journal of Geophysical Research, 112, 1–12, doi:10.1029/2006JD008317, 2007.

Hörhold, M. W., Laepple, T., Freitag, J., Bigler, M., Fischer, H., and Kipfstuhl, S.: On the impact of impurities on the densification of polar firn, Earth and Planetary Science Letters, 325-326, 93–99, doi:10.1016/j.epsl.2011.12.022, 2012.

Johnsen, S. J.: Stable isotope profiles compared with temperature profiles in firn with historical temperature records, Isotopes and Impurities in Snow and Ice, pp. 388–392, 1977.

Kawamura, K., Severinghaus, J. P., Albert, M. R., Courville, Z. R., Fahnestock, M. A., Scambos, T. A., Shields, E., and Shuman, C. A.: Kinetic fractionation of gases by deep air convection in polar firn, Atmospheric Chemistry and Physics, 13, 11 141–11 155, doi:10.5194/acp-13-11141-2013, 2013.

Keeling, C. D., Stephen, C., Piper, S. C., Bacastow, R. B., Wahlen, M., Whorf, T. P., Heimann, M., and Meijer, H. A.: Exchanges of atmospheric CO2 and 13CO2 with the terrestrial biosphere and oceans from 1978 to 2000., Global Aspects, SIO Reference Series. Scripps Institution of Oceangraphy, San Diego, 01-06, 83–113, doi:10.1007/b138533, 2001.

Lazzara, M. A., Weidner, G. A., Keller, L. M., Thom, J. E., and Cassano, J. J.: Antarctic Automatic Weather Station Program: 30 Years of Polar

Observation, Bulletin of the American Meteorological Society, 93, 1519–1537, doi:10.1175/BAMS-D-11-00015.1, 2012.

Lüthi, D., Le Floch, M., Bereiter, B., Blunier, T., Barnola, J.-M., Siegenthaler, U., Raynaud, D., Jouzel, J., Fischer, H., Kawamura, K., and Stocker, T. F.: High-resolution carbon dioxide concentration record 650,000-800,000 years before present., Nature, 453, 379–382, doi:10.1038/nature06949, 2008.

Mitchell, L. E., Buizert, C., Brook, E. J., Breton, D. J., Fegyveresi, J., Baggenstos, D., Orsi, A., Severinghaus, J., Alley, R. B., Albert, M., Rhodes, R. H., McConnell, J. R., Sigl, M., Maselli, O., Gregory, S., and Ahn, J.: Observing and modeling the influence of layering on bubble trapping in polar firn, Journal of Geophysical Research Atmospheres, 120, 2558–2574, doi:10.1002/2014JD022766, 2015.

Orsi, A. J., Cornuelle, B. D., and Severinghaus, J. P.: Little Ice Age cold interval in West Antarctica: Evidence from borehole temperature at the West Antarctic Ice Sheet (WAIS) Divide, Geophysical Research Letters, 39, 1–7, doi:10.1029/2012GL051260, 2012.

Orsi, A. J., Kawamura, K., Fegyveresi, J. M., Headly, M. A., Alley, R. B., and Severinghaus, J. P.: Differentiating bubble-free layers from Melt layers in ice cores using noble gases, Journal of Glaciology, 61, 585–594, doi:10.3189/2015JoG14J237, 2015.

Petit, R. J., Jouzel, J., Raynaud, D., Barkov, N. I., Barnola, J.-M., Basile, I., Bender, M., Chappellaz, J., Davis, M., Delaygue, G., Delmotte, M., Kotyakov, V. M., Legrand, M., Livenkov, V. Y., Lorius, C., Pépin, L., Ritz, C., Saltzman, E., and Stievenard, M.: Climate and atmospheric history of the past 420,000 years from the Vostok ice core, Antarctica, Nature, 399, 429–413, doi:10.1038/20859, 1999.

Ritz, S. P., Stocker, T. F., and Severinghaus, J. P.: Noble gases as

proxies of mean ocean temperature: Sensitivity studies using a climate model of reduced complexity, Quaternary Science Reviews, 30, 3728–3741, doi:10.1016/j.quascirev.2011.09.021, 2011.

Rommelaere, V., Arnaud, L., and Barnola, J.-M.: Reconstructing recent atmospheric trace gas concentrations from polar firn and bubbly ice data by inverse methods, Journal of Geophysical Research, 102, 30 069–30 083, 1997.

Sapart, C. J., Martinerie, P., Witrant, E., Chappellaz, J., Van De Wal, R. S., Sperlich, P., Van Der Veen, C., Bernard, S., Sturges, W. T., Blunier, T., Schwander, J., Etheridge, D., and Röckmann, T.: Can the carbon isotopic composition of methane be reconstructed from multi-site firn air measurements?, Atmospheric Chemistry and Physics, 13, 6993–7005, doi:10.5194/acp-13-6993-2013, 2013.

Schwander, J.: The transformation of snow to ice and the occlusion of gases, The Environmental Record in Glaciers and Ice Sheets H. Oeschger, CC Langway, 53–67, 1989.

Schwander, J., Stauffer, B., and Sigg, A.: Air mixing in firn and the age of the air at pore close-off, Annals of Glaciology, 10, 141–145, 1988.

Schwander, J., Barnola, J.-M., Andrié, C., Leuenberger, M., Ludin, A., Raynaud, D., and Stauffer, B.: The age of the air in the firn and the ice at Summit, Greenland, Journal of Geophysical Research, 98, 2831–2838, doi:10.1029/92JD02383, 1993.

Severinghaus, J. P. and Battle, M. O.: Fractionation of gases in polar ice during bubble close-off: New constraints from firn air Ne, Kr and Xe observations, Earth and Planetary Science Letters, 244, 474–500, doi:10.1016/j.epsl.2006.01.032, 2006.

Severinghaus, J. P., Grachev, A., and Battle, M.: Thermal fractionation of air in polar firn by seasonal temperature gradients, Geochemistry, Geophysics, Geosystems, 2, 1–24, doi:10.1029/2000GC000146, 2001.

Severinghaus, J. P., Albert, M. R., Courville, Z. R., Fahnestock, M. A., Kawamura, K., Montzka, S. A., Mühle, J., Scambos, T. A., Shields, E., Shuman, C. A., Suwa, M., Tans, P., and Weiss, R. F.: Deep air convection in the firn at a zero-accumulation site, central Antarctica, Earth and Planetary Science Letters, 293, 359–367, doi:10.1016/j.epsl.2010.03.003, 2010.

Sowers, T., Bender, M., and Raynaud, D.: Elemental and Isotopic Composition of Occluded O2 and N2 in Polar Ice, Journal of Geophysical Research, 94, 5137–5150, doi:10.1029/JD094iD04p05137, 1989.

Trudinger, C. M., Enting, I. G., Etheridge, D. M., Francey, R. J., Levchenko, V. A., Steele, L. P., Raynaud, D., and Arnaud, L.: Modeling air movement and bubble trapping in firn, Journal of Geophysical Research: Atmospheres, 102, 6747–6763, doi:10.1029/96JD03382, 1997.

Trudinger, C. M., Etheridge, D. M., Rayner, P. J., Enting, I. G., Sturrock, G. A., and Langenfelds, R. L.: Reconstructing atmospheric histories from measurements of air composition in firn, Journal of Geophysical Research Atmospheres, 107, 1–13, doi:10.1029/2002JD002545, 2002.

Trudinger, C. M., Enting, I. G., Rayner, P. J., Etheridge, D. M., Buizert, C., Rubino, M., Krummel, P. B., and Blunier, T.: How well do different tracers constrain the firn diffusivity profile?, Atmospheric Chemistry and Physics, 13, 1485–1510, doi:10.5194/acp-13-1485-2013, 2013.

Van Ommen, T. D., Morgan, V. I., Jacka, T. H., Woon, S., and Elcheikh, A.: Near-surface temperatures in the Dome Summit South (Law Dome, East Antarctica) borehole, Annals of Glaciology, 29, 141–144, doi:doi:10.3189/172756499781821382, 1999.

WAIS Divide Project Members: Precise interpolar phasing of abrupt climate change during the last ice age, Nature, 520, 661–665, doi:10.1038/nature14401, 2015.

Weller, G. and Schwerdtfeger, P.: Thermal properties and heat transfer processes of low-temperature snow, in: Meteorological Studies at Plateau Station, Antarctica, edited by Dalrymple, P. C., Riordan, A. J., Riordan, A., Riordan, A. J., and Weller, H. H. Lettau, H. Lettau, L. A. Stroschein, L. S. Kundla, Leander A. Stroschein, M. Kuhn, Peter Schwerdtfeger, R. C. L. a. R., vol. 25, American Geophysical Union, 1977.

Chapter 2

Gravitational separation of Ar/N_2 and age of air in the lowermost stratosphere in airborne observations and a chemical transport model

2.1 Abstract

Accurate simulation of atmospheric circulation, particularly in the lower stratosphere, is challenging due to unresolved wave–mean flow interactions and limited high-resolution observations for validation. Gravity-induced pressure gradients lead to a small but measurable separation of heavy and light gases by molecular diffusion in the stratosphere. Because the relative abundance of Ar to N_2 is exclusively controlled by physical transport, the argon-to-nitrogen ratio (Ar/N_2) provides an additional constraint on circulation and the age of air (AoA), i.e., the time elapsed

since entry of an air parcel into the stratosphere. Here we use airborne measurements of N_2O and Ar/N_2 from nine campaigns with global coverage spanning 2008–2018 to calculate AoA and to quantify gravitational separation in the lowermost stratosphere. To this end, we develop a new N_2O–AoA relationship using a Markov chain Monte Carlo algorithm. We observe that gravitational separation increases systematically with increasing AoA for samples with AoA between 0 and 3 years. These observations are compared to a simulation of the TOMCAT/SLIMCAT 3-D chemical transport model, which has been updated to include gravitational fractionation of gases. We demonstrate that although AoA at old ages is slightly underestimated in the model, the relationship between Ar/N_2 and AoA is robust and agrees with the observations. This highlights the potential of Ar/N_2 to become a new AoA tracer that is subject only to physical transport phenomena and can supplement the suite of available AoA indicators.

2.2 Introduction

Transport in the middle atmosphere is driven by a combination of advection by the Brewer–Dobson circulation (BDC) (Brewer, 1949; Dobson, 1956) and quasi-horizontal, two-way mixing by breaking waves (Holton et al., 1995) Models consistently predict an acceleration of the BDC due to climate change (Butchart, 2014), but subgrid-scale mixing processes and momentum transfer by unresolved buoyancy waves limit our ability to accurately simulate circulation in the stratosphere (Haynes, 2005; Plumb, 2007). An acceleration of the BDC has important repercussions for stratosphere–troposphere exchange (STE) and thus recovery of the ozone layer and the greenhouse effect of stratospheric water vapor; however, observational evidence of an acceleration of the BDC is weak (Engel et al., 2009, 2017; Waugh, 2009; Ray et al., 2014, 2010).

The mean age of air (AoA) is a widely used indicator of stratospheric circula-

tion (Hall and Plumb, 1994; Waugh and Hall, 2002; Linz et al., 2016). Air can be transported to any location r in the stratosphere via a myriad of different paths, and each path will have an associated transit time. The probability density function that describes the likelihood of air reaching location r with a specific transit time is called the age spectrum. Although the age spectrum is not directly observable, some aspects of its shape can be inferred from observations of short- and long-lived tracers (Andrews et al., 1999, 2001; Schoeberl et al., 2005; Hauck et al., 2019, 2020; Podglajen and Ploeger, 2019). For tracers that are conserved in the stratosphere and whose concentrations increase approximately linearly with time in the troposphere, such as SF_6 and CO_2, the mean AoA, i.e., the first moment of the distribution, can simply be calculated as the time difference, or "lag time", to when tracer concentrations in the upper troposphere last had comparable values as measured in a stratospheric sample (Hall and Plumb, 1994; Boering et al., 1996; Waugh and Hall, 2002). The stratospheric concentration of N_2O has also been calibrated as an independent AoA tracer by relating the gradual photolytic loss of N_2O in the stratosphere to AoA as determined from CO_2 (Boering et al., 1996; Andrews et al., 2001; Linz et al., 2017).

In contrast to early measurements made on rocket samples (Bieri and Koide, 1970), Ishidoya et al. (2008, 2013) have shown using a balloon-borne sampling system that stratospheric air is detectably fractionated by gravitational settling (GS), with the degree of fractionation strongly correlated to AoA (Ishidoya et al., 2008, 2013, 2018; Sugawara et al., 2018; Belikov et al., 2019). GS leads to depletion of heavier gases in the stratosphere yielding lower ratios of heavy to light gases, e.g., Ar/N_2, $^{18}O/^{16}O$ of O_2 and $^{15}N/^{14}N$ of N_2, with increasing elevation. The vertical gradients induced by gravimetric separation are steeper at higher latitudes (Ishidoya et al., 2008, 2013, 2018; Sugawara et al., 2018), and consistent with patterns observed in stratospheric AoA (Sugawara et al., 2018; Belikov et al., 2019). Gravimetric settling in the stratosphere has also been simulated in 1-D (Keeling, 1988; Ishidoya et al., 2008), 2-D (Ishidoya et al., 2013, 2018; Sugawara et al., 2018), and 3-D stratospheric

models (Belikov et al., 2019); 2-D and 3-D models both show a pattern of GS which increases with altitude and latitude, similar to the patterns observed in tracers with a significant stratospheric sink such as N_2O, and consistent with a positive correlation with AoA (Ishidoya et al., 2013; Sugawara et al., 2018; Belikov et al., 2019). Here we attempt to calibrate GS of Ar/N_2 as an AoA tracer similar to previous work on the N_2O–AoA relationship.

Observing GS in the stratosphere is challenging, however, as the signals are small and because of the need to avoid artifacts caused by temperature- and pressure-induced fractionation near the sampling inlet (Blaine et al., 2006; Ishidoya et al., 2008, 2013). The resulting scatter in existing balloon-based measurements precludes a clear evaluation of the relationship between GS and AoA (Belikov et al., 2019).

Here we present a dataset of gravitational fractionation of Ar/N_2 and AoA observations made on flask samples from three airborne research projects totaling nine campaigns in the lowermost stratosphere with mean AoA < 3 years (Wofsy et al., 2017, 2018; Stephens, 2017). The HIAPER Pole-to-Pole Observations (HIPPO) project was a global survey of the Pacific troposphere to lower stratosphere on the NSF/NCAR Gulfstream-V aircraft (Wofsy et al., 2011), composed of five individual campaigns from 2008 to 2011. The O_2/N_2 Ratio and CO_2 Airborne Southern Ocean (ORCAS) study was conducted using the same aircraft but focused on the Drake Passage and Antarctic Peninsula during January–February 2016 (Stephens et al., 2018). The Atmospheric Tomography (ATom) project was a survey of the troposphere and lower stratosphere of the Pacific and Atlantic Ocean basins on the NASA DC-8 aircraft, composed of four individual campaigns from 2016 to 2018 (Prather et al., 2017). The observations are compared to new simulations of GS with the TOMCAT/SLIMCAT (Chipperfield, 2006) tracer transport model. Our goals are to demonstrate the consistency of our data with gravitational fractionation, to evaluate model performance, and to highlight the potential of Ar/N_2 as a new age tracer.

2.3 Methods

2.3.1 Measurements

Discrete 1.5 L flask samples were taken with the NCAR/Scripps Medusa Whole Air Sampler (Bent, 2014; Stephens et al., 2020) (https://www.eol.ucar.edu/instruments/ncar-scripps-airborne-flask-sampler, last access: 7 June 2020). Medusa holds 32 borosilicate glass flasks sealed with Viton o-rings and uses active pressure control to fill the flasks with cryogenically dried air to ~ 760 torr. Flasks are shipped to the Scripps Institution of Oceanography (SIO) for analysis of Ar/N_2 ratios on an IsoPrime Mass Spectrometer. We report changes in Ar/N_2 ratios in delta notation:

$$\delta = \left(\frac{R_{\mathrm{SA}}}{R_{\mathrm{REF}}} - 1 \right) \times 10^6 \,(\text{per meg})\,, \tag{2.1}$$

where R_{SA} is the mixing or isotope ratio in the sample and R_{REF} the ratio in a reference mixture. Measurements are made on the Scripps O2 Program Argon Scale, as defined on 21 January 2020. $\delta(Ar/N_2)$ values are reported after applying an offset to the data to yield a mean of zero in the tropical airborne observations of the free troposphere between 3 and 8 km.

Uncertainty in $\delta(Ar/N_2)$ observations arises from a combination of analytical limitations and artifactual fractionation during sampling. Replicate agreement of surface flasks shows a 1σ repeatability of ± 6.1 per meg for $\delta(Ar/N_2)$, but additional scatter in the data may be introduced by small leaks in the Medusa system and thermal or pressure gradient fractionation at the sample intake (Morgan et al., 2020; Stephens et al., 2020). For further details, see (Bent, 2014). These effects are challenging to separate from true atmospheric variability and differ between campaigns because sampling strategies have generally improved over time. To constrain uncertainty due to aircraft sampling, we quantify total variability in observations from the presumably fairly homogeneous tropical troposphere between 3 and 8 km (Fig. S1

in the Supplement). Data from the earlier campaigns HIPPO 1–5 show a pooled standard deviation of 24 per meg, whereas data from ATom 2–4 yield a pooled standard deviation of 9 per meg, illustrating advances in sampling and sample handling. While no ORCAS samples are available in the tropical troposphere, ORCAS data show similar scatter to ATom 2–4 data between 20 and 50. For all campaigns, the uncertainty is small compared to the stratospheric signal of tens to hundreds per meg shown below. We also show that the stratospheric signal in $\delta(\mathrm{Ar}/\mathrm{N_2})$ is not due to pressure-dependent inlet fractionation by evaluating the residual $\delta(\mathrm{Ar}/\mathrm{N_2})$, which has been corrected for the natural gravitational signal (Fig. S2).

We have compiled available simultaneous, high-frequency measurements of a range of other trace gases, including N_2O, CO_2, O_3, CH_4, and CO, to identify Medusa samples with stratospheric influence and calculate mean AoA. N_2O was measured continuously with a precision of 0.09 ppb at 1 Hz frequency using the Harvard Quantum Cascade Laser Spectrometer (QCLS) (Santoni et al., 2014) during HIPPO and ORCAS and measured every 1–3 min using the NOAA gas chromatograph PAN and Trace Hydrohalocarbon ExpeRiment (PANTHER) during ATom. The Unmanned Aircraft Systems Chromatograph for Atmospheric Trace Species (UCATS) was used to measure O_3 during HIPPO and ATom. O_3 was not measured on ORCAS. We use continuous H_2O data from the NCAR open-path near-infrared multi-pass spectrometer Vertical Cavity Surface Emitting Laser (VCSEL) (Zondlo et al., 2010) for HIPPO and ORCAS, whereas H_2O was measured using the NASA Diode Laser Hygrometer (DLH) (Diskin et al., 2002) during ATom flights. CH_4, CO_2, and CO were measured by QCLS during HIPPO and ORCAS and by the NOAA Picarro (Karion et al., 2013) during ATom. An averaging kernel is applied to the continuous and semi-continuous aircraft data, such as N_2O, O_3, and H_2O, to match it to Medusa samples. The kernel multiplies a weighting function $w_i(t)$ by all continuous data before time t_s, when Medusa switched from sample flask i to sample flask $i+1$. $w_i(t)$

for each sample i is given by

$$w_i(t) = \exp\left[\frac{-t_s - t}{\tau}\right], \tag{2.2}$$

where t is each 1 s increment of the continuous data and $\tau = \frac{V}{Q}$ is the flushing time of air in a Medusa flask determined by the flask volume V and airflow Q.

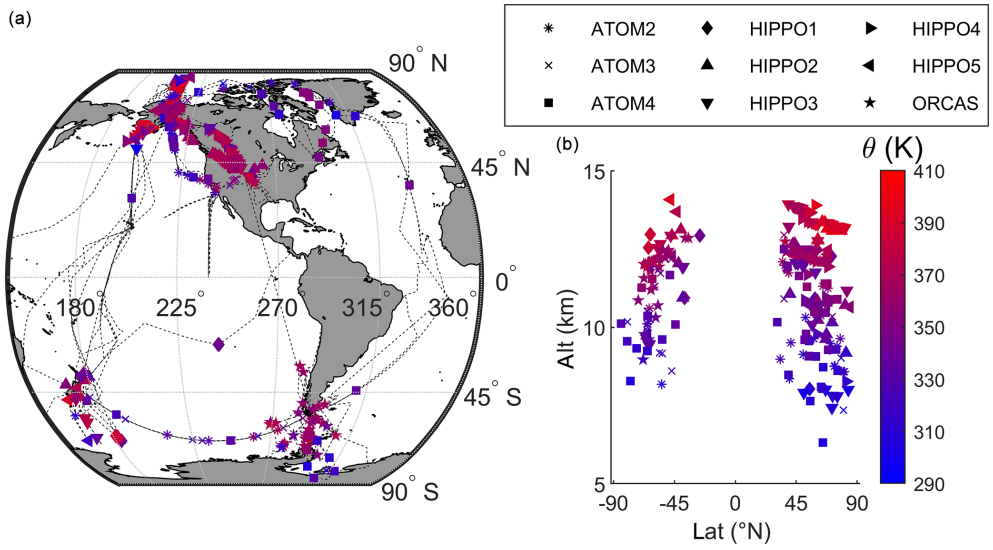

Figure 2.1: Horizontal **(a)** and vertical **(b)** distributions of airborne flask sample locations identified as being of stratospheric origin (see text). Thin dashed black lines on the map illustrate the flight tracks of all nine campaigns. Symbols indicate the campaigns during which the stratospheric samples were collected, and colors show the potential temperature at which the sample was taken.

Stratospheric samples are identified based on their N_2O, O_3, and water vapor levels. Classification based on chemical composition rather than potential temperature or altitude effectively selects samples with a clear stratospheric signature in the lowermost stratosphere and excludes air which has experienced substantial mixing with tropospheric air masses. We label samples as "stratospheric" if (i) water vapor levels are below 15 ppm and either (ii.a) O_3 values exceed 140 ppb or (ii.b) N_2O (detrended to a reference year of 2009) is below 315 ppb. These criteria yield 234 lower stratospheric samples with high-quality N_2O and $\delta(Ar/N_2)$ data, spanning a wide range of

latitudes poleward of 40n both the Northern Hemisphere and Southern Hemisphere (Fig. 2.1). We use Medusa samples from all five HIPPO campaigns, ORCAS, and ATom 2–4. We do not use samples from ATom 1 because inlet fractionation due to the unique inlet design and location on the DC-8 on this campaign introduced apparent biases on the order of 30 per meg. An additional 25 stratospheric samples are available from the START-08 campaign on the NSF/NCAR GV, but we have not used these here because of the limited number of flasks collected and greater scatter in the data.

2.3.2 AoA calculation

Stratospheric (mean) AoA for Medusa samples is calculated from N_2O using an updated hemisphere-specific N_2O–AoA relationship. Our method broadly follows Andrews et al. (2001) who assumed a bimodal age spectrum and used multiple observations of CO_2 binned by N_2O values to resolve the seasonal cycle of CO_2 in each bin. Properties of the age spectrum for each N_2O bin, including mean AoA, were constrained by optimizing the agreement between observed CO_2 concentrations and concentrations implied by randomly generated age spectra in each N_2O bin. Andrews et al. (2001) used a highly efficient "genetic algorithm" to yield the most likely relationship between mean AoA and N_2O in each bin. In contrast, we use a more computationally costly Markov chain Monte Carlo (MCMC) method that allows us to obtain more robust uncertainties for all estimated parameters of the age spectrum. Following Malinverno (2002) and Green (1995), our algorithm builds on a Metropolis–Hastings sampler (Metropolis et al., 1953; Hastings, 1970) to evaluate probability distributions for each age spectrum parameter and automatically chooses whether a unimodal or bimodal representation of the age spectrum is more appropriate in each N_2O bin. Finally, we constructed a new tropical upper troposphere reference time series for CO_2 in this study to ensure maximum consistency between

all observations used. Analytical and methodological uncertainties are propagated thoroughly and reported as the 95% confidence interval around a mean.

We consider the tropical upper troposphere to be the single entry point of air into the stratosphere for our AoA calculation. Mixing between tropospheric and lower stratospheric air can occur outside the tropics, leading to air masses that are transitional between stratospheric and tropospheric in the lowermost extratropical stratosphere (e.g. Škerlak et al., 2014). This additional pathway for tropospheric entry has been accounted for in previous studies via additional model information and/or multiple tracers (Ray et al., 1999; Hoor et al., 2004; Bönisch et al., 2009; Hauck et al., 2020). However, we are limited by the number of tracers available to us and therefore instead aim to largely exclude samples influenced through this additional pathway by using thresholds in N_2O, O_3, and H_2O when identifying stratospheric samples. Because of this sample selection strategy, we note that the ages calculated here should not be considered representative of the region that air was sampled in.

Our upper troposphere reference time series (TRTS) consists of a long-term trend and a representation of the mean seasonal cycle. Because direct CO_2 observations in the region are limited, the long-term trend and a first guess of the mean seasonal cycle are estimated from monthly mean surface observations at the Mauna Loa station in Hawaii (MLO, 19N, 155W; Fig. 2.2a) (Keeling et al., 2001) which are later adjusted to match airborne observations in the tropics (20S–20N) above 8 km (Fig. 2.2c). The adjustment includes (i) a constant offset, (ii) a reduced amplitude of the seasonal cycle, and (iii) a phase lag of 1 month. As shown in Fig. 2.2, after these adjustments the TRTS matches the mean seasonal cycle and absolute value of the airborne data, thus accounting for known vertical gradients of CO_2 and reduced seasonality in the upper troposphere (Fig. 2.2d). The amplitude of the seasonal cycle in our time series is also in good agreement with the boundary condition used by Andrews et al. (1999, 2001).

The new TRTS is used to estimate the age spectrum in 13 N_2O bins of 5 or 10 ppb

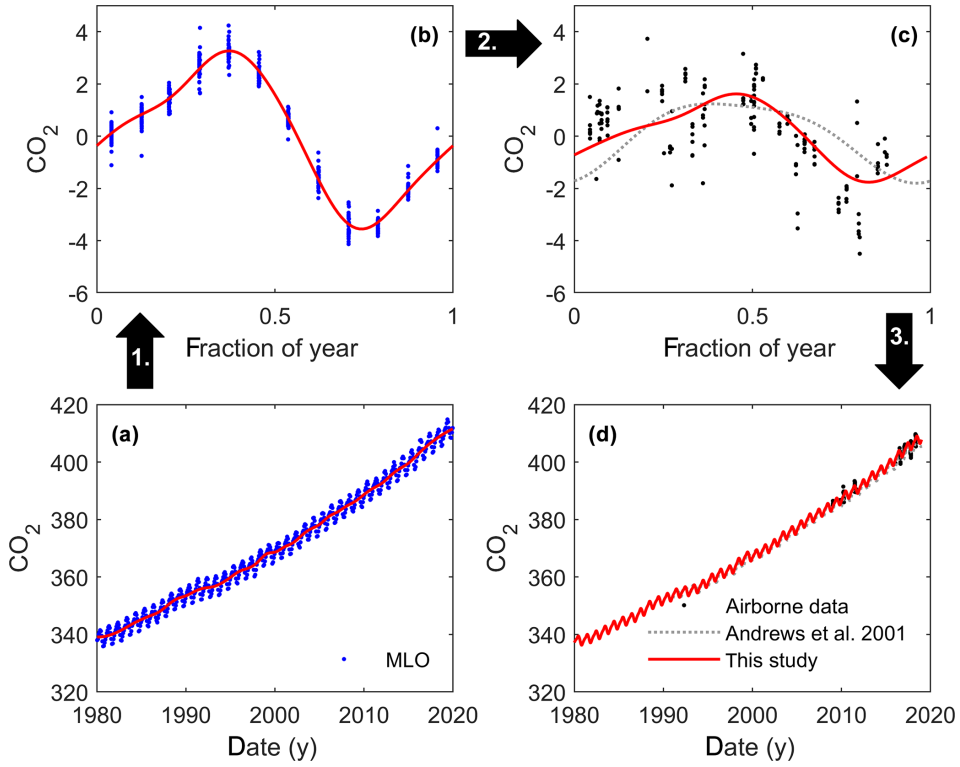

Figure 2.2: Illustration of the major steps in deriving a tropical upper tropospheric reference time series. Panel **(a)** shows the monthly mean surface CO_2 concentrations at Mauna Loa (MLO) (Keeling et al., 2001) with a stiff spline trend shown in red. Panel **(b)** shows a fit of the mean seasonal cycle at MLO compared to detrended observations from 1980 to 2019. Panel **(c)** shows the 1-month lagged seasonal cycle (red line) rescaled in amplitude to match detrended airborne observations in the equatorial upper troposphere (20S $<$ lat $<$ 20N, alt $>$ 8 km, black). The seasonal cycle derived by Andrews et al. (2001) is presented as a dotted grey line for reference. Panel **(d)** shows the resulting upper tropospheric mean reference time series (TRTS, red) used for CO_2 in the age-of-air algorithm with the airborne observations from the tropical upper troposphere (black dots) and the time series (grey dotted line) of Andrews et al. (2001).

width (320–325, ..., 290–295, 280–290, ..., 230–240 ppb) using a Markov chain Monte Carlo (MCMC) algorithm which compares observed CO_2 concentrations in the bin to concentration expected from the TRTS. To maximize data availability, we use high-frequency data (see Sect. 2.3.1) identified as stratospheric according to the criteria above from the 10 s merged products available for HIPPO, ORCAS, and ATom rather than data averaged to the lower Medusa sampling interval for this calibration exercise. Small corrections are applied to the observed CO_2 concentrations (< 0.2 ppm) to account for oxidation of CH_4 and CO in the stratosphere.

The MCMC algorithm considers random noise in the TRTS and uses a unimodal or bimodal inverse Gaussian shape of the age spectrum characterized by mean ages Γ_1 and Γ_2 and shape parameters λ_1 and λ_2:

$$\begin{aligned} G\left(t' \middle| \left(\Gamma_1, \Gamma_2, \lambda_1, \lambda_2\right)\right) = \\ A\sqrt{\frac{\lambda_1}{2\pi t'^3}} \exp\left(-\frac{\lambda_1 \left(t' - \Gamma_1\right)^2}{2\Gamma_1^2 t'}\right) \\ + (1 - A)\sqrt{\frac{\lambda_2}{2\pi t'^3}} \exp\left(-\frac{\lambda_2 \left(t' - \Gamma_2\right)^2}{2\Gamma_2^2 t'}\right), \end{aligned} \tag{2.3}$$

where factor A determines the relative weight of each peak and a value of $A = 1$ yields a unimodal spectrum (Hall and Plumb, 1994; Andrews et al., 2001; Bönisch et al., 2009). Though more complex representations of the age spectrum have recently been proposed, accounting for multiple modes and seasonal variations (e.g., Bönisch et al., 2009; Li et al., 2012; Hauck et al., 2019, 2020; Podglajen and Ploeger, 2019), these require additional information from multiple tracers or models and good seasonal data coverage that is not available here. In any case, we only rely on the first moment of the age distribution (i.e., the mean age) for calibrating the N_2O–AoA relationship, and the mean age is not particularly sensitive to the assumed shape of the age spectrum (Andrews et al., 2001). By setting $A = 1$ for 50% of all tested age spectra, the MCMC algorithm automatically selects whether a unimodal or bimodal representation of the age spectrum is optimal for matching observations. Although

bimodal solutions with five instead of two free parameters will always be able to fit the data better, a larger number of parameters also decreases the likelihood of randomly selecting a combination of parameters that match the observations well because the fraction of the total parameter space region which yields good agreement with the observation decreases as more parameters are added (Malinverno, 2002). The algorithm is thus able to make an appropriate choice between unimodal and bimodal distributions from the data themselves, without any further *a priori* assumptions. The MCMC algorithm is set up separately with 2000 independent chains for each N_2O bin to account for uncertainty in the TRTS and obtain best estimates of the mean AoA, i.e., the first moment of Eq. (2.3). To simplify the algorithm, possible values of $\Gamma_1, \Gamma_2, \lambda_1$, and λ_2 are repeatedly sampled from the same N_2O bin-specific prior distributions. Details of the algorithm are presented in Appendix A.

Finally, the resulting relationship between mean AoA and the N_2O concentration of each bin is fit separately for each hemisphere by a quadratic polynomial, and the polynomial is evaluated at the N_2O value of each Medusa sample to pair every observation of $\delta(Ar/N_2)$ with an AoA. Uncertainty in N_2O and the polynomial fits are propagated by a Monte Carlo scheme. Overall, our method estimates the most likely mean AoA for each Medusa sample and improves upon previous methods by providing a framework for the treatment of uncertainty resulting from (i) analytical error, (ii) uncertainty in the shape of the age spectrum, and (iii) uncertainty in the composition of source gas introduced into the stratosphere.

2.3.3 TOMCAT/SLIMCAT model

TOMCAT/SLIMCAT (hereafter TOMCAT) is an offline 3-D chemical tracer transport model that has been used extensively for studies of stratospheric ozone depletion and circulation (e.g., Chipperfield, 2006; Chipperfield et al., 2017; Krol et al., 2018). For this study, TOMCAT was run over 31 years, from 1988 to 2018,

with a timestep of 30 min at 2.82.8orizontal resolution forced by the ERA-Interim reanalysis (Dee et al., 2011) at 60 vertical hybrid sigma-pressure (σ–p) levels up to $\sim$ 60–65 km. The first 20 years (i.e., before the first flask observation) were treated as spin-up. The TOMCAT AoA tracer is initialized at the surface and corrected to a value of AoA = 0 just below the tropical tropopause. Vertical motion was calculated from the divergence of the horizontal mass fluxes. Although this approach gives slightly younger stratospheric AoA than using isentropic levels and radiative heating rates, it allows a more detailed treatment of tropospheric transport (Chipperfield, 2006; Monge-Sanz et al., 2007). The model simulation was sampled at the times and locations of the Medusa flask observations to provide a direct comparison between the measurements and model.

Following the methodology of Belikov et al. (2019), we include an additional vertical flux term in the model representing the GS of gases in the atmosphere. The vertical flux $\mathbf{f}_i$ (mol m^{-2} s^{-1}) of tracer i due to molecular diffusion in Earth's gravitational field is given as (Banks and Kockarts, 1973; Belikov et al., 2019)

$$\mathbf{f}_i = -D_i N C_i \left[\frac{1}{C_i} \frac{\partial C_i}{\partial z} + \left(\frac{1}{H_i} - \frac{1}{H_{\text{air}}} \right) + \alpha_i \frac{1}{T} \frac{\partial T}{\partial z} \right], \tag{2.4}$$

where D_i is the tracer-specific binary molecular diffusivity in air (m^2 s^{-1}), N is the number density of air (mol m^{-3}), C_i is the mixing ratio, $H_i = \frac{RT}{gM_i}$ is the tracer-specific atmospheric equilibrium scale height (m), R is the fundamental gas constant (J K^{-1} mol^{-1}), g is the gravitational constant (m s^{-2}), M_i is the tracer-specific atomic or molecular mass (kg mol^{-1}), α_i is the tracer-specific thermal diffusivity (m^2 s^{-1}), and T is temperature (K). The three terms in Eq. (2.4) represent molecular diffusion driven by (i) vertical gradients in the mole fraction of i, (ii) pressure gradients caused by gravity and described by the barometric law, and (iii) temperature gradients (left to right). We neglect the first and third terms in the brackets in Eq. (2.4), leaving only the gravitational settling term $\left(\frac{1}{H_i} - \frac{1}{H_{\text{air}}}\right)$ on the basis that both terms are orders of magnitude less important than the gravitational separation term under stratospheric

conditions (see Appendix B) (Ishidoya et al., 2013; Belikov et al., 2019). No fluxes are allowed through the top boundary, and C_i is held constant at the Earth's surface.

To simplify the numerical treatment, we simulate an idealized reference tracer of gravitational fractionation δ_{GST}, which has a molecular mass 1 amu greater than air and diffusivity equal to that of Ar (see Appendices B and C). This tracer can be scaled offline to obtain the gravitational separation signal in any other species, including $\delta(\mathrm{Ar}/\mathrm{N_2})$, e.g.,

$$\delta\left(Ar/N_2\right) \approx \frac{(M_{\mathrm{Ar}} - M_{\mathrm{air}}) \times D_{\mathrm{Ar}} - (M_{N_2} - M_{\mathrm{air}}) \times D_{N_2}}{(M_{\mathrm{GST}} - M_{\mathrm{air}}) \times D_{\mathrm{GST}}} \times \delta_{\mathrm{GST}}. \tag{2.5}$$

The appropriate diffusivity values D_{Ar} and D_{N_2} for Ar and $\mathrm{N_2}$ in air are derived in Appendix B for a ternary mixture of Ar, $\mathrm{O_2}$, and $\mathrm{N_2}$, extending previous work (Ishidoya et al., 2013; Belikov et al., 2019). δ_{GST} is divided by D_{GST} in Eq. (2.5) and therefore does not depend on the exact value chosen for D_{GST}.

2.3.4 NIES TM model

We compare our results to previous simulations of GS using the National Institute for Environmental Studies chemical transport model (NIES TM) published recently by Belikov et al. (2019). The NIES TM is a 3-D transport model of similar complexity to TOMCAT driven by the Japanese 25-year Reanalysis (JRA-25) with a hybrid sigma–isentropic (σ–θ) vertical coordinate up to 5 hPa or $\sim$ 35 km. The model and GS results are described in detail in Belikov et al. (2013, 2019), respectively.

2.4 Results

2.4.1 $\mathrm{N_2O}$–AoA calibration

Our new relationships between $\mathrm{N_2O}$ and mean AoA for the Northern Hemisphere and Southern Hemisphere (NH and SH) are well constrained by the observations

and generally follow the mid-latitude NH calibration curve of Andrews et al. (2001) (Fig. 2.3d). At mean AoA > 2.5, the N_2O–AoA relationship yields slightly younger ages in the NH than in the SH and compared to the previously published curve, suggesting there might be a latitudinal dependence of the relationship. Such a latitude dependence is, in fact, expected based on theory (Plumb, 2007). We expect curvature and a latitudinal difference in the N_2O–AoA relationship because photolysis of N_2O depends on latitude and altitude due to local sunlight availability. Furthermore, mixing of young and old air results in a mixture with an anomalously low N_2O concentration for a given age. Since the SH, NH, and tropics feature different photolysis rates and show different degrees of mixing/isolation, different N_2O–AoA relationships are expected.

Unimodal age spectra are generally preferentially selected by the algorithm, in particular for the SH (Fig. 2.3a–c), but unimodal age spectra dominate the solution ensemble by a small margin except for AoA < 0.5 years (Fig. S3). Confidence intervals on age spectra parameters from bimodal spectra are considerably wider than for unimodal spectra. This implies that the parameters in a bimodal distribution are redundant and the shape of the age spectrum is not sufficiently constrained by the observations used. The width of the spectrum in each N_2O bin varies widely within the prescribed bounds for most unimodal and bimodal age spectra (Fig. S3). It appears that not enough data are available from the airborne campaigns to determine the amplitude of the seasonal cycle with enough confidence to constrain the width of the age spectrum and distinguish the relative contribution of the old peak (influencing primarily the mean concentration difference to the troposphere) and the young peak (controlling the amplitude of seasonality) in bimodal age spectra. Additional observations with less scatter or information from different age tracers are needed to properly resolve the shape of the age spectra. Despite the limited resolution of the seasonal cycle, the observations are sufficient to place tight limits on the mean AoA in each N_2O bin and yield a well-characterized relationship between N_2O and mean

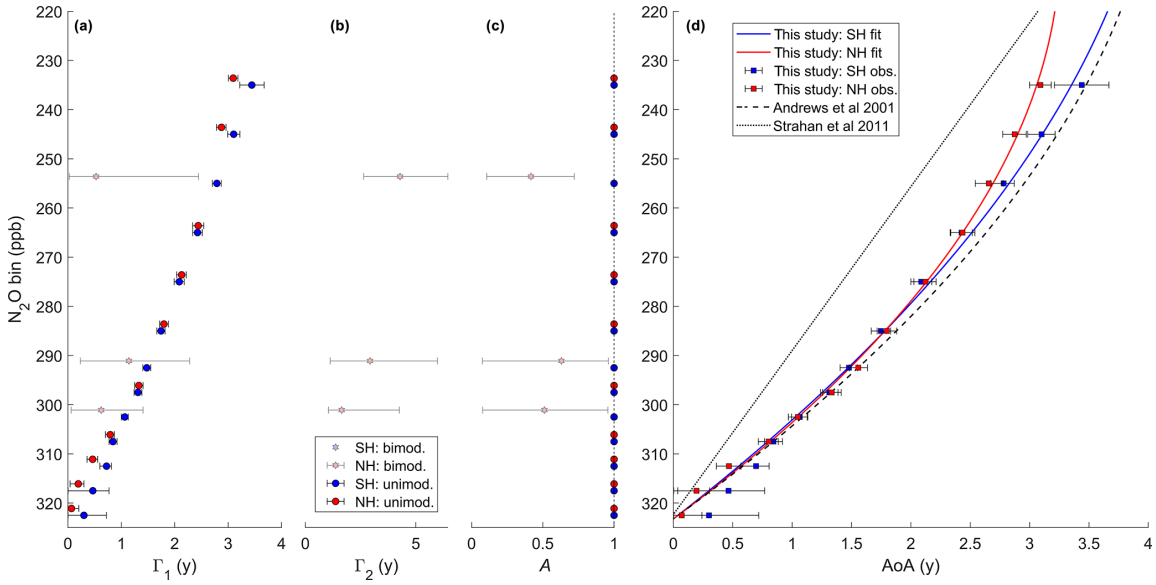

Figure 2.3: Hemisphere-specific properties of the age spectra in different N_2O bins from the 10 s averaged airborne observations estimated by Markov chain Monte Carlo. Panels **(a)**–**(c)** show the value and 95% confidence interval of Γ_1 Γ_2 and A in each bin for either a unimodal (blue and red circles) or bimodal (faint blue and faint red stars) age spectrum depending on which type was preferentially selected by the algorithm. N_2O values are offset by 1.4 ppb for all Northern Hemisphere estimates (NH, red) for visual clarity in panels **(a)**–**(c)**. Panel **(d)** shows the mean AoA and confidence interval of the age spectra ensemble in each bin (i.e., unimodal and bimodal together). These data are fit by a quadratic polynomial for each hemisphere with a fixed y intercept (NH AoA $= -0.0002381(323.23 - N_2O)^2 + 0.05567(323.23 - N_2O)$; SH AoA $= -0.0001723(323.23 - N_2O)^2 + 0.05317(323.23 - N_2O)$). Previous relationships published by Andrews et al. (2001) and Strahan et al. (2011) are given as a dashed and dotted line for reference. y-intercept values of the previously published N_2O–AoA calibrations have been updated to reflect the gradual increase in tropospheric N_2O between 1997 and the new reference year 2009.

AoA for each hemisphere.

2.4.2 The relationship between mean AoA and GS in models and observations

A comparison of the AoA–GS relationship with observations yields good agreement for the TOMCAT model results within the observational uncertainties (Fig. 2.4a), but the observations fall outside the range of GS predicted by the NIES TM (Belikov et al., 2019) for mean AoA > 1 year (Fig. 2.4b). For young samples with mean AoA < 3 years, GS of $\delta(\mathrm{Ar}/\mathrm{N_2})$ increases by roughly 35–45 per meg per year of AoA in both TOMCAT and observations and converges to zero for the youngest samples. In the upper stratosphere, TOMCAT does not obtain any ages as old as observed by Ishidoya et al. (2013, 2008, 2018) and therefore cannot reproduce these observations directly. Changing the vertical coordinate system of TOMCAT or forcing the model with a different reanalysis product could improve agreement with the observations for old ages because TOMCAT in the configuration used here is known to slightly underestimate AoA in the upper stratosphere (Monge-Sanz et al., 2007; Chabrillat et al., 2018). The very steep AoA–GS relationship for the oldest simulated air is however seen in TOMCAT and the balloon observations.

A comparison of $\delta(\mathrm{Ar}/\mathrm{N_2})$ and AoA between flask samples and TOMCAT is shown in Fig. S4. However, the direct comparison should not be considered a good test of model performance because our stratospheric composition criteria intentionally target unusually old air in the lowermost stratosphere. For the same reason, profiles of $\delta(\mathrm{Ar}/\mathrm{N_2})$ and AoA are not evaluated here. Instead, we suggest the AoA–GS relationship provides a more robust metric for comparison. Overall, our observations validate the implementation of GS for young (< 3 years) ages in TOMCAT.

The relationship between mean AoA and GS differs between TOMCAT and the NIES TM (Fig. 2.5). The NIES TM shows weaker curvature in the relationship overall and produces larger declines in $\mathrm{Ar}/\mathrm{N_2}$ at ages less than 4.5 years compared to

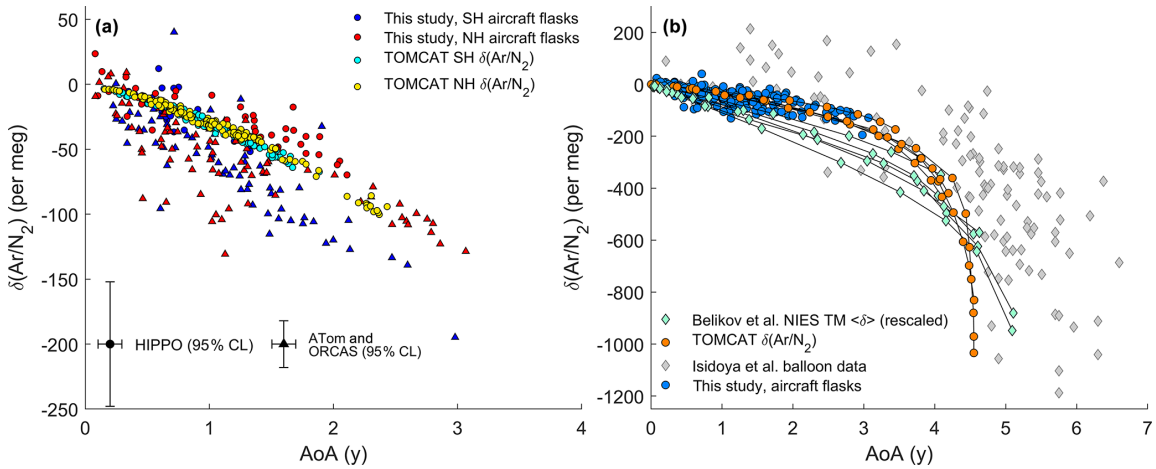

Figure 2.4: Comparison of age of air (AoA) and gravitational settling (GS) of $\delta(\mathrm{Ar/N_2})$ in models and observations. Panel **(a)** shows observations from the Northern Hemisphere (red) and Southern Hemisphere (blue) together with TOMCAT model output (SH: cyan; NH: yellow) selected from the closest model grid box in time and space. Because uncertainty for AoA is similar for all stratospheric samples but $\delta(\mathrm{Ar/N_2})$ uncertainty differs between campaigns, representative error bars (95% confidence interval) are shown for HIPPO (triangles) and ATom/ORCAS (circles) at an arbitrary AoA. $\delta(\mathrm{Ar/N_2})$ is normalized to yield a delta value of zero in the equatorial free troposphere. In panel **(b)**, observations from airborne campaigns (this study) and the balloon sampling system (Ishidoya et al., 2008, 2013, 2018; Sugawara et al., 2018) are plotted with the AoA–GS relationship observed in TOMCAT and the NIES TM (Belikov et al., 2019) as lines for each of the latitude bands shown in Fig. 2.5 and points for different altitude bins between 10 and 35 km. To yield an equivalent estimate of $\delta(\mathrm{Ar/N_2})$, $\delta(^{13}\mathrm{CO_2}/^{12}\mathrm{CO_2})$ results from the NIES TM (Belikov et al., 2019) have been rescaled according to Eq. (2.5) and offset by $\sim$ 10 per meg to account for the different tropospheric reference region in the definition of δ.

TOMCAT. In TOMCAT's mesosphere (which is at the limit of the domain covered by the ERA-Interim reanalyses forcing the model), AoA is near uniform, but GS continues to increase with increasing altitude, changing the relationship between mean AoA and GS in this region. The AoA–GS relationship in TOMCAT is very similar in all non-tropical regions (outside 15> lat > −15, whereas the curvature of the relationship is slightly stronger in the tropics. In contrast, the NIES TM has a

clear dependence of the AoA–GS relationship on latitude. There is also some evidence in the observations of a dependence of the AoA–GS relationship on hemisphere. In the observations, $\delta(\mathrm{Ar/N_2})$ values appear to be slightly more negative in the SH than in the NH for the same age, particularly for AoA > 1.5 years. However, almost all SH samples with mean AoA older than 1.5 years come only from the ORCAS campaign. This campaign used a different inlet design than HIPPO and ATom, which could cause a small artifactual offset, but the scatter in our observations generally makes it difficult to separate signal from noise for small interhemispheric differences.

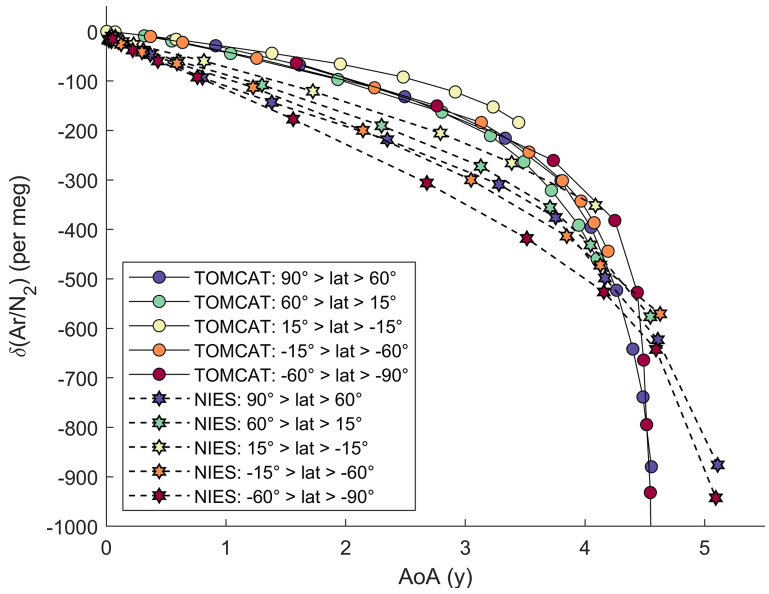

Figure 2.5: Comparison of the annual and zonal mean age of air (AoA) relationship with gravitational settling simulated in TOMCAT and the NIES TM. The relationship is plotted as lines for the latitude bands indicated by marker color. For the NIES TM, markers show the vertical profile using all grid boxes available between $\sim$ 10 and 35 km. For TOMCAT, markers instead correspond to binned altitude bands between 10 and 35 km with a spacing of 2.5 km because of the finer vertical resolution of the model. To yield an equivalent estimate of $\delta(\mathrm{Ar/N_2})$, $\delta(^{13}\mathrm{CO_2}/^{12}\mathrm{CO_2})$ results from the NIES TM (Belikov et al., 2019) have been rescaled according to Eq. (2.5) and offset by $\sim$ 10 per meg to account for the different tropospheric reference region in the definition of δ.

2.4.3 GS and AoA in TOMCAT

Annual mean $\delta(\mathrm{Ar}/\mathrm{N_2})$ in TOMCAT follows the typical pattern of a tracer with a stratospheric sink (Chipperfield, 2006), as previously found in simulations using the NIES TM (Belikov et al., 2019) and the SOCRATES model (Ishidoya et al., 2013; Sugawara et al., 2018) (Fig. 2.6). $\delta(\mathrm{Ar}/\mathrm{N_2})$ is zero in the troposphere and decreases with elevation. The most depleted $\delta(\mathrm{Ar}/\mathrm{N_2})$ is observed at high latitudes where sinking air of the Brewer–Dobson circulation advects strongly fractionated air downward. In the tropics, $\delta(\mathrm{Ar}/\mathrm{N_2})$ values are considerably less fractionated at the same altitude due to upwelling of unfractionated tropospheric air. Vertical gradients in $\delta(\mathrm{Ar}/\mathrm{N_2})$ generally increase with altitude and are largest in the mesosphere ($>$ 50 km) because molecular diffusion increases with decreasing pressure and eventually dominates above the turbopause (not shown). There are strong seasonal changes in $\delta(\mathrm{Ar}/\mathrm{N_2})$ depletion on the order of several thousand per meg, in particular in the high-latitude mesosphere, with the strongest fractionation occurring during the winter season (see movie available with online version of the paper).

The AoA tracer in TOMCAT shows a similar pattern to $\delta(\mathrm{Ar}/\mathrm{N_2})$, with younger ages at low altitude and in the tropics and the oldest ages in the mesosphere. Vertical gradients in mean AoA are largest at high latitudes close to the tropopause. At high latitudes above 20 km and at low latitudes above 50 km, vertical gradients of AoA mostly disappear and AoA becomes nearly uniform.

2.5 Discussion

2.5.1 Difference between TOMCAT and the NIES TM

We hypothesize that an adequate representation of the mesosphere in models is critical in determining the curvature of the AoA–GS relationship. The residence time of air above $\sim$ 40 km is rather short in TOMCAT, and AoA is nearly constant

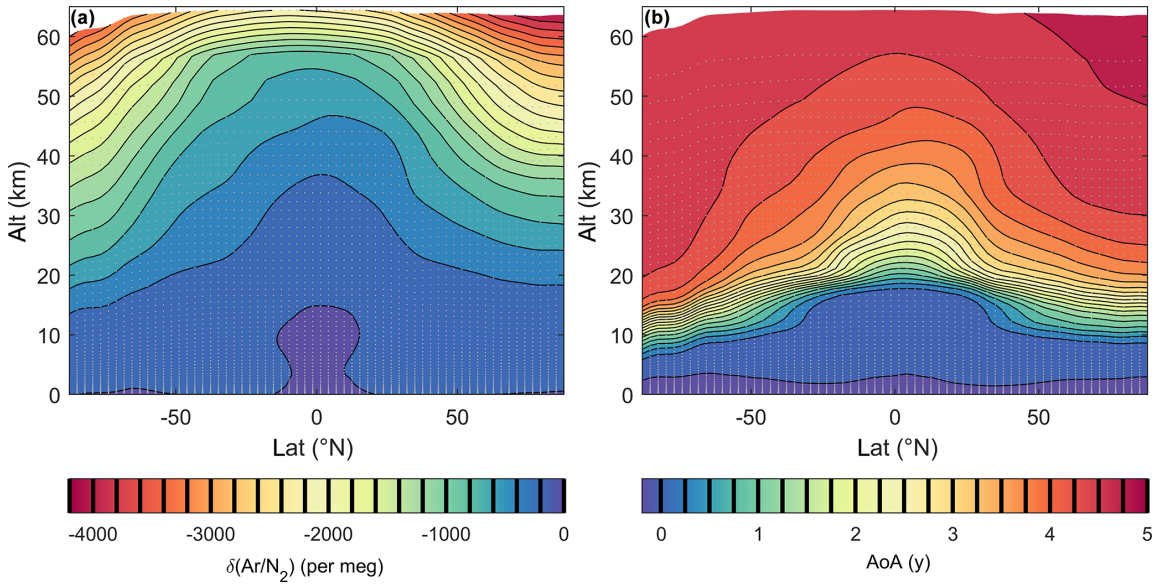

Figure 2.6: Annual and zonal means of $\delta(\mathrm{Ar}/\mathrm{N}_2)$ **(a)** and age of air (AoA) **(b)** simulated by TOMCAT. Values of the contour lines are shown as black vertical lines on the color bar. Grey dots indicate the center of a grid box in TOMCAT. A video of this figure highlighting the natural variability in monthly-mean values is available in the Supplement.

with altitude in this region. GS in contrast continues to increase with altitude because of the diffusivity dependence on pressure allowing gases to separate more effectively. The much lower top of the NIES TM ($\sim$ 35 km vs. 60–65 km) reduces its ability to capture this effect, which impacts the AoA–GS relationship because the mesospheric signal is exported into the stratosphere, in particular in polar regions where mesospheric air descends. TOMCAT furthermore produces a less negative slope of the AoA–GS relationship for young air (mean AoA $<$ 3 years) and greater similarity in the AoA–GS relationship between latitude bands than the NIES TM as shown in Fig. 2.5. This could in part be a consequence of using a different meteorological reanalysis product for forcing the two models (Chabrillat et al., 2018) or could indicate differences between the models in vertical and horizontal mixing intensity.

2.5.2 Estimating mean AoA from observed $\delta(Ar/N_2)$

Different tracers of AoA all have unique strengths and weaknesses. Estimating AoA in the lowermost stratosphere from CO_2 for example is limited by complexities involving seasonality and the possibility of multiple entry points of air into the stratosphere due to isentropic mixing with the midlatitude troposphere (Hall and Plumb, 1994; Andrews et al., 2001; Waugh and Hall, 2002). SF_6-derived AoA in contrast is biased high at mid and high latitudes due to the influence of mesospheric air which has been photochemically depleted in SF_6 (Kovács et al., 2017; Linz et al., 2017). N_2O as an AoA tracer relies on the photolytic destruction of N_2O in the stratosphere, which may depend strongly on location and had only been empirically calibrated for young ages at mid latitudes so far (Andrews et al., 2001; Linz et al., 2017).

Thanks to the robust relationship between mean AoA and $\delta(Ar/N_2)$ and the small seasonal cycle amplitude of $\delta(Ar/N_2) < 5$ per meg in the upper troposphere (Fig. S1), mean AoA could also be estimated from $\delta(Ar/N_2)$. Using the current analytical $\delta(Ar/N_2)$ uncertainty of 12.2 per meg (2σ) and the AoA–$\delta(Ar/N_2)$ relationship seen in TOMCAT (including variability from seasonal and latitudinal differences), we estimate that mean AoA could be calculated to within about ± 0.4 years (2σ, Fig. S5). This is still considerably worse than the ± 0.1-year confidence interval in mean AoA estimated from N_2O. However, the uncertainty can be improved with future improvements in sampling, and the accuracy and precision of the measurements.

The heavy noble gases krypton and xenon will be roughly 3.6× and 5.8× more strongly fractionated in the stratosphere than Ar but are also more challenging to measure due to their $\sim$ 8000× and 100 000× lower abundance in the atmosphere. Nevertheless, future analysis of these gases in stratospheric air samples might further improve our ability to estimate AoA from the gravitational fractionation of gases and help diagnose artifactual fractionation, because heavier noble gases are more strongly

fractionated under the influence of gravity and less sensitive to thermal fractionation (Seltzer et al., 2019).

2.5.3 Future directions

An open question in climate applications of noble gases is whether there could be a stratospheric influence on tropospheric $\delta(\mathrm{Ar}/\mathrm{N_2})$. Tropospheric observations of $\delta(\mathrm{Ar}/\mathrm{N_2})$ and other noble gas-elemental ratios have been used to infer ocean heat content changes by capitalizing on the temperature dependency of gas solubility in the oceans (Keeling et al., 2004; Ritz et al., 2011; Headly and Severinghaus, 2007; Bereiter et al., 2018). However, long-term trends (Butchart, 2014) and natural variability in stratospheric circulation and stratosphere–troposphere exchange (STE) such as the Quasi-Biennial Oscillation (QBO) (Baldwin et al., 2001) could advect a stratospheric GS signal into the troposphere and alias onto surface observations of these gases. To this end, we calculate the volumetric Ar deficit in the atmosphere in moles using TOMCAT (Fig. 2.7) relative to a hypothetical, unfractionated atmosphere with a homogenous mixing ratio ($C_{\mathrm{o_{Ar}}}$) at all elevations. Ar deficit is

$$\mathrm{Ar_{deficit}} = (C_{\mathrm{Ar}} - C_{\mathrm{o_{Ar}}}) \times N_{\mathrm{air}}, \tag{2.6}$$

where C_{Ar} is the simulated Ar mixing ratio and N_{air} is the number density of air.

The Ar deficit is concentrated in the lower stratosphere at around 20 km and at mid to high latitudes. Although the GS signal is considerably stronger in the mesosphere, the potential for perturbing the troposphere is low given the low molar density of air in the mesosphere. The region with the greatest potential to influence the troposphere therefore lies in the lower stratosphere. The total Ar deficit of the atmosphere above 200 hPa is approximately -2.9×10^{13} mol and the atmosphere below 200 hPa contains roughly 1.3×10^{18} mol of Ar. Perturbing STE and/or the stratospheric circulation by 10%, consistent with interannual to decadal variability of STE in models (Salby and Callaghan, 2006; Flury et al., 2013; Ray et al., 2014;

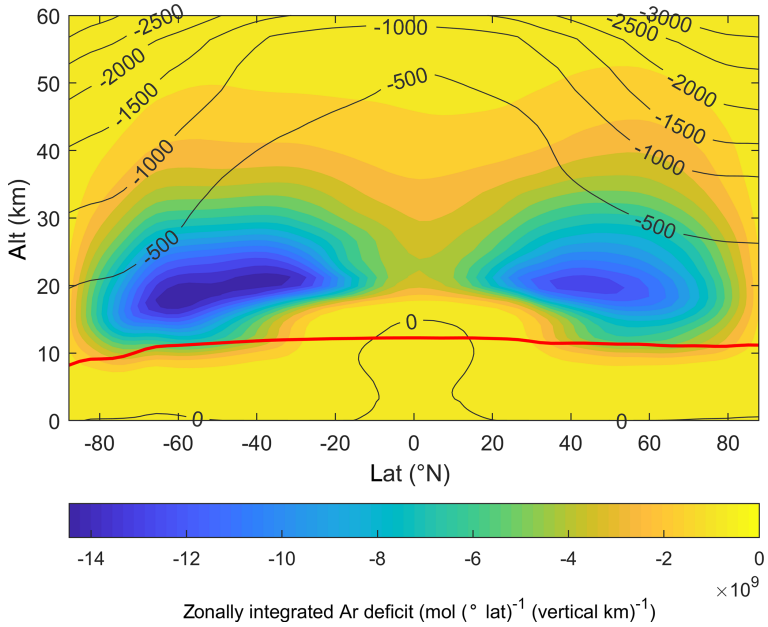

Figure 2.7: Color map of annual mean and zonally integrated Ar deficit in TOMCAT. Overlain black contour lines show $\delta(\mathrm{Ar}/\mathrm{N_2})$ (per meg). The red solid line highlights the mean position of the 200 hPa isobar.

Montzka et al., 2018), thus should lead to a detectable signal of roughly 2.2 per meg ($-2.9 \times 10^{13}/1.3 \times 10^{18} \times 10\% \times 10^6$) in tropospheric $\delta(\mathrm{Ar}/\mathrm{N_2})$. Corresponding advection of stratospheric GS signals in $\mathrm{N_2}$ amplifies the pure Ar signal by roughly 10%. A careful investigation of such a signal in the $\delta(\mathrm{Ar}/\mathrm{N_2})$ surface network data (Keeling et al., 2004) is needed because secular trends of $\delta(\mathrm{Ar}/\mathrm{N_2})$ caused by degassing of Ar and $\mathrm{N_2}$ from a warming ocean are also expected to be on the order of 2–3 per meg per decade. Previous studies have also used ratios involving heavier noble gases ($\mathrm{Xe}/\mathrm{N_2}$, $\mathrm{Kr}/\mathrm{N_2}$) to reconstruct mean ocean temperature changes over glacial–interglacial timescales (Headly and Severinghaus, 2007; Bereiter et al., 2018; Baggenstos et al., 2019). Simultaneous changes in stratospheric circulation and STE affect heavier noble gases more strongly than $\mathrm{Ar}/\mathrm{N_2}$ and will need to be accounted for in such applications of noble gas thermometry.

2.6 Conclusions

With improvements in data treatment, measurement quality, and modeling constraints, we have shown that gravitational fractionation of Ar relative to N_2 in the stratosphere and mesosphere is a potentially powerful constraint on circulation. High-precision observations of $\delta(Ar/N_2)$ in air samples of the lowermost stratosphere from nine airborne campaigns are well captured by the TOMCAT/SLIMCAT 3-D chemical transport model, which has been updated to account for the influence of gravity on air composition through molecular diffusion. In the observations and the model, $\delta(Ar/N_2)$ is directly related to stratospheric mean age of air (AoA) derived here using a new calibration of N_2O. Our observations for mean AoA < 3 years produce a slope of roughly 35–45 per meg of $\delta(Ar/N_2)$ per year of AoA. TOMCAT/SLIMCAT shows better agreement with the new observations than the NIES transport model (Belikov et al., 2019), and we speculate that the model disagreement could be explained by (i) the factor of 2 lower top of the NIES transport model, (ii) the use of different reanalysis products, and/or (iii) differences in vertical and horizontal mixing. In this context, further work is also needed to study the influence of unresolved turbulence on AoA and $\delta(Ar/N_2)$ in chemical transport models.

As the importance of stratospheric circulation for ozone recovery, climate projections, and evaluation of tropospheric trends in halocarbons is increasingly recognized, a need for new observations from the still undersampled stratosphere is becoming evident. Combining $\delta(Ar/N_2)$ with other tracers of circulation could lead to new insights into atmospheric mixing and transport. $\delta(Ar/N_2)$ has potential advantages over existing approaches based on transient tracers such as CO_2 or N_2O since $\delta(Ar/N_2)$ is only influenced by the physics of transport and mostly unaffected by seasonality in the tropical upper troposphere. Furthermore, because of its large gradients at high altitudes, $\delta(Ar/N_2)$ observations from the upper stratosphere and mesosphere could improve our understanding of circulation on seasonal and interannual timescales in a

region where AoA becomes near uniform, and some photochemical age tracers such as N_2O are almost fully depleted and thus lose sensitivity to circulation changes.

2.7 Appendix A: Description of the Markov chain Monte Carlo algorithm

The following list outlines key steps in our MCMC algorithm to calculate AoA from CO_2 for each N_2O bin.

1. Start a new Markov chain and allow for uncertainty in TRTS by adding white noise with an amplitude given by the scatter of upper tropospheric observations around the mean TRTS in Fig. 2.2.

2. With a 50% chance, peak weighting factor A is set to zero and a unimodal spectrum is tested ($k = 1$). Alternatively, A is allowed to vary between 0 and 1 for a bimodal distribution ($k = 2$).

3. The other age spectrum parameters are selected from N_2O bin-dependent prior distributions: Γ_1 is sampled from a uniform prior distribution with a mean AoA predicted by the N_2O–AoA relationship of Andrews et al. (2001) and with generous width (> 1.5 years). Γ_2 is sampled from a uniform prior distribution with values between 1 and 6 years representing older stratospheric air. The shape parameters are defined as $\lambda_i \equiv \frac{\Gamma_i^2}{2\gamma_i}$, and γ_i is chosen randomly for each peak with values between 0.1 and 1, as observed in previous studies (Hall and Plumb, 1994; Andrews et al., 2001; Waugh and Hall, 2002).

4. Convolve the age spectrum calculated from the parameters ($\mathbf{m} \equiv [\Gamma_1, \Gamma_2, \lambda_1, \lambda_2, A]$) with the perturbed TRTS to obtain a possible time series of CO_2 in the N_2O bin and calculate the misfit ($\mathbf{e}$) between the CO_2 time series and observations.

5. Calculate the likelihood function $P(\mathbf{d}|k,\mathbf{m})$ for the set of parameters $\mathbf{m}$ and k, given a total of n observations ($\mathbf{d}$):

$$P(\mathbf{d}|k,\mathbf{m}) = \frac{1}{\left[(2\pi)^n \det\left(\hat{\mathbf{C}}_\mathbf{e}\right)\right]^{0.5}} \exp\left(-\frac{1}{2}\mathbf{e}^T\hat{\mathbf{C}}_\mathbf{e}^{-1}\mathbf{e}\right). \quad (2.7)$$

where $\hat{\mathbf{C}}_\mathbf{e}$ is the covariance matrix. We assume that all n observations are independent. Thus, $\hat{\mathbf{C}}_\mathbf{e}$ has only diagonal entries of $\sigma^2_{CO_2}$ and $\det(\hat{\mathbf{C}}_\mathbf{e})$ simplifies to $(\sigma^2_{CO_2})^n$. The value of $\sigma^2_{CO_2}$ is different for each bin and determined iteratively as the approximate root mean square error of the observations around the final time series for each bin obtained at the end of the MCMC algorithm. Typical values of $\sigma^2_{CO_2}$ are between 0.18 and 1.28 ppm and generally decrease with increasing AoA of a N_2O bin.

6. If this is the first pass of the chain, define k_{saved} and $\mathbf{m}_{\text{saved}}$ to equal k and $\mathbf{m}$. Otherwise, calculate the selection criterion $\alpha \equiv \min\left(1, \frac{P(\mathbf{d}|k,\mathbf{m})}{P(\mathbf{d}|k_{\text{saved}},\mathbf{m}_{\text{saved}})}\right)$ and accept k and $\mathbf{m}$ as new saved values ($k_{\text{saved}}\mathbf{m}_{\text{saved}}$) with probability α. Sampling from the same prior distributions on each pass of the chain simplifies our expression of α compared to that presented by Malinverno (2002), making it only dependent on the likelihood ratio.

7. Repeat steps 2–6 1000 times, sampling parameter values from the same prior distributions, and store the final values of k_{saved} and $\mathbf{m}_{\text{saved}}$ obtained after the 1000th iteration (i.e., a plausible solution produced past the burn-in period) for later use.

8. To sample the full posterior pdf (i.e., the full uncertainty about the age spectrum parameters), initialize 2000 different Markov chains by repeating steps 1–7. Each stored value of $\mathbf{m}$ characterizes one age spectrum that is likely not far from the best solution, given the data $\mathbf{d}$, yielding an ensemble of 2000 age

spectra from which statistics can be computed. Note that each Markov chain is fully independent, so the algorithm can be easily parallelized to minimize computational costs.

2.8 Appendix B: Derivation of Eq. (2.4) from the Maxwell–Stefan equations

We start by approximating air as a ternary mixture of N_2, O_2, and Ar and later generalize to consider additional trace species. According to the Maxwell–Stefan equations (Taylor and Krishna, 1993), diffusion in this ternary mixture is governed by

$$\mathbf{d}_{N_2} = \frac{C_{N_2}\mathbf{f}_{\mathrm{Ar}} - C_{\mathrm{Ar}}\mathbf{f}_{N_2}}{N \times D_{N_2:Ar}} + \frac{C_{N_2}\mathbf{f}_{O_2} - C_{O_2}\mathbf{f}_{N_2}}{N \times D_{N_2:O_2}}, \tag{2.8}$$

$$\mathbf{d}_{\mathrm{Ar}} = \frac{C_{\mathrm{Ar}}\mathbf{f}_{N_2} - C_{N_2}\mathbf{f}_{\mathrm{Ar}}}{N \times D_{Ar:N_2}} + \frac{C_{\mathrm{Ar}}\mathbf{f}_{O_2} - C_{O_2}\mathbf{f}_{\mathrm{Ar}}}{N \times D_{Ar:O_2}}, \tag{2.9}$$

$$\mathbf{f}_{O_2} = -\mathbf{f}_{N_2} - \mathbf{f}_{\mathrm{Ar}}, \tag{2.10}$$

$$C_{N_2} + C_{O_2} + C_{\mathrm{Ar}} = 1, \tag{2.11}$$

where $C_i \equiv n_i/N$ is the mole fraction, n_i is molar or number density (mol m^{-3}), N is the total number density (mol m^{-3}), $\mathbf{f}_i$ is the molecular diffusion flux (mol m^2 s^{-1}) relative to the molar average velocity of the mixture, $\mathbf{d}_i$ is the thermodynamic driving force for molecular diffusion (m^{-1}), and $D_{i:j}$ is the binary diffusion coefficient of the $(i:j)$ pair. An equation for O_2 that is analogous to Eq. (2.8) is not needed because changes in O_2 are governed by the conservation Eqs. (2.10) and (2.11). Binary diffusivity coefficients (cm^2 s^{-1}) can be calculated using the method of Fuller et al. as reported in Reid et al. (1987):

$$D_{ij} = 0.001\frac{T^{1.75}\left(\frac{1}{M_i} + \frac{1}{M_j}\right)^{0.5}}{P\left[\nu_i^{1/3} + \nu_j^{1/3}\right]^2}, \tag{2.12}$$

where P is pressure (atm), ν_i is the molecular diffusion volume of a trace gas or air (Table 2.1), and M_i is the molecular mass (g mol^{-1}) of a gas.

Table 2.1: Molecular diffusion volumes (Reid et al., 1987) and masses used in this study.

Chemical species	Molecular mass (g mol^{-1})	Molecular diffusion volume
Ar	40	16.2
N_2	28	18.5
O_2	32	16.3
Air	28.95	19.7

For an ideal gas, d_i is given by

$$d_i \equiv \nabla C_i + (C_i - \omega_i)\frac{\nabla P}{P} - \frac{\rho_i}{P}\left(\frac{F_i}{M_i} - \sum_{j=1}^{n}\omega_i\frac{F_j}{M_j}\right) + \frac{k_i^T}{T}\nabla T, \tag{2.13}$$

where $\omega_i \equiv \frac{\rho_i}{\rho} = \frac{M_i C_i}{M_{\text{air}}}$ is the mass fraction of gas i, ρ_i is density of i (kg m^{-3}), P is pressure (Pa), T is temperature (K), k_i^T is the thermal-diffusion ratio of i, M_i is the molecular mass of i (kg mol^{-1}), and F_i the external body force per mole (N mol^{-1}) for i (Chapman et al., 1990; Taylor, 1953).

In the atmosphere, (vertical) pressure gradients are caused by gravity and well approximated by hydrostatic balance

$$\nabla P \approx \frac{\partial P}{\partial z} \approx -\rho g = -\frac{P M_{\text{air}}}{RT} g. \tag{2.14}$$

The gravitational force per mole F_i is

$$F_i = -\frac{\rho_i}{n_i} g. \tag{2.15}$$

Substituting Eqs. (2.14) and (2.15) into Eq. (2.13) yields

$$\begin{aligned} d_i &\approx \nabla C_i - \left(1 - \frac{M_i}{M_{\text{air}}}\right) C_i \frac{1}{P} \frac{P M_{\text{air}} g}{RT} \\ &+ \frac{\rho_i}{P} \left(\frac{\frac{\rho_i}{n_i} g}{M_i} - \sum_{j=1}^{n} \omega_j \frac{\frac{\rho_j}{n_j} g}{M_j} \right) + \frac{k_i^T}{T} \nabla T \\ &= \nabla C_i + \left(M_i - M_{\text{air}}\right) \frac{g}{RT} C_i + \frac{\rho_i}{P} \left(g - \sum_{j=1}^{n} \omega_i g \right) \\ &+ \frac{k_i^T}{T} \nabla T \\ &= \nabla C_i + \left(\frac{1}{H_i} - \frac{1}{H_{\text{air}}} \right) C_i + \frac{k_i^T}{T} \nabla T, \end{aligned} \tag{2.16}$$

where we use the definition of the scale height $H_i \equiv \frac{RT}{gM_i}$. The two terms involving the body force cancel because all species experience the same gravitational force per unit mass. The tendency for gravimetric separation instead arises from the pressure gradient term proportional to $\left(\frac{1}{H_i} - \frac{1}{H_{\text{air}}}\right)$.

Equations (2.8) and (2.9) can be inverted to solve for f_{N_2} and f_{Ar} (Taylor and Krishna, 1993):

$$f_{N_2} = -N D^{\text{air}}_{N_2} d_{N_2} - N D^{\text{air}}_{N_2 \times (Ar, O_2)} d_{\text{Ar}} \tag{2.17}$$

$$f_{\text{Ar}} = -N D^{\text{air}}_{Ar \times (N_2, O_2)} d_{N_2} - N D^{\text{air}}_{\text{Ar}} d_{\text{Ar}}, \tag{2.18}$$

where

$$D^{\text{air}}_{N_2} = \frac{D_{N_2:O2} \left(C_{N_2} D_{Ar:O_2} + \left(1 - C_{N_2}\right) D_{N_2:Ar} \right)}{S}, \tag{2.19}$$

$$D^{\text{air}}_{N_2 \times (Ar, O_2)} = \frac{C_{N_2} D_{Ar:O_2} \left(D_{N_2:O2} - D_{N_2:Ar} \right)}{S}, \tag{2.20}$$

$$D^{\text{air}}_{\text{Ar}} = \frac{D_{Ar:O_2} \left(C_{\text{Ar}} D_{N_2:O_2} + \left(1 - C_{\text{Ar}}\right) D_{N_2:Ar} \right)}{S}, \tag{2.21}$$

$$D^{\text{air}}_{Ar \times (N_2, O_2)} = \frac{C_{\text{Ar}} D_{N_2:O_2} \left(D_{Ar:O_2} - D_{N_2:Ar} \right)}{S}, \tag{2.22}$$

$$S = C_{N_2} D_{Ar:O_2} + C_{\text{Ar}} D_{N_2:O_2} + C_{O_2} D_{N_2:Ar}. \tag{2.23}$$

Here $D^{\rm air}_{N_2}$ and $D^{\rm air}_{\rm Ar}$ are the effective diffusivities of N_2 and Ar in air, while $D^{\rm air}_{N_2\times(Ar,O_2)}$ and $D^{\rm air}_{Ar\times(N_2,O_2)}$ reflect ternary cross-interactions, such as the tendency of N_2 to be impacted by any process that drives a diffusive flux of Ar.

In air, Ar is a minor gas ($C_{\rm Ar} \ll C_{N_2} \sim C_{O_2}$), and therefore interactions of N_2 with Ar can be neglected in the N_2 flux and the diffusive fluxes of N_2 and O_2 must balance approximately, as in the case of a binary mixture of the two gases:

$$f_{N_2} \approx -N D^{\rm air}_{N_2} d_{N_2}, \tag{2.24}$$

$$f_{O_2} \approx -f_{N_2}. \tag{2.25}$$

Combining Eqs. (2.17) and (2.25) with Eq. (2.16) yields

$$\begin{aligned} f_{N_2} \approx -N D^{\rm air}_{N_2} \Bigg[& \nabla C_{N_2} + \left(\frac{1}{H_{N_2}} - \frac{1}{H_{\rm air}} \right) C_{N_2} \\ & + \alpha^T_{N_2:O_2} \frac{C_{N_2}\left(1 - C_{N_2}\right)}{T} \nabla T \Bigg], \end{aligned} \tag{2.26}$$

$$\begin{aligned} f_{\rm Ar} \approx & -N D^{\rm air}_{Ar\times(N_2,O_2)} \Bigg[\nabla C_{N_2} + \left(\frac{1}{H_{N_2}} - \frac{1}{H_{\rm air}} \right) C_{N_2} \\ & + \alpha^T_{N_2:O_2} \frac{C_{N_2}\left(1 - C_{N_2}\right)}{T} \nabla T \Bigg] \\ & - N D^{\rm air}_{\rm Ar} \Bigg[\nabla C_{\rm Ar} + \left(\frac{1}{H_{\rm Ar}} - \frac{1}{H_{\rm air}} \right) C_{\rm Ar} \\ & + \alpha^T_{Ar:air} \frac{C_{\rm Ar}}{T} \nabla T \Bigg], \end{aligned} \tag{2.27}$$

where we have replaced the thermal diffusion ratio k^T_i with the better empirically constrained thermal diffusion factor $\alpha^T_i \equiv \frac{k^T_i}{C_i C_j}$ defined as such only in binary mixtures. Therefore, $k^T_{N_2} \approx \alpha^T_{N_2:O2} C_{N_2} C_{O_2}$ and $k^T_{\rm Ar} \approx \alpha^T_{Ar:air} C_{\rm Ar}$. Table 2.2 presents rough estimates of the magnitudes of the terms in Eqs. (2.26) and (2.27) in the stratosphere,

Table 2.2: Characteristic values of variables in Eqs. (2.26) and (2.27).

Variable/term	Magnitude in extratropics at			Units	Notes or Eq.
	$\sim$ 20 km	$\sim$ 35 km	$\sim$ 57 km		
P	50	5	0.3	mb	
T	215	235	255	K	c
$\frac{\partial T}{\partial z}$	3×10^{-4}	2.5×10^{-3}	2.4×10^{-3}	K m^{-1}	c
H_{N_2}	6.51×10^{3}	7.11×10^{3}	7.57×10^{3}	m	
H_{Ar}	4.56×10^{3}	4.98×10^{3}	5.30×10^{3}	m	
H_{air}	6.29×10^{3}	6.88×10^{3}	7.32×10^{3}	m	
$\alpha^T_{N_2:O_2}$		$< 1.8 \times 10^{-2}$		–	a
$\alpha^T_{Ar:air}$	$\sim 5.6 \times 10^{-2}$	$\sim 6.3 \times 10^{-2}$	$\sim 6.6 \times 10^{-2}$	–	b
C_{N_2}		78.09		%	
C_{O_2}		20.95		%	
C_{Ar}		0.93		%	
$\frac{\partial C_{N_2}}{\partial z}$	2.0×10^{-9}	2.6×10^{-9}	8.7×10^{-9}	m^{-1}	c
$\frac{\partial C_{\mathrm{Ar}}}{\partial z}$	2.7×10^{-10}	3.4×10^{-10}	11.6×10^{-10}	m^{-1}	c
$D^{\mathrm{air}}_{N_2}$	2.3×10^{-4}	2.7×10^{-3}	5.3×10^{-2}	m^2 s^{-1}	
$D^{\mathrm{air}}_{Ar\times(N_2,O_2)}$	9.8×10^{-9}	1.1×10^{-7}	2.2×10^{-6}	m^2 s^{-1}	
$D^{\mathrm{air}}_{\mathrm{Ar}}$	2.2×10^{-4}	2.6×10^{-3}	5.0×10^{-2}	m^2 s^{-1}	
$D^{\mathrm{air}}_{N_2} \frac{\partial C_{N_2}}{\partial z}$	4.7×10^{-13}	7.1×10^{-12}	4.6×10^{-10}	m s^{-1}	2.26
$D^{\mathrm{air}}_{N_2} \left(\frac{1}{H_{N_2}} - \frac{1}{H_{\mathrm{air}}}\right) C_{N_2}$	9.6×10^{-10}	11.0×10^{-8}	1.9×10^{-7}	m s^{-1}	2.26
$D^{\mathrm{air}}_{N_2} \alpha^T_{N_2:O_2} \frac{C_{N_2}\left(1-C_{N_2}\right)}{T} \frac{\partial T}{\partial z}$	$< 5.9 \times 10^{-12}$	$< 8.7 \times 10^{-11}$	$< 1.6 \times 10^{-9}$	m s^{-1}	2.26
$D^{\mathrm{air}}_{Ar\times(N_2,O_2)} \frac{\partial C_{N_2}}{\partial z}$	2.0×10^{-17}	3.0×10^{-16}	1.9×10^{-14}	m s^{-1}	2.27
$D^{\mathrm{air}}_{Ar\times(N_2,O_2)} \left(\frac{1}{H_{N_2}} - \frac{1}{H_{\mathrm{air}}}\right) C_{N_2}$	4.0×10^{-14}	4.3×10^{-13}	7.8×10^{-12}	m s^{-1}	2.27
$D^{\mathrm{air}}_{Ar\times(N_2,O_2)} \alpha^T_{N_2:O_2} \frac{C_{N_2}\left(1-C_{N_2}\right)}{T} \frac{\partial T}{\partial z}$	$< 2.5 \times 10^{-16}$	$< 3.6 \times 10^{-15}$	$< 6.8 \times 10^{-14}$	m s^{-1}	2.27
$D^{\mathrm{air}}_{\mathrm{Ar}} \frac{\partial C_{\mathrm{Ar}}}{\partial z}$	6.0×10^{-14}	8.9×10^{-13}	5.8×10^{-11}	m s^{-1}	2.27
$D^{\mathrm{air}}_{\mathrm{Ar}} \left(\frac{1}{H_{\mathrm{Ar}}} - \frac{1}{H_{\mathrm{air}}}\right) C_{\mathrm{Ar}}$	1.3×10^{-10}	1.3×10^{-9}	2.4×10^{-8}	m s^{-1}	2.27
$D^{\mathrm{air}}_{\mathrm{Ar}} \alpha^T_{Ar:air} \frac{C_{\mathrm{Ar}}}{T} \frac{\partial T}{\partial z}$	$\sim 9.8 \times 10^{13}$	$\sim 1.6 \times 10^{-11}$	$\sim 3.2 \times 10^{-10}$	m s^{-1}	2.27

[a] 1.8×10^{-2} observed at 293 K (Waldmann, 1947).
[b] Assuming $C_{\mathrm{Ar}} \approx \frac{N_{\mathrm{Ar}}}{N_{N_2}}$.
[c] Estimated from TOMCAT results.

showing that the thermal diffusion and cross-diffusion terms involving $D^{\text{air}}_{Ar\times(N_2,O_2)}$ are at least 2 orders of magnitude smaller than the remaining terms. Neglecting these smaller terms yields the governing Eq. (2.4) used in our model simulation:

$$\begin{aligned}\mathbf{f_i} &\approx -ND_i\left[\left(\frac{1}{H_i}-\frac{1}{H_{\text{air}}}\right)C_i\right]\\ &= -ND_i\Delta M_i\frac{g}{RT}C_i,\end{aligned} \tag{2.28}$$

where we introduced $\Delta M_i \equiv M_i - M_{\text{air}}$, the molecular mass difference to air (kg mol^{-1}), as a shorthand. Equation (2.28) is equally valid for trace gases such as Ar and major gases N_2 and O_2 when the appropriate diffusivities given by Eqs. (2.19) and (2.21) are used. In our case $D_{N_2} \equiv D^{\text{air}}_{N_2} = D^{\text{air}}_{O_2} \approx D_{N_2:O_2}$ for N_2 and $D_{\text{Ar}} \equiv D^{\text{air}}_{\text{Ar}} \approx \frac{D_{Ar:O_2}D_{N_2:Ar}}{C_{N_2}D_{Ar:O_2}+C_{O_2}D_{N_2:Ar}}$ for Ar.

2.9 Appendix C: Calculating $\delta(\text{Ar}/\text{N}_2)$ from δ(GST)

The conservation equation of gas i with mixing ratio C_i accounting for advection (first term RHS), eddy mixing (second term RHS), and molecular diffusion (third term RHS, using the simplified Eq. B21) is given by

$$\begin{aligned}\frac{\partial}{\partial t}(C_i) = &-\mathbf{u}\cdot\nabla[C_i] + \nabla\cdot[\mathbf{D}_e\nabla C_i]\\ &+\frac{\partial}{\partial z}\left[D_i\Delta M_i\frac{g}{RT}C_i\right],\end{aligned} \tag{2.29}$$

where $\mathbf{u}$ is the velocity vector (m s^{-1}), $\mathbf{D}_e$ is the eddy diffusivity tensor (m^2 s^{-1}), D_i is the molecular diffusivity of species i in air (i.e., D^{air}_i m^2 s^{-1}), g is the gravitational acceleration, R is the fundamental gas constant (J K^{-1} mol^{-1}), and T is temperature (K). "$\nabla\cdot$" represents the divergence operator. $\mathbf{u}$, $\mathbf{D}_e$, D_i, N, and T depend on x, y, z, and t and the largest gradients for these variables generally occur in the vertical direction.

Dividing Eq. (2.29) by a reference value $C_{i,0}$, separating C_i into a constant and a perturbation component (i.e., $\frac{C_i}{C_{i,0}} = 1 + \frac{C_i'}{C_{i,0}} = 1 + \delta_i$), and using the chain rule yields

$$\begin{aligned}\frac{\partial}{\partial t}\left(\delta_i\right) = &-\mathbf{u}\cdot\nabla\left[\delta_i\right] + \nabla\cdot\left[\mathbf{D}_e\nabla\delta_i\right] \\ &+ D_i\Delta M_i\frac{g}{RT}\frac{\partial}{\partial z}\left[\delta_i\right] + \left(1+\delta_i\right)\frac{\partial}{\partial z}\left[D_i\Delta M_i\frac{g}{RT}\right].\end{aligned} \tag{2.30}$$

To simplify Eq. (2.30), we assume that the perturbations in the mixing ratio are small (i.e., $\delta_i \ll 1$), which is true at the 1% level for $\delta(\mathrm{Ar}/\mathrm{N_2})$ even in the mesosphere. Furthermore, we assume that $U + \frac{D_e}{L} \gg \frac{D_i}{\Delta H_i}$ (U is a characteristic velocity scale, D_e is a characteristic eddy diffusivity, and L is a characteristic length scale; $\Delta H_i = \frac{RT}{\Delta M_i g}$) or, equivalently stated in terms of the Peclet number, $Pe \sim \frac{U\Delta H_i + D_e\frac{\Delta H_i}{L}}{D_i} \gg 1$. We estimate typical values of the vertical Peclet number in the stratosphere to be between 1000 and 10000 based on the height ($\sim$ 20 km) and turnover time ($\sim$ 5 years) of the stratosphere and the range of molecular diffusivities given in Table 2.2. In the mesosphere, AoA is near uniform, and we conservatively assume a turnover time of 0.5 years and a height of 20 km. This implies a Peclet number of $\sim$ 500 for the mesosphere. Under these conditions, the third term on the RHS can be eliminated because it is $O(Pe)$ smaller than the first and second terms and because it is $O(\delta_i)$ smaller than the fourth term. Thus, we obtain

$$\frac{\partial}{\partial t}\left(\delta_i\right) \approx -\mathbf{u}\cdot\nabla\left[\delta_i\right] + \nabla\cdot\left[\mathbf{D}_e\nabla\delta_i\right] + \frac{\partial}{\partial z}\left[D_i\Delta M_i\frac{g}{RT}\right], \tag{2.31}$$

where the last term approximates the vertical divergence of the gravitational flux. At the top of the atmosphere and Earth's surface, the gravitational flux abruptly vanishes, and its divergence becomes large. If its divergence is small in the interior, Eq. (2.31) can be conceptually interpreted as an advection–diffusion problem with large apparent sources or sinks at the bottom and top boundaries due to diffusive flux divergence. The steady-state solution to Eq. (2.31) for a tracer δ_i with no additional

sources and sinks (other than the apparent sources from diffusive flux divergence) yields the steady-state profile for species i. This solution can be scaled to yield the steady-state solution for any other tracer δ_j as

$$\delta_j \approx \frac{D_j \Delta M_j}{D_i \Delta M_i} \delta_i, \tag{2.32}$$

as can easily be validated by solving Eq. (C4) for δ_i and substitution into Eq. (2.31). Note that $\frac{D_j \Delta M_j}{D_i \Delta M_i}$ does not depend on x, y, and z.

Furthermore, ratios of passive tracers k and l can be calculated directly from δ_i by recognizing that $\delta_{k/l} \approx \delta_k - \delta_l$ for $\delta_k + \delta_l \ll 1$. Hence, we obtain the general version of Eq. (2.5) in the main text:

$$\delta_{k/l} \approx \delta_k - \delta_l \approx \frac{D_k^{\mathrm{air}} \Delta M_k - D_l^{\mathrm{air}} \Delta M_l}{D_i \Delta M_i} \delta_i. \tag{2.33}$$

2.10 Data availability

All data from the ORCAS, HIPPO, and ATom airborne campaigns are freely available at doi:10.5065/D6SB445X (Stephens, 2017), doi:10.3334/CDIAC/HIPPO_014 (Wofsy et al., 2017), and doi:10.3334/ornldaac/1581 (Wofsy et al., 2018). All of the primary data used here are consistent with the associated merged data products in Wofsy et al. (2017, 2018) and Stephens (2017). For Medusa samples identified as stratospheric, CO_2, $\delta(\mathrm{Ar}/\mathrm{N}_2)$, AoA, and kernel-averaged N_2O, O_3, H_2O, CO, CH_4, as well as additional metadata are available at doi:10.3334/ORNLDAAC/1788 (Birner et al., 2020). NIES TM modeling results (Belikov et al., 2019) and stratospheric observations of GS from the cryogenic balloon sampling system (Ishidoya et al., 2008, 2013, 2018; Sugawara et al., 2018) were provided directly by the authors.

2.11 Supplement availability

The supplement related to this article is available online at: https://doi.org/10.5194/acp-20-1-2020-supplement.

2.12 Acknowledgements

We would like to thank the pilots and crew of the GV and DC-8 research aircraft as well as NCAR and NASA project managers, field support staff, and logistics experts that were integral to the success of the ORCAS, HIPPO, and ATom campaigns. We are grateful to Andy Watt at NCAR, who helped prepare the Medusa sampler for the field and assisted with its operation. Bill Paplawsky, Sara Afshar, Shane Clark, Stephen Walker, and Adam Cox facilitated sample analysis, gas cylinder preparation, and data management and performed instrument maintenance at the Scripps Institution of Oceanography (SIO). Special thanks go to Eric Hintsa, Fred Moore, Jim Elkins, Mark Zondlo, Stuart Beaton, Minghui Diao, Glenn Diskin, Glen Sachse, Joshua DiGangi, John Nowak, James Flynn, Sergio Alvarez, Kathryn McKain, and Colm Sweeney for sharing O_3, N_2O, H_2O, CO, and CH_4 data used in this paper.

For the VCSEL hygrometer, field support, laboratory calibrations, and QA/QC were provided by Minghui Diao, Josh DiGangi, Mark Zondlo, and Stuart Beaton in HIPPO; Stuart Beaton provided field support and Minghui Diao provided laboratory calibrations and QA/QC in ORCAS.

This material is based upon work supported by the National Center for Atmospheric Research (NCAR), which is a major facility sponsored by the National Science Foundation (NSF) under cooperative agreement no. 1852977. The TOMCAT simulations were performed on the UK Archer and University of Leeds ARC HPC facilities. The modeling work in Leeds was supported by a NERC SISLAC. Martyn P. Chipperfield was also supported by a Royal Society Wolfson Merit award.

We thank Dimitry Belikov, Satoshi Sugawara, Shigeyuki Ishidoya, and colleagues for sharing the NIES TM modeling results and stratospheric observations from the balloon sampling system with us.

This research has been supported by NASA (grant nos. NNX17AE74G and NNX15AJ23G), the National Science Foundation (grant nos. ATM-0628575, ATM-0628519, ATM-0628388, AGS-1547797, AGS-1623748, 1501993, 1501997, 1501292, 1502301, and 1543457), and the Natural Environment Research Council (grant no. NE/R001782/1).

Chapter 2, in full, is a reprint of the material as it appears in Birner, B., Chipperfield, M.P., Morgan, E.J., Stephens, B.B., Linz, M., Feng, W., Wilson, C., Bent, J.D., Wofsy, S.C., Severinghaus, J., Keeling, R.F., 2020. Gravitational separation of $\delta(\mathrm{Ar}/\mathrm{N}_2)$ and age of air in the lowermost stratosphere in airborne observations and a chemical transport model. Atmospheric Chemistry and Physics 1–34. https://doi.org/https://doi.org/10.5194/acp-2020-95. The dissertation author was the primary investigator and author of this paper.

References

Andrews, A. E., Boering, K. A., Daube, B. C., Wofsy, S. C., Hintsa, E. J., Weinstock, E. M., and Bui, T. P.: Empirical age spectra for the lower tropical stratosphere from in situ observations of CO2: Implications for stratospheric transport, Journal of Geophysical Research Atmospheres, 104, 26 581–26 595, doi:10.1029/1999JD900150, 1999.

Andrews, A. E., Boering, K. A., Wofsy, S. C., Daube, B. C., Jones, D. B., Alex, S., Loewenstein, M., Podolske, J. R., and Strahan, S. E.: Empirical age spectra for the midlatitude lower stratosphere from in situ observations of CO2: Quantitative evidence for a subtropical "barrier" to horizontal transport, Journal of Geophysical Research Atmospheres, 106, 10 257–10 274, doi:10.1029/2000JD900703, 2001.

Baggenstos, D., Häberli, M., Schmitt, J., Shackleton, S. A., Birner, B., Severinghaus, J. P., Kellerhals, T., and Fischer, H.: Earth's radiative imbalance from the Last Glacial Maximum to the present, Proceedings of the National Academy of Sciences of the United States of America, 116, 14 881–14 886, doi:10.1073/pnas.1905447116, 2019.

Baldwin, M. P., Gray, L. J., Dunkerton, T. J., Hamilton, K., Haynes, P. H., Randel, W. J., Holton, J. R., Alexander, M. J., Hirota, I., Horinouchi, T., Jones, D. B. A., Kinnersley, J. S., Marquardt, C., Sato, K., and Takahashi, M.: The quasi-biennial oscillation, Reviews of Geophysics, 39, 179–229, doi:10.1029/1999RG000073, URL http://doi.wiley.com/10.1029/1999RG000073, 2001.

Banks, P. M. and Kockarts, G.: Aeronomy, Part B, Academic Press, New York, USA, 1 edn., 1973.

Belikov, D., Sugawara, S., Ishidoya, S., Hasebe, F., Maksyutov, S., Aoki, S., Morimoto, S., and Nakazawa, T.: Three-dimensional simulation of stratospheric gravitational separation using the NIES global atmospheric tracer transport model, Atmospheric Chemistry and Physics, 19, 5349–5361, doi:10.5194/acp-19-5349-2019, 2019.

Belikov, D. A., Maksyutov, S., Sherlock, V., Aoki, S., Deutscher, N. M., Dohe, S., Griffith, D., Kyro, E., Morino, I., Nakazawa, T., Notholt, J., Rettinger, M., Schneider, M., Sussmann, R., Toon, G. C., Wennberg, P. O., and Wunch, D.: Simulations of column-averaged CO2 and CH4 using the NIES TM with a hybrid sigma-isentropic (σ-θ) vertical coordinate, Atmospheric Chemistry and Physics, 13, 1713–1732, doi:10.5194/acp-13-1713-2013, 2013.

Bent, J. D.: Airborne Oxygen Measurements over the Southern Ocean as an Integrated Constraint of Seasonal Biogeochemical Processes, Phd dissertation, University of California San Diego, 2014.

Bereiter, B., Shackleton, S., Baggenstos, D., Kawamura, K., and Severinghaus, J.: Mean global ocean temperatures during the last glacial transition, Nature, 553, 39–44, doi:10.1038/nature25152, 2018.

Bieri, R. H. and Koide, M.: Noble gases in the atmosphere between 43 and 63 kilometers, Journal of Geophysical Research, 75, 6731–6735, doi:10.1029/jc075i033p06731, 1970.

Birner, B., Chipperfield, M. P., Morgan, E., and Keeling, R.: ATom: Age of Air, ArN2 Ratio, and Trace Gases in Stratospheric Samples, 2009-2018, doi:10.3334/ORNLDAAC/1788, 2020.

Blaine, T. W., Keeling, R. F., and Paplawsky, W. J.: An improved inlet for precisely measuring the atmospheric Ar/N2 ratio, Atmospheric Chemistry and Physics, 6, 1181–1184, doi:10.5194/acp-6-1181-2006, 2006.

Boering, K. A., Wofsy, S. C., Daube, B. C., Schneider, H. R., Loewenstein, M., Podolske, J. R., and Conway, T. J.: Stratospheric mean ages and transport rates from observations of carbon dioxide and nitrous oxide, Science, 274, 1340–1343, doi:10.1126/science.274.5291.1340, 1996.

Bönisch, H., Engel, A., Curtius, J., Birner, T., and Hoor, P.: Quantifying transport into the lowermost stratosphere using simultaneous in-situ measurements of SF6 and CO2, Atmospheric Chemistry and Physics, 9, 5905–5919, doi:10.5194/acp-9-5905-2009, 2009.

Brewer, A. W.: Evidence for a world circulation provided by the measurements of helium and water vapour distribution in the stratosphere, Quarterly Journal of the Royal Meteorological Society, 75, 351–363, doi:10.1002/qj.49707532603, 1949.

Butchart, N.: The Brewer-Dobson circulation, Reviews of Geophysics, 52, 157–184, doi:10.1002/2013RG000448, 2014.

Chabrillat, S., Vigouroux, C., Christophe, Y., Engel, A., Errera, Q., Minganti, D., Monge-Sanz, B. M., Segers, A., and Mahieu, E.: Comparison of mean age of air in five reanalyses using the BASCOE transport model, Atmospheric Chemistry and Physics, 18, 14 715–14 735, doi:10.5194/acp-18-14715-2018, 2018.

Chapman, S., Cowling, T. G., and Burnett, D.: The mathematical theory of non-uniform gases: an account of the kinetic theory of viscosity, thermal conduction and diffusion in gases, Cambridge University Press, 3 edn., 1990.

Chipperfield, M. P.: New version of the TOMCAT/SLIMCAT off-line chemical transport model: Intercomparison of stratospheric tracer experiments, Quarterly Journal of the Royal Meteorological Society, 132, 1179–1203, doi:10.1256/qj.05.51, 2006.

Chipperfield, M. P., Bekki, S., Dhomse, S., Harris, N. R., Hassler, B., Hossaini, R., Steinbrecht, W., Thiéblemont, R., and Weber, M.: Detecting recovery of the stratospheric ozone layer, Nature, 549, 211–218, doi:10.1038/nature23681, URL http://dx.doi.org/10.1038/nature23681, 2017.

Diskin, G. S., Podolske, J. R., Sachse, G. W., and Slate, T. A.: Open-path airborne tunable diode laser hygrometer, in: Diode Lasers and Applications in Atmospheric Sensing, edited by Fried, A., pp. 196–204, Proceedings of the Society of Photo-Optical Instrumentation Engineers (SPIE), doi:10.1117/12.453736, 2002.

Dobson, G. M. B.: Origin and distribution of the polyatomic molecules in the atmosphere, Proceedings of the Royal Society of London. Series A. Mathematical and Physical Sciences, 236, 187–193, doi:10.1098/rspa.1956.0127, 1956.

Engel, A., Möbius, T., Bönisch, H., Schmidt, U., Heinz, R., Levin, I., Atlas, E., Aoki, S., Nakazawa, T., Sugawara, S., Moore, F., Hurst, D., Elkins, J., Schauffler, S.,

Andrews, A., and Boering, K.: Age of stratospheric air unchanged within uncertainties over the past 30 years, Nature Geoscience, 2, 28–31, doi:10.1038/ngeo388, 2009.

Engel, A., Bönisch, H., Ullrich, M., Sitals, R., Membrive, O., Danis, F., and Crevoisier, C.: Mean age of stratospheric air derived from AirCore observations, Atmospheric Chemistry and Physics, 17, 6825–6838, doi:10.5194/acp-17-6825-2017, 2017.

Flury, T., Wu, D. L., and Read, W. G.: Variability in the speed of the Brewer-Dobson circulation as observed by Aura/MLS, Atmospheric Chemistry and Physics, 13, 4563–4575, doi:10.5194/acp-13-4563-2013, 2013.

Green, P. J.: Reversible jump Markov chain monte carlo computation and Bayesian model determination, Biometrika, 82, 711–732, doi:10.1093/biomet/82.4.711, 1995.

Hall, T. M. and Plumb, R. A.: Age as a diagnostic of stratospheric transport, Journal of Geophysical Research, 99, 1059–1070, doi:10.1029/93JD03192, 1994.

Hastings, W. K.: Monte carlo sampling methods using Markov chains and their applications, Biometrika, 57, 97–109, doi:10.1093/biomet/57.1.97, 1970.

Hauck, M., Fritsch, F., Garny, H., and Engel, A.: Deriving stratospheric age of air spectra using an idealized set of chemically active trace gases, Atmospheric Chemistry and Physics, 19, 5269–5291, doi:10.5194/acp-19-5269-2019, 2019.

Hauck, M., Bönisch, H., Hoor, P., Keber, T., Ploeger, F., Schuck, T. J., and Engel, A.: A convolution of observational and model data to estimate age of air spectra in the northern hemispheric lower stratosphere, Atmospheric Chemsitry and Physics Discussions, in review, doi:10.5194/acp-2020-167, 2020.

Haynes, P.: Stratospheric Dynamics, Annual Review of Fluid Mechanics, 37, 263–293, doi:10.1146/annurev.fluid.37.061903.175710, 2005.

Headly, M. A. and Severinghaus, J. P.: A method to measure Kr/N2 ratios in air bubbles trapped in ice cores and its application in reconstructing past mean ocean temperature, Journal of Geophysical Research, 112, 1–12, doi:10.1029/2006JD008317, 2007.

Holton, J. R., Haynes, P. H., Mcintyre, M. E., Douglass, A. R., and Rood, B.: Stratosphere-Troposphere, Review of Geophysics, pp. 403–439, 1995.

Hoor, P., Gurk, C., Brunner, D., Hegglin, M. I., Wernli, H., and Fischer, H.: Seasonality and extent of extratropical TST derived from in-situ CO measurements during SPURT, Atmospheric Chemistry and Physics Discussions, 4, 1427–1442, doi:10.5194/acpd-4-1691-2004, 2004.

Ishidoya, S., Sugawara, S., Morimoto, S., Aoki, S., and Nakazawa, T.: Gravitational separation of major atmospheric components of nitrogen and oxygen in the stratosphere, Geophysical Research Letters, 35, doi:10.1029/2007GL030456, 2008.

Ishidoya, S., Sugawara, S., Morimoto, S., Aoki, S., Nakazawa, T., Honda, H., and Murayama, S.: Gravitational separation in the stratosphere - A new indicator of atmospheric circulation, Atmospheric Chemistry and Physics, 13, 8787–8796, doi:10.5194/acp-13-8787-2013, 2013.

Ishidoya, S., Sugawara, S., Inai, Y., Morimoto, S., Honda, H., Ikeda, C., Hashida, G., Machida, T., Tomikawa, Y., Toyoda, S., Goto, D., Aoki, S., and Nakazawa, T.: Gravitational separation of the stratospheric air over Syowa, Antarctica and its connection with meteorological fields, Atmospheric Science Letters, 19, 1–7, doi:10.1002/asl.857, 2018.

Karion, A., Sweeney, C., Wolter, S., Newberger, T., Chen, H., Andrews, A., Kofler, J., Neff, D., and Tans, P.: Long-term greenhouse gas measurements from aircraft, Atmospheric Measurement Techniques, 6, 511–526, doi:10.5194/amt-6-511-2013, 2013.

Keeling, C. D., Stephen, C., Piper, S. C., Bacastow, R. B., Wahlen, M., Whorf, T. P., Heimann, M., and Meijer, H. A.: Exchanges of atmospheric CO2 and 13CO2 with the terrestrial biosphere and oceans from 1978 to 2000, 2001.

Keeling, R. F.: Development of an interferometric oxygen analyzer for precise measurement of the atmospheric O2 mole fraction, Ph.D. thesis, Harvard University, 1988.

Keeling, R. F., Blaine, T., Paplawsky, B., Katz, L., Atwood, C., and Brockwell, T.: Measurement of changes in atmospheric Ar/N_2 ratio using a rapid-switching, single-capillary mass spectrometer system, Tellus, 56B, 322–338, doi:10.1111/j.1600-0889.2004.00117.x, 2004.

Kovács, T., Feng, W., Totterdill, A., Plane, J. M., Dhomse, S., Gómez-Martín, J. C., Stiller, G. P., Haenel, F. J., Smith, C., Forster, P. M., García, R. R., Marsh, D. R., and Chipperfield, M. P.: Determination of the atmospheric lifetime and global warming potential of sulfur hexafluoride using a three-dimensional model, Atmospheric Chemistry and Physics, 17, 883–898, doi:10.5194/acp-17-883-2017, 2017.

Krol, M., De Bruine, M., Killaars, L., Ouwersloot, H., Pozzer, A., Yin, Y., Chevallier, F., Bousquet, P., Patra, P., Belikov, D., Maksyutov, S., Dhomse, S., Feng, W., and Chipperfield, M. P.: Age of air as a diagnostic for transport timescales in global models, Geoscientific Model Development, 11, 3109–3130, doi:10.5194/gmd-11-3109-2018, 2018.

Li, F., Waugh, D. W., Douglass, A. R., Newman, P. A., Pawson, S., Stolarski, R. S., Strahan, S. E., and Nielsen, J. E.: Seasonal variations of stratospheric age spectra in the Goddard Earth Observing System Chemistry Climate Model (GEOSCCM), Journal of Geophysical Research Atmospheres, 117, 1–14, doi:10.1029/2011JD016877, 2012.

Linz, M., Plumb, R. A., Gerber, E. P., and Sheshadri, A.: The relationship between age of air and the diabatic circulation of the stratosphere, Journal of the Atmospheric Sciences, 73, 4507–4518, doi:10.1175/JAS-D-16-0125.1, 2016.

Linz, M., Plumb, R. A., Gerber, E. P., Haenel, F. J., Stiller, G., Kinnison, D. E., Ming, A., and Neu, J. L.: The strength of the meridional overturning circulation of the stratosphere, Nature Geoscience, 10, 663–667, doi:10.1038/ngeo3013, 2017.

Malinverno, A.: Parsimonious Bayesian Markov chain Monte Carlo inversion in a nonlinear geophysical problem, Geophysics Journal International, 151, 675–688, 2002.

Metropolis, N., Rosenbluth, A. W., Rosenbluth, M. N., Teller, A. H., and Teller, E.: Equation of state calculations by fast computing machines, The Journal of Chemical Physics, 21, 1087–1092, doi:10.1063/1.1699114, 1953.

Monge-Sanz, B. M., Chipperfield, M. P., Simmons, A. J., and Uppala, S. M.: Mean age of air and transport in a CTM: Comparison of different ECMWF analyses, Geophysical Research Letters, 34, 1–5, doi:10.1029/2006GL028515, 2007.

Montzka, S. A., Dutton, G. S., Yu, P., Ray, E., Portmann, R. W., Daniel, J. S., Kuijpers, L., Hall, B. D., Mondeel, D., Siso, C., Nance, J. D., Rigby, M., Manning, A. J., Hu, L., Moore, F., Miller, B. R., and Elkins, J. W.: An unexpected and persistent increase in global emissions of ozone-depleting CFC-11, Nature, 557, 413–417, doi:10.1038/s41586-018-0106-2, 2018.

Morgan, E. J., Stephens, B. B., Birner, B., and Keeling, R. F.: Observational Constraints on the Vertical and Interhemispheric Gradient of the Ar/N2 Ratio in the Troposphere, in: Abstract CT14A-0845 presented at Ocean Sciences Meeting 2020, AGU, San Diego, 2020.

Plumb, R. A.: Tracer interrelationships in the stratosphere, Reviews of Geophysics, 45, 1–33, doi:10.1029/2005RG000179, 2007.

Podglajen, A. and Ploeger, F.: Retrieving the age of air spectrum from tracers: Principle and method, Atmospheric Chemistry and Physics, 19, 1767–1783, doi:10.5194/acp-19-1767-2019, 2019.

Prather, M. J., Zhu, X., Flynn, C. M., Strode, S. A., Rodriguez, J. M., Steenrod, S. D., Liu, J., Lamarque, J. F., Fiore, A. M., Horowitz, L. W., Mao, J., Murray, L. T., Shindell, D. T., and Wofsy, S. C.: Global atmospheric chemistry - Which air matters, Atmospheric Chemistry and Physics, 17, 9081–9102, doi:10.5194/acp-17-9081-2017, 2017.

Ray, E. A., Moore, F. L., Elkins, J. W., Dutton, G. S., Fahey, D. W., Vömel, H., Oltmans, S. J., and Rosenlof, K. H.: Transport into the Northern Hemisphere lowermost stratosphere revealed by in situ tracer measurements, Journal of Geophysical Research Atmospheres, 104, 26 565–26 580, doi:10.1029/1999JD900323, 1999.

Ray, E. A., Moore, F. L., Rosenlof, K. H., Davis, S. M., Boenisch, H., Morgenstern, O., Smale, D., Rozanov, E., Hegglin, M., Pitari, G., Mancini, E., Braesicke, P., Butchart, N., Hardiman, S., Li, F., Shibata, K., and Plummer, D. A.: Evidence for changes in stratospheric transport and mixing over the past three decades based on multiple data sets and tropical leaky pipe analysis, Journal of Geophysical Research Atmospheres, 115, 1–16, doi:10.1029/2010JD014206, 2010.

Ray, E. A., Moore, F. L., Rosenlof, K. H., Davis, S. M., Sweeney, C., Tans, P., Wang, T., Elkins, J. W., Bönisch, H., Engel, A., Sugawara, S., Nakazawa, T., and Aoki, S.: Improving stratospheric transport trend analysis based on SF6 and CO2 measurements, Journal of Geophysical Research: Atmospheres, 119, 14 110–14 128, doi:10.1002/2014JD021802, 2014.

Reid, R. C., Prausnitz, J. M., and Poling, B. E.: The properties of gases and liquids, McGraw-Hill, New York, 4 edn., 1987.

Ritz, S. P., Stocker, T. F., and Severinghaus, J. P.: Noble gases as proxies of mean ocean temperature: Sensitivity studies using a climate model of reduced complexity, Quaternary Science Reviews, 30, 3728–3741, doi:10.1016/j.quascirev.2011.09.021, 2011.

Salby, M. L. and Callaghan, P. F.: Influence of the Brewer-Dobson circulation on stratosphere-troposphere exchange, Journal of Geophysical Research Atmospheres, 111, 1–9, doi:10.1029/2006JD007051, 2006.

Santoni, G. W., Daube, B. C., Kort, E. A., Jiménez, R., Park, S., Pittman, J. V., Gottlieb, E., Xiang, B., Zahniser, M. S., Nelson, D. D., Mcmanus, J. B., Peischl, J., Ryerson, T. B., Holloway, S., Andrews, A. E., Sweeney, C., Hall, B., Hintsa, E. J., Moore, F. L., Elkins, J. W., Hurst, D. F., Stephens, B. B., Bent, J., and Wofsy, S. C.: Evaluation of the airborne quantum cascade laser spectrometer (QCLS) measurements of the carbon and greenhouse gas suite - CO2, CH4, N2O, and CO - during the CalNex and HIPPO Campaigns, Atmospheric Measurement Techniques, 7, 1509–1526, doi:10.5194/amt-7-1509-2014, 2014.

Schoeberl, M. R., Douglass, A. R., Polansky, B., Bonne, C., Walker, K. A., and Bernath, P.: Estimation of stratospheric age spectrum from chemical tracers, Journal of Geophysical Research Atmospheres, 110, 1–18, doi:10.1029/2005JD006125, 2005.

Seltzer, A. M., Ng, J., Danskin, W. R., Kulongoski, J. T., Gannon, R. S., Stute, M., and Severinghaus, J. P.: Deglacial water-table decline in Southern California recorded by noble gas isotopes, Nature Communications, 10, 1–6, doi:10.1038/s41467-019-13693-2, 2019.

Škerlak, B., Sprenger, M., and Wernli, H.: A global climatology of stratosphere-troposphere exchange using the ERA-Interim data set from 1979 to 2011, Atmospheric Chemistry and Physics, 14, 913–937, doi:10.5194/acp-14-913-2014, 2014.

Stephens, B. B.: ORCAS Merge Products. Version 1.0, doi:10.5065/D6SB445X, URL https://data.eol.ucar.edu/dataset/490.024, 2017.

Stephens, B. B., Long, M. C., Keeling, R. F., Kort, E. A., Sweeney, C., Apel, E. C., Atlas, E. L., Beaton, S., Bent, J. D., Blake, N. J., Bresch, J. F., Casey, J., Daube, B. C., Diao, M., Diaz, E., Dierssen, H., Donets, V., Gao, B. C., Gierach, M., Green, R., Haag, J., Hayman, M., Hills, A. J., Hoecker-Martínez, M. S., Honomichl, S. B., Hornbrook, R. S., Jensen, J. B., Li, R. R., McCubbin, I., McKain, K., Morgan, E. J., Nolte, S., Powers, J. G., Rainwater, B., Randolph, K., Reeves, M., Schauffler, S. M., Smith, K., Smith, M., Stith, J., Stossmeister, G., Toohey, D. W., and Watt, A. S.: The O2/N2 ratio and CO2 airborne Southern Ocean study, Bulletin of the American Meteorological Society, 99, 381–402, doi:10.1175/BAMS-D-16-0206.1, 2018.

Stephens, B. B., Morgan, E. J., Bent, J. D., Keeling, R. F., Watt, A. S., Shertz, S. R., and Daube, B. C.: Airborne measurements of oxygen concentration from the surface to the lower stratosphere and pole to pole, Atmospheric Measurement Techniques Discussions, pp. 1–39, doi:10.5194/amt-2020-294, 2020.

Strahan, S. E., Douglass, A. R., Stolarski, R. S., Akiyoshi, H., Bekki, S., Braesicke, P., Butchart, N., Chipperfield, M. P., Cugnet, D., Dhomse, S., Frith, S. M., Gettelman, A., Hardiman, S. C., Kinnison, D. E., Lamarque, J. F., Mancini, E.,

Marchand, M., Michou, M., Morgenstern, O., Nakamura, T., Olivié, D., Pawson, S., Pitari, G., Plummer, D. A., Pyle, J. A., Scinocca, J. F., Shepherd, T. G., Shibata, K., Smale, D., Teyssèdre, H., Tian, W., and Yamashita, Y.: Using transport diagnostics to understand chemistry climate model ozone simulations, Journal of Geophysical Research Atmospheres, 116, 1–18, doi:10.1029/2010JD015360, 2011.

Sugawara, S., Ishidoya, S., Aoki, S., Morimoto, S., Nakazawa, T., Toyoda, S., Inai, Y., Hasebe, F., Ikeda, C., Honda, H., Goto, D., and Putri, F. A.: Age and gravitational separation of the stratospheric air over Indonesia, Atmospheric Chemistry and Physics, 18, 1819–1833, doi:10.5194/acp-18-1819-2018, 2018.

Taylor, G.: Dispersion of Soluble Matter in Solvent Flowing Slowly through a Tube, Proceedings of the Royal Society A: Mathematical, Physical and Engineering Sciences, 219, 186–203, doi:10.1098/rspa.1953.0139, URL http://rspa.royalsocietypublishing.org/cgi/doi/10.1098/rspa.1953.0139, 1953.

Taylor, R. and Krishna, R.: Multicomponent mass transfer, vol. 2, John Wiley & Sons, 2 edn., 1993.

Waugh, D.: Atmospheric dynamics: The age of stratospheric air, Nature Geoscience, 2, 14–16, doi:10.1038/ngeo397, 2009.

Waugh, D. W. and Hall, T. M.: Age of stratospheric air: Theory, observations, and models, Reviews of Geophysics, 40, doi:10.1029/2000RG000101, 2002.

Wofsy, S. C., the HIPPO science team, modelers, C., and teams, S.: HIAPER Pole-to-Pole Observations (HIPPO): Fine-grained, global-scale measurements of climatically important atmospheric gases and aerosols, Philosophical Transactions of the Royal Society A: Mathematical, Physical and Engineering Sciences, 369, 2073–2086, doi:10.1098/rsta.2010.0313, 2011.

Wofsy, S. C., Daube, B. C., Jimenez, R., Kort, E., Pittman, J. V., Park, S., Commane, R., Xiang, B., Santoni, G., Jacob, D., Fisher, J., Pickett-Heaps, C., Wang, H., Wecht, K., Wang, Q.-Q., Stephens, B. B., Shertz, S., Watt, A., Romashkin, P., Campos, T., Haggerty, J., Cooper, W. A., Rogers, D., Beaton, S., Hendershot, R., Elkins, J. W., Fahey, D. W., Gao, R. S., Moore, F., Montzka, S. A., Schwarz, J. P., Perring, A. E., Hurst, D., Miller, B. R., Sweeney, C., Oltmans, S., Nance, D., Hintsa, E., Dutton, G., Watts, L. A., Spackman, J. R., Rosenlof, K. H., Ray, E. A., Hall, B., Zondlo, M. A., Diao, M., Keeling, R., Bent, J., Atlas, E. L., Lueb, R., and Mahoney, M. J.: HIPPO MEDUSA Flask Sample Trace Gas and Isotope Data, doi:10.3334/CDIAC/HIPPO_014, URL https://hippo.ornl.gov/data{_}access, 2017.

Wofsy, S. C., Afshar, S., Allen, H. M., Apel, E., Asher, E. C., Barletta, B., Bent, J., Bian, H., Biggs, B. C., Blake, D. R., Blake, N., Bourgeois, I., Brock, C. A., Brune, W. H., Budney, J. W., Bui, T. P., Butler, A., Campuzano-Jost, P., Chang, C. S., Chin, M., Commane, R., Correa, G., Crounse, J. D., Cullis, P. D., Daube, B. C., Day, D. A., Dean-Day, J. M., Dibb, J. E., Digangi, J. P., Diskin, G. S., Dollner, M., Elkins, J. W., Erdesz, F., Fiore, A. M., Flynn, C. M., Froyd, K., Gesler, D. W., Hall, S. R., Hanisco, T. F., Hannun, R. A., Hills, A. J., Hintsa, E. J., Hoffman, A., Hornbrook, R. S., Huey, L. G., Hughes, S., Jimenez, J. L., Johnson, B. J., Katich, J. M., Keeling, R., Kim, M. J., Kupc, A., Lait, L. R., Lamarque, J. F., Liu, J., McKain, K., McLaughlin, R. J., Meinardi, S., Miller, D. O., Montzka, S. A., Moore, F. L., Morgan, E. J., Murphy, D. M., Murray, L. T., Nault, B. A., Neuman, J. A., Newman, P. A., Nicely, J. M., Pan, X., Paplawsky, W., Peischl, J., Prather, M. J., Price, D. J., Ray, E., Reeves, J. M., Richardson, M., Rollins, A. W., Rosenlof, K. H., Ryerson, T. B., Scheuer, E., Schill, G. P., Schroder, J. C., Schwarz, J. P., St.Clair, J. M., Steenrod, S. D., Stephens, B. B., Strode, S. A., Sweeney, C., Tanner, D., Teng, A. P., Thames, A. B., Thompson, C. R., Ullmann, K., Veres, P. R., Vizenor, N., Wagner, N. L., Watt, A., Weber, R., Weinzierl, B.,

Wennberg, P., Williamson, C. J., Wilson, J. C., Wolfe, G. M., Woods, C. T., and Zeng, L. H.: ATom: Merged Atmospheric Chemistry, Trace Gases, and Aerosols, doi:10.3334/ornldaac/1581, 2018.

Zondlo, M. A., Paige, M. E., Massick, S. M., and Silver, J. A.: Vertical cavity laser hygrometer for the National Science Foundation Gulfstream-V aircraft, Journal of Geophysical Research Atmospheres, 115, 1–14, doi:10.1029/2010JD014445, 2010.

Chapter 3

Measurements of atmospheric He/N_2 as an indicator of fossil fuel extraction and stratospheric circulation

3.1 Abstract

The atmospheric He/N_2 ratio is expected to be increasing due to the emission of He associated with fossil fuels and is expected to also vary in both space and time due to gravitational separation in the stratosphere. These signals may be useful indicators of fossil-fuel exploitation and variability in stratospheric circulation, but direct measurements of He/N_2 ratio are lacking on all time scales. Here we present a high-precision custom inlet system for mass spectrometers that continuously stabilizes the flow of gas during sample-standard comparison and removes all non-noble gases from the gas stream, enabling unprecedented accuracy in measurement of relative changes in the $^4He/N_2$ ratio. Repeat measurements of the same combination of

high-pressure tanks using our inlet system achieves a reproducibility of ∼10 per meg (i.e. 0.001%) in 6–8h analyses. This compares to interannual changes of He/N_2 gravitational enrichment at ∼35 km in the mid latitude stratosphere of order 300–400 per meg, and an annual tropospheric increase from human fossil fuel activity of less than ∼30 per meg y^{-1} (bounded by previous work on helium isotopes). The gettering and flow-stabilizing inlet may also be used for the analysis of other noble gas isotopes and could resolve previously unobserved seasonal cycles in Kr/N_2 and Xe/N_2.

3.2 Introduction

The atmospheric mole fraction of helium in dry air is typical ∼5.24 ppm (Glückauf, 1944) with an isotopic abundance of ^4He about 10^6 times greater than ^3He. On geological time scales, the natural concentration of ^4He in the atmosphere is set by a balance of ^4He loss to space and ^4He release from the Earth's crust, where it is produced by radioactive decay of uranium and thorium (Kockarts, 1973; Pierson-Wickmann et al., 2001; Zartman et al., 1961; Sano et al., 2013). Over the past century, human exploitation of fossil fuels likely has accelerated the release of crustal He, but the observational evidence of a secular increase of atmospheric ^4He remains ambiguous presumably due to a lack of analytical precision (Boucher et al., 2018c; Lupton and Evans, 2013, 2004; Mabry et al., 2015; Oliver et al., 1984; Sano et al., 1989). Additionally, recent measurements and model simulations reveal a small depletion of gases heavier than air in the stratosphere by gravitational separation (Belikov et al., 2019; Birner et al., 2020; Ishidoya et al., 2020, 2018, 2013; Sugawara et al., 2018) suggesting a corresponding enrichment of the light gas helium. Gravitational separation is only partially counteracted by the large-scale stratospheric circulation and mixing, which tends to homogenize the atmosphere. Variability in stratospheric circulation and stratosphere-troposphere exchange (STE) could therefore impact the

degree of fractionation and cause additional interannual changes in the stratospheric and, to a much lesser extent, the tropospheric abundance of ^{4}He.

Measurements of He/N_2 may provide an alternative indicator of variations in stratospheric circulation and STE. An improved understanding of STE is critical because stratospheric circulation changes affect tropospheric trends of societally-important trace and greenhouse gases such as N_2O, CH_4, ^{14}C, O_3 and CFCs (Arblaster et al., 2014; Graven et al., 2012; Hamilton and Fan, 2000; Hegglin and Shepherd, 2009; Montzka et al., 2018; Nevison et al., 2011; Simmonds et al., 2013). These gases all have significant sources or sinks in the stratosphere that cause strong stratosphere-troposphere concentration differences. Global circulation models consistently predict an acceleration of the stratospheric Brewer-Dobson Circulation (BDC; Brewer, 1949; Dobson, 1956) under global warming (Butchart, 2014). Stratospheric circulation is also naturally modulated on a range of shorter time scales from synoptic-scale events to decadal variations (e.g., Holton et al., 1995; Li et al., 2012; Flury et al., 2013; Butchart, 2014; Ray et al., 2014). Circulation changes have typically been observed using measurements of numerous different trace gases in the stratosphere (e.g., Ar/N_2, SF_6, H_2O, O_3, CO, or N_2O) (e.g., Bönisch et al., 2009; Engel et al., 2009, 2017; Ray et al., 2010; Haenel et al., 2015). However, interpretation of these tracers of stratospheric circulation is complicated by complex chemical source and sink processes, whereas gravitational fractionation of He/N_2 is governed by comparatively simple physics.

Atmospheric He/N_2 measurements may also provide an indication of the history of fossil-fuel usage. Previous attempts to measure the fossil-fuel signal in He have centered on measurements of changes in the atmospheric ^{3}He/^{4}He isotope ratio (Boucher et al., 2018c; Lupton and Evans, 2013, 2004; Oliver et al., 1984; Sano et al., 1989). However, measurements of the ^{3}He/^{4}He ratio are fundamentally limited by the extremely low abundance of ^{3}He (e.g. Mabry et al., 2015; Boucher et al., 2018c), with only 1 in 730,000 He atoms being ^{3}He. Therefore, the precision on individ-

ual $^3He/^4He$ analyses is limited to $\sim \pm 0.2\%$. This is insufficient for the detection of the stratospheric and anthropogenic signals we are interested in, and which we estimate to cause variations in the atmospheric ^4He mole fraction on the order of 0.003 to 0.04% y^{-1} (see section 3.2.1 & 3.2.2). Moreover, small changes in ^3He from radioactive decay of tritium in nuclear warheads may complicate the interpretation of $^3He/^4He$ results (e.g., Boucher et al., 2018c; Lupton and Evans, 2004). Here we describe a method to measure relative differences in ^4He mole fraction ($^4He/M$) between two large samples of air using a custom mass spectrometer inlet system. The helium mole fraction can later be mathematically translated to our target ratio, $^4He/N_2$, given supplementary measurements of O_2, Ar, and Ar/N_2 (see discussion). This is advantageous because N_2 is near-constant in the atmosphere making $^4He/N_2$ more readily interpretable than $^4He/M$. The $^4He/M$ method depends on stabilization of the air flow to the ion source between a sample and standard gas to achieve high precision differencing. Novel elements in our setup include continuous flow removal of reactive gases via titanium gettering immediately upstream of the mass spectrometer inlet, and the use of an actively-controlled open split (Henneberg et al., 1975) for balancing pressures upstream of a shared capillary directed towards the mass spectrometer. Gas handling techniques, the inlet system and the continuous-flow getter oven are described in detail below.

3.2.1 Gravitational fractionation of He/N_2 in the stratosphere

The notion that the stratospheric and tropospheric He/N_2 ratio must vary in response to fluctuations in stratospheric circulation is based on studies of the atmospheric Ar/N_2 ratio (Birner et al., 2020; Ishidoya et al., 2020). Relative changes in the Ar/N_2 ratio (or He/N_2) are commonly expressed in delta notation:

$$\delta(Ar/N_2) = \frac{(Ar/N_2)_{SA}}{(Ar/N_2)_{ST}} - 1 \tag{3.1}$$

where subscripts SA and ST refer to the ratio in a sample and a reference gas mixture, respectively. $\delta(\mathrm{Ar/N_2})$ is multiplied by 10^6 and expressed in "per meg" units.

Sensitivity tests with the 2-D chemical-dynamical-radiative model of the atmosphere SOCRATES by Ishidoya et al. (2020) indicate that significant temporal changes in stratospheric $\mathrm{Ar/N_2}$ should occur in response to an acceleration or deceleration of the BDC. The simulations also suggest a weak stratospheric influence on tropospheric $\mathrm{Ar/N_2}$. Ishidoya et al. find that imposing a gradual acceleration of the BDC of 4% dec^{-1} leads to a 40 per meg dec^{-1} increase in $\delta(\mathrm{Ar/N_2})$ at ∼35 km altitude in northern mid-latitudes, and a corresponding 1.3 per meg dec^{-1} decrease of $\delta(\mathrm{Ar/N_2})$ in the troposphere. Furthermore, they find that imposing 3-year periodic changes of 10% in BDC yields anomalies of ±25 and ±0.4 per meg in stratospheric and tropospheric $\delta(\mathrm{Ar/N_2})$, respectively. Tropospheric observations of $\delta(\mathrm{Ar/N_2})$ by Ishidoya et al. (2020) would be consistent with larger STE-induced interannual changes of tropospheric $\mathrm{Ar/N_2}$. Variability of the BDC on the order of 10% or more on seasonal to decadal time scales is consistent with published estimates (Flury et al., 2013; Ray et al., 2014; Salby and Callaghan, 2006).

The atmospheric $\mathrm{He/N_2}$ ratio must be more strongly impacted by gravitational fractionation than $\mathrm{Ar/N_2}$ due to the larger mass difference and higher diffusivity of He than Ar, which brings He closer to gravitational equilibrium. The gravitational fractionation effect on $\mathrm{He/N_2}$ can be scaled from $\mathrm{Ar/N_2}$ (Birner et al., 2020) using the molar mass difference to air ΔM_i ($\Delta M_i = M_i - 0.02896$ kg mol^{-1}) and the molecular diffusivity D_i of gas i in air as:

$$\delta(He/N_2) = \frac{(He/N_2)_{SA}}{(He/N_2)_{ST}} - 1 \approx \frac{D^{air}_{He}\Delta M_{He} - D^{air}_{N_2}\Delta M_{N_2}}{D^{air}_{Ar}\Delta M_{Ar} - D^{air}_{N_2}\Delta M_{N_2}}\delta(Ar/N_2). \tag{3.2}$$

Using the method of Fuller et al. as reported in (Reid et al., 1987), D_{He} is 3.6 times greater than D_{Ar} and ΔM is more than twice as large, making $\delta(\mathrm{He/N_2})$ ∼7.5 times more strongly fractionated by gravity than $\delta(\mathrm{Ar/N_2})$ in the stratosphere.

3.2.2 Other controls on tropospheric He/N_2

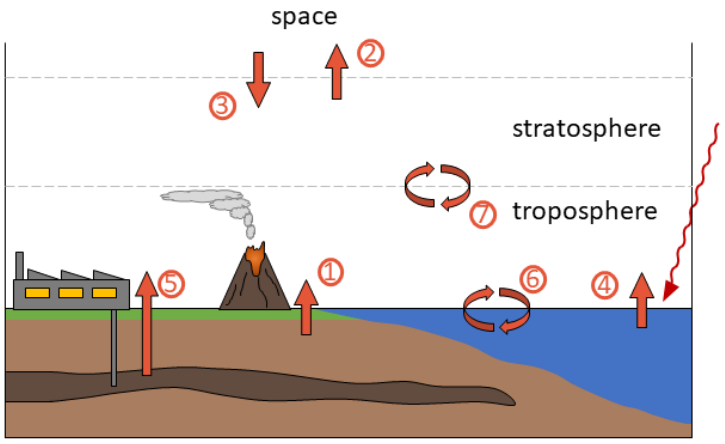

Figure 3.1: Schematic depiction of ^{4}He fluxes to and from the troposphere. Different processes are numbered and listed in Table 1.

A variety of known natural processes influence tropospheric $^4He/N_2$ is summarized in Figure 3.1 and Table 3.1. Natural ^{4}He release from the Earth's crust is mediated by volcanism, ground water discharge and diffusive leakage. At the same time, helium is lost to space by thermal and non-thermal escape (Kockarts, 1973; Oliver et al., 1984; Sano et al., 2013; Torgersen, 1989; Pierson-Wickmann et al., 2001). Based on these natural fluxes and the total atmospheric burden, the atmospheric residence time of ^{4}He is estimated to be $\sim$1 million years.

Table 3.1: Processes contributing to variations in the tropospheric and stratospheric $^4He/N_2$ ratio.

Process	^{4}He **flux (10^7 mol y^{-1})**	**Tropospheric $\delta(^4He/N_2)$ trend (per meg y^{-1})**	**Stratospheric $\delta(^4He/N_2)$ trend[1] (per meg y^{-1})**	**Tropospheric $\delta(^4He/N_2)$ anomaly (per meg)**	**Reference[2]**
Long-term trend					
(1) Crustal degassing and volcanism	24.0–50.7	0.26–0.55			(a)
(2) Loss to space	53.3–106.8	-0.58—1.15			(a,b)
(3) Non-terrestrial sources	insignificant				(a)
(4) Global Ocean warming[3]	1.3	-0.16			
(5) Fossil fuel extraction[4]	3189–12755	34–138			(c)
	13000±7000	140±76			(d)
	34000	367			(e)
(6) BDC acceleration[5]		0.5	-15		
Observational limits on decadal trends[6]					
		-1.4±44.5			(f)
		9.5±32.7			(g)
		-2±23.8			(h)
Seasonal and interannual variability					
Seasonal cycle of global ocean heat[7]				3–9	
Strat. circ. & STE variability[8]		±6	±375		
Interhemispheric difference[9]			<30		

[1] ($^4He/N_2$) trends are calculated using first column and assuming total atmospheric ^{4}He = 9.268 e+14 mol. N_2 changes are generally neglected except for ocean degassing. Tropospheric trends are globally uniform because the troposphere is well mixed. Stratospheric trend estimates are given for 35 km in the mid latitude Northern Hemisphere.

[1] ($^4He/N_2$) trends are calculated using first column and assuming total atmospheric ^{4}He = 9.268 e+14 mol. N_2 changes are generally neglected except for ocean degassing. Tropospheric trends are globally uniform because the troposphere is well mixed. Stratospheric trend estimates are given for 35 km in the mid latitude Northern Hemisphere.

[2]

(a) Torgersen (1989) (d) Pierson-Wickmann et al. (2001) (g) Mabry et al. (2015)

(b) Kockarts (1973) (e) Sano et al. (2013) (h) Boucher et al. (2018c)

(c) Oliver et al. (1984) (f) Lupton and Evans (2013)

[3] calculated from ^{4}He and N_2 solubility changes (Weiss, 1971; Hamme and Emerson, 2004) for an ocean heat content trend of 10 ZJ y^{-1} at a mean water temperature of 10°C.

[4] (c) includes natural gas, coal and uranium, (d) and (e) include natural gas, petroleum and coal.

[5] ($^4He/N_2$) rescaled from (Ar/N_2) assuming 7.5× greater gravitational separation. The secular (Ar/N_2) trend was simulated in the SOCRATES model for an accelerating BDC scenario (+4% dec^{-1}) by Ishidoya et al. (2020).($^4He/N_2$) trend is adjusted to reflect a more plausible BDC acceleration of +2% dec^{-1}.

[6] observed $^3He/^4He$ trends are translated to ^{4}He trends assuming $^3He/^4He$ = 3e-8 in fossil fuel associated helium.

[7] scaled from seasonal (Ar/N_2) changes of 5–15 per meg (Keeling et al., 2004) using solubility-temperature dependency of He, N_2 and Ar in a 10°C warm surface ocean (Weiss, 1971; Hamme and Emerson, 2004).

[8] Tropospheric and stratospheric($^4He/N_2$) rescaled from (Ar/N_2). Ishidoya et al. (2020) report a ±0.4 and ±25 per meg (Ar/N_2) change in troposphere and stratosphere in the SOCRATES model for a sinusoidal ±5% change in BDC strength over 3 years.

[9] Assuming that industrial He release is confined to the Northern Hemisphere and assuming an annual($^4He/N_2$) increase of 30 per meg (consistent with the current observational error) yields an interhemispheric($^4He/N_2$) difference < 30 per meg. Differences in STE of He between the hemispheres are neglected here but could be important.

Over the few last centuries, He release from fossil-fuel extraction has dwarfed the natural release rates of ^{4}He by several orders of magnitude. Based on knowledge of fossil fuel usage and He content of the material (Table 3.1) the additional ^{4}He release rate is estimated to be of order 3 to 30×10^{10} mole y^{-1} (e.g., Oliver et al., 1984; Sano et al., 1989, 2013; Pierson-Wickmann et al., 2001) implying that ^{3}He/^{4}He should be decreasing at rates between 35 and 350 per meg y^{-1}. However, in contrast to these predictions and some earlier observations (Oliver et al., 1984; Pierson-Wickmann et al., 2001; Sano et al., 1989, 2010), no significant trend in atmospheric ^{3}He/^{4}He has been observed using archived air samples spanning from the beginning of the 20$^{\text{th}}$ century to today at the level of roughly $\pm$30 per meg per year, suggesting similarly small increase rates in δ(He/N$_2$) (Boucher et al., 2018c; Lupton and Evans, 2013, 2004; Mabry et al., 2015). He release from fossil-fuel extraction is also expected to impose an interhemispheric gradient in δ(He/N$_2$). A rough upper bound can be estimated by assuming all fossil-fuel derived He emissions occur in the Northern Hemisphere and interhemispheric mixing of the atmosphere has a time scale of about one year. This would yield a north-south difference of 30 per meg, equal to the expected annual rise in δ(He/N$_2$). Seasonal and long-term ocean warming can cause small changes in He/N$_2$, mainly due to the impact on N2. From observations of δ(Ar/N$_2$) (Keeling et al., 2004) and solubility data of Ar, He and N$_2$ (Hamme and Emerson, 2004; Weiss, 1971), we estimate that the impact on He/N$_2$ of air-sea exchanges is on the order of 0.16 per meg y^{-1} for the secular ocean warming trend and 3-9 per meg for seasonal heat exchanges. Therefore, the ratio of stratospheric signals to ocean warming is $\sim$12 times greater for He/N$_2$ than Ar/N$_2$ and the effect of slow ocean warming is over two orders of magnitude smaller than the influence of fossil fuel exploitation. The He/N$_2$ ratio could also be impacted by processes changing atmospheric N$_2$. However, the annual removal of 7.5×10^{12} moles N$_2$ y^{-1} by anthropogenic nitrogen fixation in agriculture, combustion, and industry is clearly negligible compared to the $\sim1.4\times10^{20}$ moles of N$_2$ in the whole atmosphere (Fowler

et al., 2013). Volcanic emissions of N_2 are likewise negligible, order 10^9 moles y^{-1}.

3.3 Methods

Our He/N_2 analysis method relies on measuring the helium mole fraction relative difference between an air sample and a standard reference gas using a single collector for $^4He^+$ on a magnetic sector mass spectrometer (MS). Crucially, whole dry air is pressure-stabilized to a high level prior to gettering, so that the beam intensity ratio being measured is effectively the ^4He to air ratio. Measurements of the He mole fraction difference can also be expressed similarly to Eq. (3.1) as $\delta(^4He/M)$ where M is total moles. By applying small corrections for variations in O_2/N_2, Ar/N_2, and CO_2, the quantity $\delta(^4He/M)$ is easily related to $\delta(^4He/N_2)$. The MS is interfaced to a custom inlet system with on-line gettering and active flow stabilization using an actively pressure-controlled open split (Henneberg et al., 1975), as shown in Figure 3.2.

3.3.1 The Inlet system

The design of the inlet system incorporates elements of an open split (Henneberg et al., 1975) but further stabilizes the pressure using active control elements and allows active switching between a sample (SA) and reference standard gas stream (ST). Pneumatically-actuated pistons (Fig. 3.2c) alternately slide 0.3-mm tubes exhausting sample or standard gas close to a shared intake capillary which is placed at the end of the stabilization chamber (Fig. 3.2d) and connects the chamber to the getter oven and MS. The chamber is shaped as a funnel to guide the sliding tubing into a reproducible resting position. Variations in chamber pressure are measured with a 0.2-Torr MKS 223B differential pressure gauge and are limited to better than 1 part in 10^6 by opening an MKS Type 248 Control Valve, which allows most of the gas in the stabilization chamber to be pumped away by a vacuum pump. The valve is

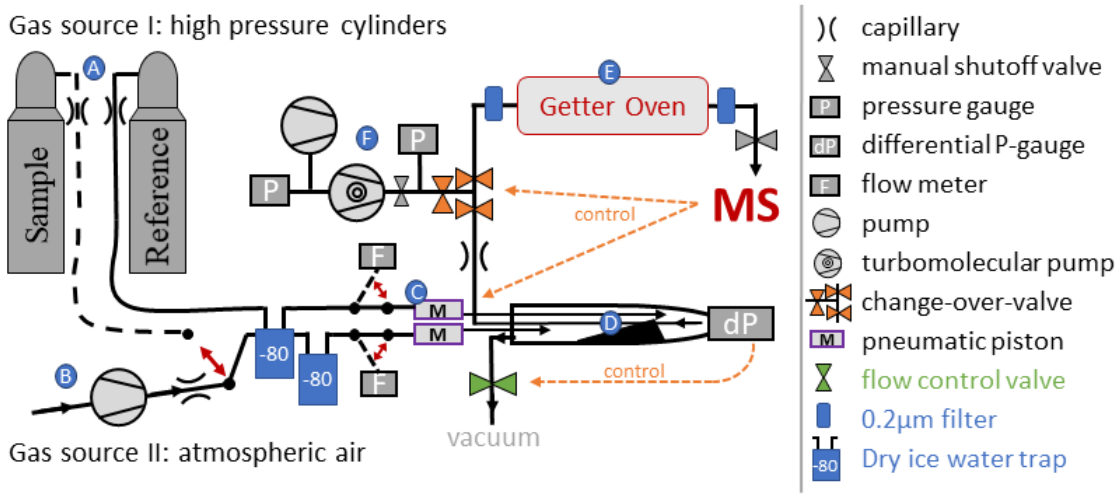

Figure 3.2: Schematic depiction of the flow-stabilizing MS inlet system. Dashed orange arrows highlight important control pathways and letters A–F in blue circles label the main sections of the inlet system. Red double arrows indicate manual switching option in the inlet system. Gas can either be delivered from samples in high-pressure cylinders (A) or locally pumped ambient air (B). The flow can be measured by two Omron flow meters before entry into the pressure stabilization chamber (C). Pistons (D) alternately move fine metal tubing in the pressure stabilization chamber, pushing either the sample or standard gas stream deeper into the stabilization chamber where the gas will be picked up by a single capillary leading to the MS. The chamber is exhausted to a vacuum system and the pressure is monitored and controlled by a differential pressure gauge combined with an automatic MKS flow control valve. The stainless-steel getter oven (E) has an inner diameter of 1/2" and is filled with 10–12 g of titanium sponge. 2µm-filters prevent particles from contaminating the MS and gas delivery system. In case of an anomalous pressure change in the MS or when venting the getter oven, the getter oven can be isolated from the pressure-stabilization chamber with a change-over-valve controlled directly by the MS software. The entire inlet vacuum system is backed by a diaphragm vacuum pump and a turbomolecular pump (F). A manual shutoff-valve can isolate the getter oven from the MS.

controlled via an MKS 250E Control Module. The 0.3 mm tubes enter the chamber through sliding seals lubricated with vacuum grease, thus allowing the chamber to be operated at a selected pressure above or below ambient. The default setting is

14 psia (96.5 kPa). The shared outlet capillary is crimped and thermally insulated. The pressure in the getter oven (Fig. 3.2e) is about 2 mTorr (0.3 Pa) because the getter material effectively acts as a vacuum pump.

3.3.2 Continuous-flow gettering

In the getter chamber (Fig. 3.2e), high purity titanium sponge (Ti) irreversibly reacts with N_2, O_2, CO_2, and other non-noble gases in air to form titanium nitride (TiN), titanium dioxide (TiO_2), titanium carbide (TiC) and other compounds at ∼850°C. This increases the concentration of He in the gas mixture by a factor of about 100, boosting precision. The getter oven is manufactured from heat resistant stainless steel (SS310) and equipped with VCR face seals for easy maintenance. The temperature of the getter oven is determined by manually adjusting the power provided to the furnace surrounding the getter. The furnace is additionally equipped with an independent limit controller for safety.

The gettering efficiency depends on the furnace's temperature and must be balanced against material tolerance and increased evolution of H_2 gas from the metal in the getter. H_2 forms a solid solution in Ti and is continuously released to the gas stream when Ti is heated. The solution process is reversible and H_2 is absorbed if the Ti is cooled down. H_2 could interact with He^+ in the source or combine with ionized gas to form hydride compounds such as ArH^+ (Fig. 3.3) However, since the H_2 flux into the gas stream varies slowly compared to the 30-second switching timescale, the impact of H^+ cancels during sample-standard comparison. In its current size (∼10–12 g Ti), the getter can be used for 70–80h before the Ti must be replaced. This requires breaking vacuum in the inlet approximately once every four weeks depending on usage. After replacement, fresh titanium is gradually heated to 900°C over ∼12h in isolation from the MS to allow degassing without contaminating the MS. A coarse mesh of metal wire and 2 µm SWAGELOK filters on both sides of

the getter prevent getter-derived dust from entering the vacuum system and MS.

3.3.3 Inlet operation

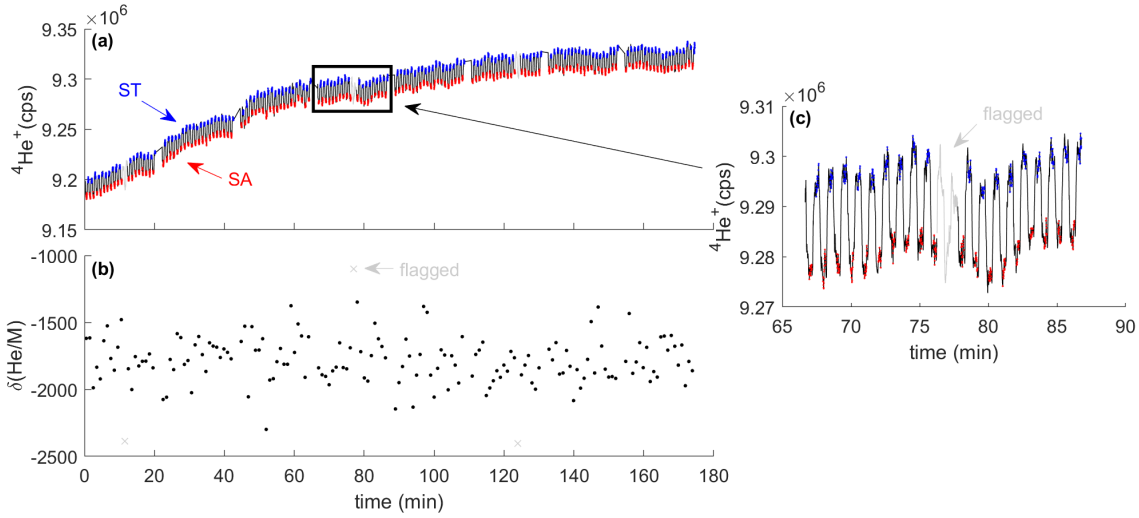

Figure 3.3: Typical analysis results from the measurement of two high pressure cylinders. The MS monitors the $^4He^+$-ion beam during switching between sample (SA) and standard (ST) gas (a). Red and blue shaded data points highlight the periods used for integration and calculation of the delta value (b). They are separated by idle times (black lines) to allow complete flushout after switching. Data are quality controlled and flagged periods are shown in grey. Inset (c) shows one block of 20 sample-standard comparisons including one cycled that was flagged as an outlier.

We have developed customized scripts using the software ISODAT provided with any MAT253 mass spectrometer to control the inlet system and operate the pneumatic actuators for He/M analysis (Fig. 3.3). In a typical run, the instrument performs sample-standard gas switching with a ∼30 second switching time (∼60 sec full cycle), using a conservative 18-second idle time to ensure complete flush-out of the stabilization chamber and the getter oven. As customary in dynamic MS noble gas application, we group each analysis into blocks consisting of (i) adjusting the accelerating voltage to find the center of the ^4He peak followed by (ii) 20 sample-

standard comparisons. Background concentrations of ^{4}He in the MS are determined daily and subtracted. Data are quality controlled and anomalous cycles are rejected when delta values deviate by more than 3 standard deviations from the smoothed time series or when there are abrupt changes detected in the ion beam associated with instability in the MS source (not shown). ISODAT also monitors the MS source pressure and closes the external change-over-valve (Fig. 3.2) to protect the MS in case of a pressure control failure.

3.3.4 Gas handling and sample delivery systems

Air can be delivered to the inlet system from either a pair of high-pressure gas cylinders (Fig. 3.2a) or from a continuous-flow system (Fig. 3.2b) pumping locally-sampled ambient air directly to the laboratory. For He/N_2 reference material, we rely on compressed dry air stored in high pressure cylinders, as is conventional for atmospheric measurements of O_2/N_2, CO_2, and Ar/N_2 (Keeling et al., 2007). All cylinders are stored horizontally for 2 days in a thermal enclosure before analysis to minimize the risk of thermal fractionation. The pressure is dropped to slightly above ambient directly at the head valve of high-pressure cylinders using capillaries rather than regulators. The use of capillaries ensures that all wetted parts are exclusively metal, which is impermeable to He, and eliminates problems we encountered using regulators during initial tests. Due to the use of capillaries, the gas delivery system cannot be evacuated efficiently and instead must be purged for several hours ahead of analysis until the signal stabilizes. The flow rates in the lines are monitored using 0.1 liter per minute Omron DF6-P flow meters and are manually balanced at around 27–28 cm^3 min^{-1} before every analysis by adjusting the crimping of the capillaries. Sample and standard gas streams each flow through a -80°C cold trap made from 1/4" stainless steel tubing before entering the pressure stabilization chamber (Fig. 3.2d).

3.4 Results

3.4.1 Gettering performance

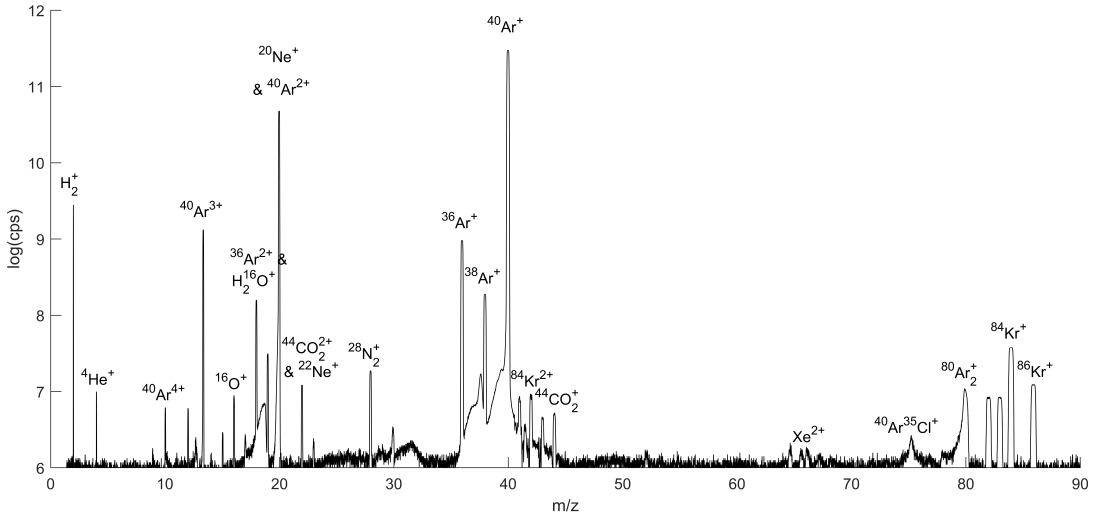

Figure 3.4: Mass scan of ambient air. Ion beam intensity is shown as the logarithm of the ions counted per second, and select ion species are labeled.

A mass scan of medical air introduced through the gettering and flow-stabilizing inlet system revealed that N_2 and O_2 are almost completely removed from the air by the on-line getter (Fig. 3.4). ^{40}Ar ions with one or more charges yield the largest beams in the scan followed by ^{36}Ar, and H_2 evolving from the hot metal in the getter oven.

3.4.2 Response time

Our setup demonstrates the ability to transition between sample and standard gas with a e-folding time scale of ∼4 seconds (Fig. 3.5). The e-folding time is primarily controlled by the volume of the getter and the total flow of gas through the getter.

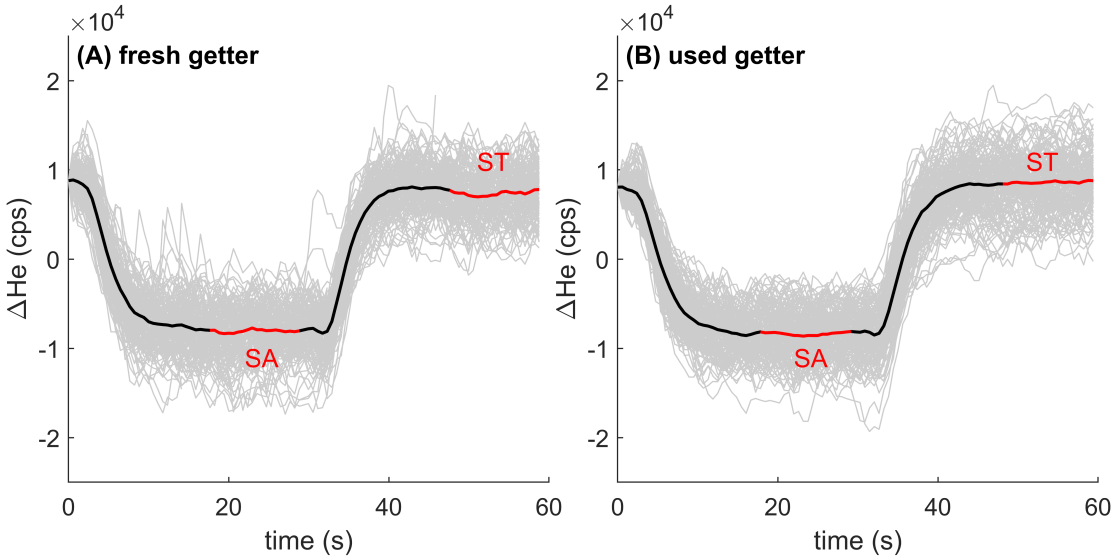

Figure 3.5: Stack of ^{4}He ion count difference (10^4 counts per second, cps) when switching between the same standard (ST) and sample (SA) gas stream using fresh titanium sponge (A) and nearly depleted getter material (B). Grey lines show individual records forced to align at time equals zero, and the thick black line shows the average of all stacked switching events. The analysis cycle consists of (i) switching to SA with an idle time of 18 seconds, (ii) a 12 second integration of ions from SA, (iii) switching back to ST, again with a 18 second idle time, and finally (iiii) a 12 second integration of ST.

Regions of the inlet system upstream of the getter experience ∼100× faster flushing than downstream of the getter because the gas upstream still contains N_2 and O_2 and hence flows much faster. The e-folding time does not change substantially over the life span of the getter.

3.4.3 Analytical precision

Using the default 60 sec sample-standard cycle, the gettering and flow-stabilizing inlet system achieves an internal precision in δ(He/M) of approximately ±15 per meg over 1.5h and ±8 per meg (1σ) for samples run 6h or longer (Figs. 3.6&3.7). The

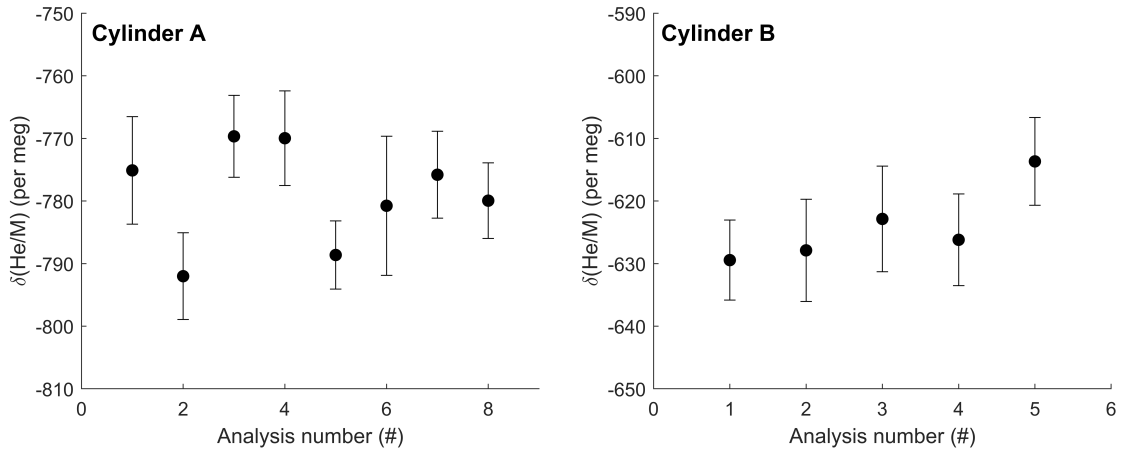

Figure 3.6: Repeat δ(He/M) analysis of two high-pressure cylinders against ambient La Jolla air collected in 2019. Each data point shown is the average of at least 300 individual 12-sec measurements. Repeat analysis show a standard deviation of 8.1 and 6.3 per meg for cylinder A and cylinder B respectively. Analysis 6 for cylinder A was shorter resulting in a larger uncertainty for that measurement. Data are not corrected for zero enrichment effects discussed in the text.

reproducibility of repeated 6–8h measurements of the same sample and standard gas cylinder combination is comparable and essentially as expected from the shot-noise on the ^{4}He ion current.

The zero enrichment, i.e., the delta value observed when introducing the same gas through sample and standard side of the inlet, is generally small and stable over time. It is tested by mounting the crimped delivery capillaries (Fig. 3.2a) to a tee fitting, which splits the gas stream at high pressure from a single tank of air. This tee minimizes thermal fractionation by dividing the flow at a junction machined into the center of a large brass block (Keeling, 1988). Identical delta values (within error) obtained after reversing the outlet from the tee demonstrate that no measurable fractionation occurs within the tee and therefore that the zero enrichment reflects a persistent asymmetry somewhere downstream, most likely within the open split. The typical zero enrichment varies slightly with the mean flow of gas into the stabilization

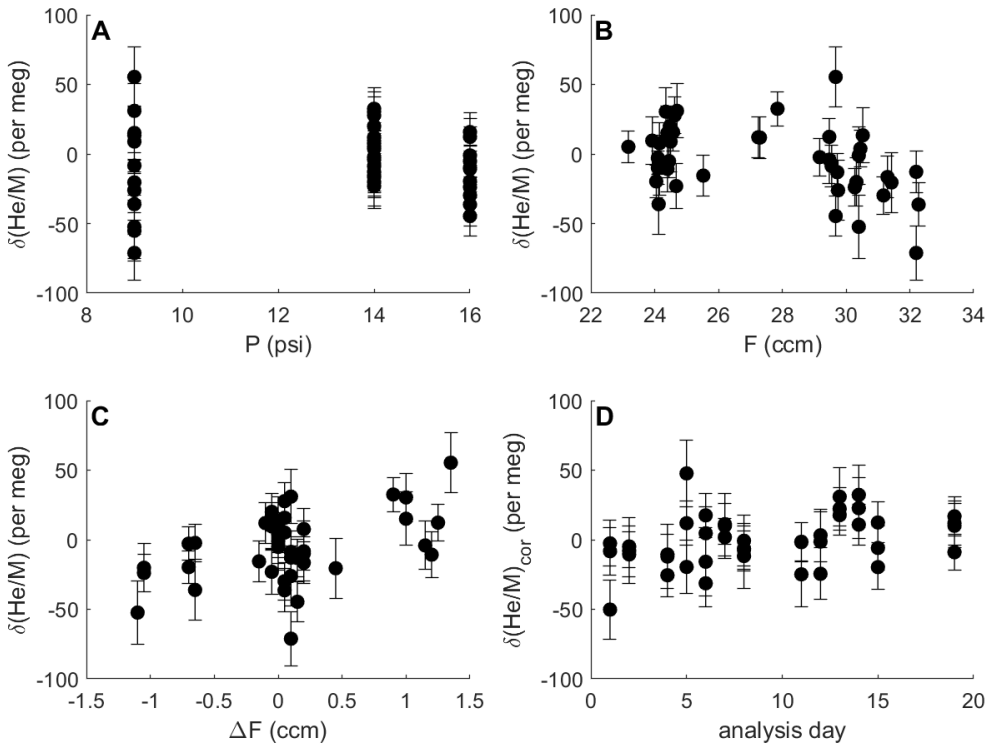

Figure 3.7: Difference in δ(He/M) between two identical gas streams (i.e., the zero enrichment) measured repeatedly under different conditions over 1.5–3h. Error bars show 1σ uncertainty. Measurements were made at different pressure levels (a), with slightly varying gas flows to the stabilization chamber (b), and imbalances in flow between SA and ST side (c). The same shared capillary was used for all analysis. Therefore, the pressure in the stabilization chamber controls the intensity of the ion beam and the internal precision of the analysis, illustrated by the greater scatter of observations at 9 psi (62.1 kPa). Delta values shown in (d) were corrected for the influence of pressure, mean flow, and flow imbalance according to coefficients found by multiple linear regression (see text). For a pressure of 14 psi (96.5 kPa), corrected delta values generally show scatter as expected from shot-noise behavior and corrected delta values are stable over time.

chamber (F), the pressure in the chamber (P), and the flow offset between SA and ST side (ΔF) before entering the stabilization chamber (Fig. 3.7). Weighted multiple linear regression analysis using 3 different pressure levels (9 psi, 14 psi, and 16 psi,

i.e, 62.1, 96.5, and 110.3 kPa) reveals that the zero enrichment value decreases by 2.8±0.9 per meg per 1 cm^3 min^{-1} change in mean flow away from 27.5 cm^3 min^{-1} and increases by 17.2±4.8 per meg per 1 cm^3 min^{-1} flow imbalance between SA and ST. The dependence of δ(He/M) on F and ΔF is significant at the 5% level. For a balanced flow of 27.5 cm^3 min^{-1} at 62.1, 96.5 and 110.3 kPa pressure in the stabilization chamber, the mean zero enrichment is -9.61±7.2 per meg, 1±3.7 per meg and -15.7±4.7 per meg, respectively. P is held constant for measurements at 96.5 kPa. F and ΔF are stable over 8h to within ±0.2 cm^3 min^{-1}. This typically yields a correction for mean gas flow and flow imbalance of less than 10 per meg with an uncertainty smaller than 6 per meg, which increases the overall analytical uncertainty in repeat tank analysis from 8 to 10 per meg.

3.5 Discussion

The gettering and flow-stabilizing inlet system has demonstrated the ability to determine the helium mole fraction difference between a sample and standard gas, δ(He/M), to about 10 per meg in a single 6–8h analysis. δ(He/M) can be related to $\delta(\mathrm{He/N_2})$ using

$$\delta(He/N_2) \approx \delta(He/M) + \delta(O_2/N_2)X_{O_2} + \delta(Ar/N_2)X_{Ar} + dX_{CO_2} \qquad (3.3)$$

as derived in Box 1, using independent measurements of $\delta(\mathrm{O_2/N_2})$, $\delta(\mathrm{Ar/N_2})$, and $\mathrm{dX_{CO2}}$ (Keeling et al., 2004, 1998). These corrections are relatively small and therefore do not significantly contribute to the overall uncertainty of $\delta(\mathrm{He/N_2})$. The long-term atmospheric changes in $\delta(\mathrm{O_2/N_2})$ ∼ -19 per meg y^{-1} and $\mathrm{dX_{CO2}}$ ∼2.5 ppm y^{-1} yield corrections of approximately -4 per meg y^{-1} and +2.5 per meg y^{-1}, respectively. The seasonal variations in $\delta(\mathrm{O_2/N_2})\mathrm{X_{O2}}$ and $\mathrm{dX_{CO2}}$ partly cancel, yielding net seasonal corrections of ∼10 per meg in both hemispheres. The term $\delta(\mathrm{Ar/N_2})\mathrm{X_{Ar}}$ contributes variations less than 1 per meg on all time scales.

Box 3.1| Deriving the helium-to-nitrogen ratio from δ(He/M)

A relationship between $\delta(\mathrm{He/N_2})$ and $\delta(\mathrm{He/M})$ can be derived from:

$$\begin{aligned}\delta(He/N_2) &= \frac{dHe}{He} - \frac{dN_2}{N_2} = \frac{dHe}{He} - \frac{dM}{M} - \frac{dN_2}{N_2} + \frac{dM}{M} \\ &= \delta(He/M) - \frac{dN_2}{N_2} + \frac{dN_2 + dO_2 + dAr + dCO_2}{M}\end{aligned}$$

Using $\frac{dN_2}{M} = \frac{dN_2}{N_2} X_{N_2}$, $\frac{dO_2}{M} = \frac{dO_2}{O_2} X_{O_2}$, etc, where X_i is the mole fraction of gas i, yields

$$\begin{aligned}\delta(He/N_2) =& \delta(He/M) + \frac{dN_2}{N_2}\left[-1 + X_{N_2} + X_{O_2} + X_{Ar} + X_{CO_2} + X_{H_2O} \cdots\right] \\ &+ \left[\frac{dO_2}{O_2} - \frac{dN_2}{N_2}\right] X_{O_2} + \left[\frac{dAr}{Ar} - \frac{dN_2}{N_2}\right] X_{Ar} \\ &+ \left[\frac{dCO_2}{CO_2} d) - \frac{dN_2}{N_2}\right] X_{CO_2} + \cdots\end{aligned}$$

This can be simplified to Eq. (3.3) using $\left[\frac{dCO_2}{CO_2} - \frac{dN_2}{N_2}\right] X_{CO_2} = dX_{CO_2}$, which follows because relative changes in CO_2 are much larger than relative changes in N_2.

3.5.1 Potential applications

The presented $\mathrm{He/N_2}$ measurement capability has a range of possible applications. Our primary targets are (i) to use stratospheric $\delta(\mathrm{He/N_2})$ as a tracer of the large-scale stratospheric circulation and (ii) to evaluate tropospheric $\delta(\mathrm{He/N_2})$ trends as a possible indicator of anthropogenic fossil fuel exploitation. We expect an excellent signal-to-noise ratio for the detection of stratospheric changes in $\delta(\mathrm{He/N_2})$. Inter-annual variability in stratospheric $\delta(\mathrm{He/N_2})$ is likely on the order 300–400 per meg (Table 3.1). Repeat 6–8h measurements of a high-pressure tank currently achieve a precision of $\sim$10 per meg, or about 40 times better than the stratospheric signal. Associated changes in tropospheric $\delta(\mathrm{He/N_2})$, in contrast, are likely much smaller at around 6 per meg and therefore at or below the current limit of detection even after

averaging of multiple samples. The reproducibility of measurements also depends on adequate calibration strategies. The short-term reproducibility of high-pressure cylinders shown in Figure 3.6 and the long-term stability established for O_2/N_2, Ar/N_2, and Ar/N_2 standard gases in previous work (Keeling et al., 2007) suggest that long-term stability in $\delta(He/N_2)$ is achievable but needs further evaluation.

He/N_2 measurements can help quantify the anthropogenic ^4He release over time due to fossil fuel extraction (Boucher et al., 2018c; Lupton and Evans, 2013, 2004; Mabry et al., 2015; Oliver et al., 1984; Sano et al., 2010, 1989). Although theoretical predictions clearly support an anthropogenic ^4He increase, past observational studies produced conflicting evidence. Recent improvements in analytical methods and sampling have narrowed the uncertainty in $^3He/^4He$ trend estimates to <30 per meg y^{-1} with a mean statistically indistinguishable from zero (Table 3.1). However, with a precision of ∼10 per meg on single samples, measurements of $\delta(^4He/N_2)$ on decades-old archived air may allow trend detection to ∼1 per meg y^{-1} or better, while also avoiding possible complications from ^3He emissions.

Another possible application is the investigation of spatial gradients in atmospheric $\delta(He/N_2)$ caused by the distribution of local volcanic or anthropogenic sources (e.g. Sano et al., 2010; Boucher et al., 2018a). High precision $\delta(He/N_2)$ may allow the detection of diffuse helium release in regions of volcanic activity (Boucher et al., 2018b). Furthermore, global north-south $\delta(He/N_2)$ gradients from anthropogenic emission sources concentrated in the Northern Hemisphere are likely on the order of 10s of per meg and thus may also be detectable directly. Alternatively, studies could target more local gradients around oil or natural gas facilities that are likely even greater.

Table 3.2: Summary of observed ion beams in Figure 4. Relative ion beam intensities on MAT253 are calculated from the scan with identical source tuning. Xe isotope beams were not observed but scaled from previous observations in the lab.

m/z	**Dominant ions**	**Ion beam intensity (cps)***	**ion beam intensity relative to $^4He^+$**
4	$^4He^+$	9.70E+06	1
20	$^{20}Ne^+$, $^{40}Ar^{2+}$	4.78E+10	4916.1
22	$^{22}Ne^+$,$^{44}CO_2^{2+}$	1.22E+07	1.25
36	$^{36}Ar^+$	9.55E+08	98.26
38	$^{38}Ar^+$	1.89E+08	19.44
40	$^{40}Ar^+$	2.98E+11	30660
82	$^{82}Kr^+$	8.50E+06	0.87
83	$^{83}Kr^+$	8.40E+06	0.86
84	$^{84}Kr^+$	3.76E+07	3.87
86	$^{86}Kr^+$	1.22E+07	1.25
129*	$^{129}Xe^+$	2.60E+06	0.27
131*	$^{131}Xe^+$	2.10E+06	0.22
132*	$^{132}Xe^+$	2.70E+06	0.28
136*	$^{136}Xe^+$	9.00E+05	0.09

*Xe isotopes were not measured directly here because of the limited dynamic range of the MAT 253 when set to measure He. Instead we report expected Xe ion beam intensities scaled from previously analysis of Kr and Xe in the lab assuming natural isotopic abundances.

The method developed here is potentially applicable to measure the abundance of any noble gas in air. The intensity of the ion beam and thus the precision for different noble gases depends on their natural abundance and ionization efficiency in the MS source. ^{20}Ne and ^{22}Ne have isobaric interferences from doubly charged Ar and Ar/N_2, but Kr and Xe yield usable ion beams (Table 3.2). We estimate a precision of ∼5 and ∼19 per meg for repeat 6–8h analyses of $\delta(^{84}Kr/^{28}N_2)$ and $\delta(^{129}Xe/^{28}N_2)$ respectively, by assuming that precision scales with the square root of the total ions counted as expected from shot-noise behavior. This estimate compares favorably to the precision currently reported in conventional dual inlet mass spectrometry

studies (Baggenstos et al., 2019; Bereiter et al., 2018). For example, Baggenstos et al. (2019) achieved a precision of 88 per meg and 203 per meg for repeat ∼2h analyses of $\delta(^{84}\mathrm{Kr}/^{40}\mathrm{Ar})$ and $\delta(^{132}\mathrm{Xe}/^{40}\mathrm{Ar})$ in ambient air, respectively.

The improved precision enabled by our inlet system should be sufficient to resolve the previously unobserved annual cycle of Kr and Xe caused by the seasonal release and uptake of both gases by the ocean as it warms and cools. The seasonal cycle of $\delta(^{40}\mathrm{Ar}/^{28}\mathrm{N_2})$ has an amplitude of 5–15 per meg in the extratropics (Keeling et al., 2004). $\delta(^{84}\mathrm{Kr}/^{28}\mathrm{N_2})$ and $\delta(^{132}\mathrm{Xe}/^{28}\mathrm{N_2})$ however are ∼3.4 and ∼8.9 times more sensitive than $\delta(^{40}\mathrm{Ar}/^{28}\mathrm{N_2})$ to changes in ocean temperature owing to the different temperature-dependences of Ar, Kr and Xe solubility in seawater (Hamme and Emerson, 2004; Jenkins et al., 2019). This implies that seasonal variations in $\delta(^{84}\mathrm{Kr}/^{28}\mathrm{N_2})$ and $\delta(^{132}\mathrm{Xe}/^{28}\mathrm{N_2})$ have a magnitude of 17–51 and 45–134 per meg respectively, which would be readily resolved if precision of our system scales as expected with signal strength.

The gettering inlet and MS system was applied here only for single ion ($\mathrm{He^+}$) detection, but alternately could be applied for multi-ion collection. The acquisition of Kr and Xe isotope ratios for example would provide valuable additional information for detecting artifactual fractionation during sampling and allow further improvements in precision by increasing the total number of ions collected.

The need for only a single ion detector also allows the gettering and flow-stabilizing inlet to be interfaced with simpler and more affordable mass spectrometers, such as quadrupole systems. The performance of the system will depend on the stability of the $^4\mathrm{He^+}$-ion beam over the time scale of switching and will need to be evaluated critically, but any variability on time scales longer than the switching time is canceled by sample-standard differencing.

3.6 Conclusions

Here, we present a new method for high-precision measurements of changes in the He/N_2 ratio of atmospheric air. The method relies on monitoring of the $^4He^+$ ion beam in a mass spectrometer during sample-standard switching. The ion beam is stabilized by flowing sample and standard air through a single capillary into the MS from an actively pressure-controlled open-split (Henneberg et al., 1975), such that variability of the $^4He^+$ ion beam directly reflects differences in the helium mole fraction of the gas mixtures. Measurements of the helium mole fraction can easily be converted to $\delta(He/N_2)$ after the analysis if O_2/N_2, Ar/N_2, and Ar/N_2 concentrations of the sample are determined as well. An online getter preconcentrates He and other noble gases before entry into the MS by chemically removing >99.99% of all N_2 and O_2 in a reaction with titanium sponge. Our method thereby avoids the need for peak jumping and avoids the need for a multi-collector mass spectrometer, while achieving a precision of ∼10 per meg (1σ) on repeat analysis of $\delta(He/N_2)$ in high pressure tanks.

In future work, the gettering and flow-stabilizing inlet system could be used to investigate possible interannual to decadal changes in stratospheric $\delta(He/N_2)$ linked to variability in stratospheric circulation and stratosphere-troposphere exchange processes. Additional applications could include the search for a signal of anthropogenic helium release during fossil fuel extraction and burning (Boucher et al., 2018c; Lupton and Evans, 2004, 2013; Mabry et al., 2015; Oliver et al., 1984; Pierson-Wickmann et al., 2001; Sano et al., 1989), or measurements of spatial gradients resulting from localized human or natural sources of helium (Boucher et al., 2018a,b; Sano et al., 2010). The setup is also suitable for the analysis of other noble gases and could therefore be used to study seasonal ocean warming associated with degassing or uptake of Kr and Xe from the ocean (Baggenstos et al., 2019; Bereiter et al., 2018).

3.7 Supplement availability

The supplement related to this article is available online at: https://amt.copernicus.org/preprints/amt-2020-313/amt-2020-313-supplement.

3.8 Acknowledgements

We thank Ross Beaudette, Alan Seltzer, Sarah Shackleton, Jacob Morgan, Jessica Ng, and Eric Morgan for laboratory support and insightful discussions during the development of the He/N_2 analysis system. We are grateful to Shane Clark, Savannah Hatley, Adam Cox, and Timothy Lueker for providing high-pressure cylinders used during testing. We also thank them for maintaining and operating the Ar/N_2, O_2/N_2 and Ar/N_2 analysis systems in the Keeling laboratory. This work was supported by the National Science Foundation grants MRI-1920369 and AGS-1940361.

Chapter 3, in full, has been submitted for publication of the material as it may appear in Birner, B., Paplawsky, W., Severinghaus, J., Keeling, R.F., 2020. Measurements of atmospheric He/N_2 as an indicator of fossil fuel extraction and stratospheric circulation. Atmospheric Measurement Techniques Discussions 1–25. https://doi.org/10.5194/amt-2020-313. The dissertation author was the primary investigator and author of this paper.

References

Arblaster, J., Gillett, N., Calvo, N., Forster, P. M., Polvani, L., Son, S.-W., Waugh, D., and Young, P.: Stratospheric ozone changes and climate, Chapter 4, Tech. rep., World Meteorological Organization, Geneva, Switzerland, 2014.

Baggenstos, D., Häberli, M., Schmitt, J., Shackleton, S. A., Birner, B., Severinghaus, J. P., Kellerhals, T., and Fischer, H.: Earth's radiative imbalance from the Last

Glacial Maximum to the present, Proceedings of the National Academy of Sciences of the United States of America, 116, 14 881–14 886, doi:10.1073/pnas.1905447116, 2019.

Belikov, D., Sugawara, S., Ishidoya, S., Hasebe, F., Maksyutov, S., Aoki, S., Morimoto, S., and Nakazawa, T.: Three-dimensional simulation of stratospheric gravitational separation using the NIES global atmospheric tracer transport model, Atmospheric Chemistry and Physics, 19, 5349–5361, doi:10.5194/acp-19-5349-2019, 2019.

Bereiter, B., Shackleton, S., Baggenstos, D., Kawamura, K., and Severinghaus, J.: Mean global ocean temperatures during the last glacial transition, Nature, 553, 39–44, doi:10.1038/nature25152, 2018.

Birner, B., Chipperfield, M. P., Morgan, E. J., Stephens, B. B., Linz, M., Feng, W., Wilson, C., Bent, J. D., Wofsy, S. C., Severinghaus, J., and Ralph, F.: Gravitational separation of Ar/N2 and age of air in the lowermost stratosphere in airborne observations and a chemical transport model, Atmospheric Chemistry and Physics Discussions, pp. 1–34, doi:10.5194/acp-2020-95, 2020.

Bönisch, H., Engel, A., Curtius, J., Birner, T., and Hoor, P.: Quantifying transport into the lowermost stratosphere using simultaneous in-situ measurements of SF6 and CO2, Atmospheric Chemistry and Physics, 9, 5905–5919, doi:10.5194/acp-9-5905-2009, 2009.

Boucher, C., Lan, T., Mabry, J., Bekaert, D. V., Burnard, P. G., and Marty, B.: Spatial analysis of the atmospheric helium isotopic composition: Geochemical and environmental implications, Geochimica et Cosmochimica Acta, 237, 120–130, doi:10.1016/j.gca.2018.06.010, 2018a.

Boucher, C., Lan, T., Marty, B., Burnard, P. G., Fischer, T. P., Ayalew,

D., Mabry, J., Maarten de Moor, J., Zelenski, M. E., and Zimmermann, L.: Atmospheric helium isotope composition as a tracer of volcanic emissions: A case study of Erta Ale volcano, Ethiopia, Chemical Geology, 480, 3–11, doi:10.1016/j.chemgeo.2017.05.011, 2018b.

Boucher, C., Marty, B., Zimmermann, L., and Langenfelds, R.: Atmospheric helium isotopic ratio from 1910 to 2016 recorded in stainless steel containers, Geochemical Perspectives Letters, 6, 23–27, doi:10.7185/geochemlet.1804, 2018c.

Brewer, A. W.: Evidence for a world circulation provided by the measurements of helium and water vapour distribution in the stratosphere, Quarterly Journal of the Royal Meteorological Society, 75, 351–363, doi:10.1002/qj.49707532603, 1949.

Butchart, N.: The Brewer-Dobson circulation, Reviews of Geophysics, 52, 157–184, doi:10.1002/2013RG000448, 2014.

Dobson, G. M. B.: Origin and distribution of the polyatomic molecules in the atmosphere, Proceedings of the Royal Society of London. Series A. Mathematical and Physical Sciences, 236, 187–193, doi:10.1098/rspa.1956.0127, 1956.

Engel, A., Möbius, T., Bönisch, H., Schmidt, U., Heinz, R., Levin, I., Atlas, E., Aoki, S., Nakazawa, T., Sugawara, S., Moore, F., Hurst, D., Elkins, J., Schauffler, S., Andrews, A., and Boering, K.: Age of stratospheric air unchanged within uncertainties over the past 30 years, Nature Geoscience, 2, 28–31, doi:10.1038/ngeo388, 2009.

Engel, A., Bönisch, H., Ullrich, M., Sitals, R., Membrive, O., Danis, F., and Crevoisier, C.: Mean age of stratospheric air derived from AirCore observations, Atmospheric Chemistry and Physics, 17, 6825–6838, doi:10.5194/acp-17-6825-2017, 2017.

Flury, T., Wu, D. L., and Read, W. G.: Variability in the speed of the Brewer-Dobson circulation as observed by Aura/MLS, Atmospheric Chemistry and Physics, 13, 4563–4575, doi:10.5194/acp-13-4563-2013, 2013.

Glückauf, E.: A simple analysis of the helium content of air, Transactions of the Faraday Society, 44, 436–439, 1944.

Graven, H. D., Guilderson, T. P., and Keeling, R. F.: Observations of radiocarbon in CO2 at La Jolla, California, USA 1992-2007: Analysis of the long-term trend, Journal of Geophysical Research Atmospheres, 117, 1–14, doi:10.1029/2011JD016533, 2012.

Haenel, F. J., Stiller, G. P., Von Clarmann, T., Funke, B., Eckert, E., Glatthor, N., Grabowski, U., Kellmann, S., Kiefer, M., Linden, A., and Reddmann, T.: Reassessment of MIPAS age of air trends and variability, Atmospheric Chemistry and Physics, 15, 13 161–13 176, doi:10.5194/acp-15-13161-2015, 2015.

Hamilton, K. and Fan, S.-M.: Effects of the stratospheric quasi-biennial oscillation on long-lived greenhouse gases in the troposphere, Journal of Geophysical Research, 105, 20 581, doi:10.1029/2000JD900331, 2000.

Hamme, R. C. and Emerson, S. R.: The solubility of neon, nirogen and argon in distilled water and seawater, Deep-Sea Research I, 51, 1517–1528, 2004.

Hegglin, M. I. and Shepherd, T. G.: Large climate-induced changes in ultraviolet index and stratosphere-to- troposphere ozone flux, Nature Geoscience, 2, 687–691, doi:10.1038/ngeo604, 2009.

Henneberg, D., Heinrichs, U., and Schomburg, G.: Open Split Connection of Glass Capillary Columns to Mass Spectrometers, Chromatographia, 8, 449–451, 1975.

Holton, J. R., Haynes, P. H., Mcintyre, M. E., Douglass, A. R., and Rood, B.: Stratosphere-Troposphere, Review of Geophysics, pp. 403–439, 1995.

Ishidoya, S., Sugawara, S., Morimoto, S., Aoki, S., Nakazawa, T., Honda, H., and Murayama, S.: Gravitational separation in the stratosphere - A new indicator of atmospheric circulation, Atmospheric Chemistry and Physics, 13, 8787–8796, doi:10.5194/acp-13-8787-2013, 2013.

Ishidoya, S., Sugawara, S., Inai, Y., Morimoto, S., Honda, H., Ikeda, C., Hashida, G., Machida, T., Tomikawa, Y., Toyoda, S., Goto, D., Aoki, S., and Nakazawa, T.: Gravitational separation of the stratospheric air over Syowa, Antarctica and its connection with meteorological fields, Atmospheric Science Letters, 19, 1–7, doi:10.1002/asl.857, 2018.

Ishidoya, S., Sugawara, S., Tohjima, Y., Goto, D., Ishijima, K., Niwa, Y., Aoki, N., and Murayama, S.: Secular change of the atmospheric Ar/N2 and its implications for ocean heat uptake and Brewer-Dobson circulation, Atmospheric Chemistry and Physics Discussions, doi:doi.org/10.5194/acp-2020-301, 2020.

Jenkins, W. J., Lott, D. E., and Cahill, K. L.: A determination of atmospheric helium, neon, argon, krypton, and xenon solubility concentrations in water and seawater, Marine Chemistry, 211, 94–107, doi:10.1016/j.marchem.2019.03.007, 2019.

Keeling, R. F., Manning, A. C., McEvoy, E. M., and Shertz, S. R.: Methods for measuring changes in atmospheric O2 concentration and their application in southern hemisphere air, Journal of Geophysical Research, 103, 3381–3397, doi:10.1029/97JD02537, 1998.

Keeling, R. F., Blaine, T., Paplawsky, B., Katz, L., Atwood, C., and Brockwell, T.: Measurement of changes in atmospheric Ar/N_2 ratio using a rapid-switching, single-capillary mass spectrometer system, Tellus, 56B, 322–338, doi:10.1111/j.1600-0889.2004.00117.x, 2004.

Keeling, R. F., Manning, A. C., Paplawsky, W. J., and Cox, A. C.: On the long-

term stability of reference gases for atmospheric O2/N2 and CO2 measurements, Tellus B: Chemical and Physical Meteorology, 59B, 3–14, doi:10.1111/j.1600-0889.2006.00196.x, 2007.

Kockarts, G.: Helium in the terrestrial atmosphere, Space Science Reviews, 14, 723–757, doi:10.1007/BF00224775, 1973.

Li, F., Waugh, D. W., Douglass, A. R., Newman, P. A., Pawson, S., Stolarski, R. S., Strahan, S. E., and Nielsen, J. E.: Seasonal variations of stratospheric age spectra in the Goddard Earth Observing System Chemistry Climate Model (GEOSCCM), Journal of Geophysical Research Atmospheres, 117, 1–14, doi:10.1029/2011JD016877, 2012.

Lupton, J. and Evans, L.: The atmospheric helium isotope ratio: Is it changing?, Geophysical Research Letters, 31, 1–4, doi:10.1029/2004GL020041, 2004.

Lupton, J. and Evans, L.: Changes in the atmospheric helium isotope ratio over the past 40 years, Geophysical Research Letters, 40, 6271–6275, doi:10.1002/2013GL057681, 2013.

Mabry, J. C., Lan, T., Boucher, C., Burnard, P. G., Brennwald, M. S., Langenfelds, R., and Marty, B.: No evidence for change of the atmospheric helium isotope composition since 1978 from re-analysis of the Cape Grim Air Archive, Earth and Planetary Science Letters, 428, 134–138, doi:10.1016/j.epsl.2015.07.035, 2015.

Montzka, S. A., Dutton, G. S., Yu, P., Ray, E., Portmann, R. W., Daniel, J. S., Kuijpers, L., Hall, B. D., Mondeel, D., Siso, C., Nance, J. D., Rigby, M., Manning, A. J., Hu, L., Moore, F., Miller, B. R., and Elkins, J. W.: An unexpected and persistent increase in global emissions of ozone-depleting CFC-11, Nature, 557, 413–417, doi:10.1038/s41586-018-0106-2, 2018.

Nevison, C. D., Dlugokencky, E., Dutton, G., Elkins, J. W., Fraser, P., Hall, B., Krummel, P. B., Langenfelds, R. L., O'Doherty, S., Prinn, R. G., Steele, L. P., and Weiss, R. F.: Exploring causes of interannual variability in the seasonal cycles of tropospheric nitrous oxide, Atmospheric Chemistry and Physics, 11, 3713–3730, doi:10.5194/acp-11-3713-2011, 2011.

Oliver, B. M., Bradley, J. G., and Farrar IV, H.: Helium concentration in the Earth's lower atmosphere, Geochimica et Cosmochimica Acta, 48, 1759–1767, doi:10.1016/0016-7037(84)90030-9, 1984.

Pierson-Wickmann, A. C., Marty, B., and Ploquin, A.: Helium trapped in historical slags: A search for temporal variation of the He isotopic composition of air, Earth and Planetary Science Letters, 194, 165–175, doi:10.1016/S0012-821X(01)00554-4, 2001.

Ray, E. A., Moore, F. L., Rosenlof, K. H., Davis, S. M., Boenisch, H., Morgenstern, O., Smale, D., Rozanov, E., Hegglin, M., Pitari, G., Mancini, E., Braesicke, P., Butchart, N., Hardiman, S., Li, F., Shibata, K., and Plummer, D. A.: Evidence for changes in stratospheric transport and mixing over the past three decades based on multiple data sets and tropical leaky pipe analysis, Journal of Geophysical Research Atmospheres, 115, 1–16, doi:10.1029/2010JD014206, 2010.

Ray, E. A., Moore, F. L., Rosenlof, K. H., Davis, S. M., Sweeney, C., Tans, P., Wang, T., Elkins, J. W., Bönisch, H., Engel, A., Sugawara, S., Nakazawa, T., and Aoki, S.: Improving stratospheric transport trend analysis based on SF6 and CO2 measurements, Journal of Geophysical Research: Atmospheres, 119, 14 110–14 128, doi:10.1002/2014JD021802, 2014.

Reid, R. C., Prausnitz, J. M., and Poling, B. E.: The properties of gases and liquids, McGraw-Hill, New York, 4 edn., 1987.

Salby, M. L. and Callaghan, P. F.: Influence of the Brewer-Dobson circulation on stratosphere-troposphere exchange, Journal of Geophysical Research Atmospheres, 111, 1–9, doi:10.1029/2006JD007051, 2006.

Sano, Y., Wakita, H., Makide, Y., and Tominaga, T.: A ten-year decrease in the atmospheric helium isotope ratio possibly caused by human activity, Geophysical Research Letters, 16, 1371–1374, doi:10.1029/GL016i012p01371, 1989.

Sano, Y., Furukawa, Y., and Takahata, N.: Atmospheric helium isotope ratio: Possible temporal and spatial variations, Geochimica et Cosmochimica Acta, 74, 4893–4901, doi:10.1016/j.gca.2010.06.003, 2010.

Sano, Y., Marty, B., and Burnard, P.: Noble Gases in the Atmosphere, in: The Noble Gases as Geochemical Tracers, edited by Burnard, P., pp. 17–31, Springer Berlin Heidelberg, 2nd edn., doi:10.1007/978-3-642-28836-4_2, 2013.

Simmonds, P. G., Manning, A. J., Athanassiadou, M., Scaife, A. A., Derwent, R. G., O'Doherty, S., Harth, C. M., Weiss, R. F., Dutton, G. S., Hall, B. D., Sweeney, C., and Elkins, J. W.: Interannual fluctuations in the seasonal cycle of nitrous oxide and chlorofluorocarbons due to the Brewer-Dobson circulation, Journal of Geophysical Research Atmospheres, 118, 10 694–10 706, doi:10.1002/jgrd.50832, 2013.

Sugawara, S., Ishidoya, S., Aoki, S., Morimoto, S., Nakazawa, T., Toyoda, S., Inai, Y., Hasebe, F., Ikeda, C., Honda, H., Goto, D., and Putri, F. A.: Age and gravitational separation of the stratospheric air over Indonesia, Atmospheric Chemistry and Physics, 18, 1819–1833, doi:10.5194/acp-18-1819-2018, 2018.

Torgersen, T.: Terrestrial helium degassing fluxes and the atmospheric helium budget: Implications with respect to the degassing processes of continental

crust, Chemical Geology: Isotope Geoscience Section, 79, 1–14, doi:10.1016/0168-9622(89)90002-X, 1989.

Weiss, R. F.: Solubility of helium and neon in water and seawater, Journal of Chemical & Engineering Data, 16, 235–241, doi:10.1021/je60049a019, 1971.

Zartman, R. E., Wasserburg, G. J., and Reynolds, J. H.: Helium, Argon, and Carbon in Some Natural Gases, Journal of Geophysical Research, 66, 277–306, doi:10.1029/jz066i001p00277, 1961.

Chapter 4

Increase in atmospheric He/N_2 from anthropogenic fossil fuel exploitation

4.1 Abstract

The atmospheric abundance of He is expected to increase with time due to incidental release of He from fossil fuel extraction. However, a clear buildup of He in the atmosphere has not previously been detected. Here we present results from a novel mass spectrometry technique that can constrain relative changes in $^4He/N_2$ at an unprecedented precision of 0.07 per mille (2σ) for a single air sample, and apply the new method to analyze 46 air samples acquired between 1974 and 2020. The atmospheric helium-to-nitrogen ($^4He/N_2$) ratio provides a direct measure of the atmospheric ^4He rise because relative changes in N_2 are negligible. We observe an increase in $\delta(^4He/N_2)$ of +1.9 per mille between 1974 and 2020, corresponding to an average rate of $+0.042\pm0.003$ per mille y^{-1} (2σ). This ties together observations and theoretical predictions of an anthropogenic signature in atmospheric helium and

places tight boundaries on the trend. When compared to previous observations of the atmospheric $^3He/^4He$ trend, the +1.9 per mille increase of ^4He implies an unknown ^3He source of 63000±25000 mol y^{-1}. The ^4He trend mirrors the buildup of atmospheric CO_2, providing an additional measure of the impact of fossil fuel burning on the composition of the global atmosphere.

4.2 Introduction

Fossil fuels are enriched in ^4He from radioactive decay of thorium and uranium in the Earth's crust. Anthropogenic fossil fuel extraction has therefore greatly increased the release of crustal ^4He to the atmosphere over the natural background state (Sano et al., 1989; Oliver et al., 1984; Mabry et al., 2015; Boucher et al., 2018; Brennwald et al., 2013; Sano et al., 2010; Pierson-Wickmann et al., 2001; Torgersen, 1989; Banks and Kockarts, 1973; Sano et al., 2013).

Changes in the atmospheric $^3He/^4He$ ratio are often regarded as a proxy measurement for trends in tropospheric helium concentration because helium in fossil fuel has a low $^3He/^4He$ ratio relative to air. $^3He/^4He$ studies over the last four decades have yielded conflicting results, with bottom-up calculations (Oliver et al., 1984; Pierson-Wickmann et al., 2001; Sano et al., 2013) and early observational studies (Sano et al., 1991, 1989) supporting the existence of an anthropogenic signal in helium isotopes, whereas recent measurements with improved error margins constrain any atmospheric $^3He/^4He$ trend to be indistinguishable from zero (Mabry et al., 2015; Lupton and Evans, 2013, 2004; Boucher et al., 2018). However, the precision of helium isotope measurements is currently limited to about 1 per mille due to the low abundance of the rare isotope ^3He in the atmosphere, and sources of ^3He could mask some of the expected fossil fuel signal in $^3He/^4He$ (Boucher et al., 2018; Lupton and Evans, 2004).

Here we present an alternative approach for observing a potential rise in atmo-

spheric helium based on high precision measurements of $\delta(^4He/N_2)$ in archived air samples. This method provides a more direct measure of changes in ^4He and achieves an almost 2 order of magnitude higher accuracy thanks to very stable atmospheric N_2 levels and a much greater abundance of ^4He than ^3He.

4.3 Methods

4.3.1 Delta values definition

We report changes in $^4He/N_2$ in delta notation:

$$\delta(^4He/N_2) = \frac{(^4He/N_2)_{SA}}{(^4He/N_2)_{ST}} - 1 \tag{4.1}$$

where subscripts SA and ST refer to the ratio in a sample and standard reference gas, respectively. $\delta(^4He/N_2)$ is either multiplied by 10^3 and reported in "per mille" units or multiplied by 10^6 and expressed in "per meg" units.

4.3.2 Sampling

We analyzed the composition of clean ambient air pumped into pressurized containers by different laboratory groups at irregular times over the last five decades. The samples broadly fall into two groups: those collected in high-pressure cylinders made from aluminum or chrome-molybdenum steel (herein called "high-pressure cylinders"), and those collected in 34 L stainless steel "Essex tanks" (Essex Cryogenics, Missouri, USA). The properties of all samples used in this study are detailed in Table 4.2.

Essex tanks

All but one Essex tanks were pumped as Advanced Global Atmospheric Gases Experiment (AGAGE) standards at either La Jolla or Trinidad Head on a RIX oil-free

compression pump up to 600–900 psi (4.1–6.2 Mpa) without any purification stage (Prinn et al., 2018, 2000). Small amounts of deionized water were added during the filling processes to cool the pump. Essex tank G-038 was filled at Cape Grim using the cryogenic air sampling system described in Brennwald et al. (2013). Essex tanks are sealed with all-metal valves connected to the tank body using metal-to-metal seals or elastomer-coated National Pipe Tapered (NPT) thread. Nine Essex tanks were excluded from this analysis because they exhibit a clear 2–5 per mille positive bias in the helium mole fraction compared to other tanks filled at similar times. For the excluded tanks, no corresponding anomaly is evident in Ar/N_2 or O_2/N_2, which suggests that these samples were contaminated with helium at the time of filling. Furthermore, Essex tanks with a remaining pressure below 1.5 MPa were not considered due to an apparent fractionation emerging only at very low pressures (SI).

Aluminum and chrome-molybdenum steel cylinders

All high-pressure cylinders were pumped at Scripps Institution of Oceanography (SIO) using a separate RIX pump, with additional chemical processing specific to individual tanks. The processing variously included any of the following: passing through high-pressure columns containing Ascarite, $Mg(ClO_4)_2$, or 13X molecular sieve, Aquasorb® and additions of pure CO_2, N_2, and O_2. We expect these modifications to impact only select gases, with generally small or correctable impacts on He/N_2. The use of 13X molecular sieve was common in the earlier part of the record but no complete documentation of this is available in the lab notebooks. Air was also temporarily archived on occasion for later use, but was typically stored for no longer than a few weeks. Some cylinders contain a blend of air from up to 3 different sampling dates which was subsequently combined using a Corblin diaphragm compressor. We only consider cylinders with multiple fill dates if they are less than a year apart and assign a representative fill date based on the contribution of each

date to the overall cylinder composition. Many of the cylinders have been used to create Northern Hemisphere background records for perfluorocarbons CF_4, C_2F_6, and C_3F_8 (Mühle et al., 2010). We update the fill history of Mühle et al. (2010) based on additional old logs and lab notebooks. Cylinder LL9082 was filled with the same pumping system used for the Essex tanks and demonstrates the comparability of the two filling systems. We exclude Viton-sealed cylinders from our analysis due to known issues with permeation (Keeling et al., 2007).

4.3.3 Summary of analysis methods

Our measurements of $^4He/N_2$ are based on a new mass spectrometric analysis method described in Birner et al. (2020b). The measurement relies on stabilizing the flow of air to a mass spectrometer (MS) to very high precision and monitoring changes in the $^4He^+$ beam while switching between a sample and reference gas. Variability in the $^4He^+$ beam can thus be interpreted as a measure of the difference in helium mole fraction between the sample and standard gas. The helium mole fraction measurement can be combined with measured changes in O_2/N_2, Ar/N_2 and the CO_2 mole fraction to calculate the change in $^4He/N_2$ using the equation given by Birner et al. (2020b):

$$\delta(\mathrm{He/N_2}) \approx \delta(\mathrm{He/M}) + \delta(\mathrm{O_2/N_2})\mathrm{X_{O_2}} + \delta(\mathrm{Ar/N_2})\mathrm{X_{Ar}} + \mathrm{dX_{CO_2}} \tag{4.2}$$

where δ(He/M) is the helium mole fraction expressed in delta notation following eq. 4.1 with $\mathrm{M} \equiv \mathrm{N_2} + \mathrm{O_2} + \mathrm{Ar} + \mathrm{CO_2} + \cdots$. $\mathrm{X_{O_2}}$ and $\mathrm{X_{Ar}}$ are a representative values of the atmospheric oxygen and argon mole fraction, and $\mathrm{dX_{CO_2}}$ denotes the change in the CO_2 mole fraction.

Air is gettered before entry into the MS to remove all non-noble gases and effectively concentrate He by a factor of ∼100. Where available, repeat measurements of He/M were averaged. All samples were measured against the same reference gas

cylinder and He/N_2 data are reported relative to the mean of all samples collected in 2020.

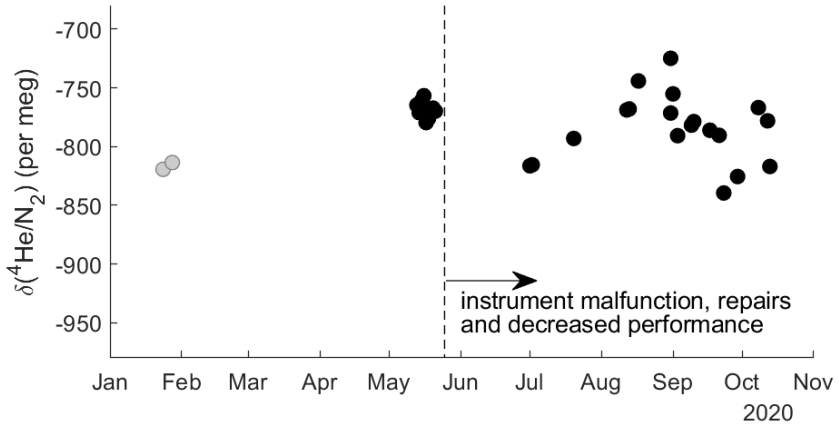

Figure 4.1: Repeat analysis of the same sample and standard cylinder combination (black circles). Cylinder ND33676 was first measured in January 2020 before the open split biases were calibrated (gray circles). Major changes to the analysis system were made at the end of May 2020 and previous performance was never fully recovered as highlighted on the graphic.

The reproducibility of repeat measurements of one standard cylinder over 8 months is 26 per meg, but performance of the instrument was not uniform over the period of measurements (Fig. 4.1). Before 25-May-2020 and following a careful calibration of the inlet system, a reproducibility of 10 per meg was achieved as reported by Birner et al. (2020b). After 25-May-2020, a lower reproducibility of 29 per meg was obtained. The degradation followed several repairs to the analysis system including replacement of the sample and standard gas delivery lines to the pressure-stabilizing inlet system, replacement of multiple MS electronic parts and the replacement of the entire MS source assembly, which required a recalibration of fractionation in the open split. As a conservative estimate, we use the reproducibility of 29 per meg after the repairs as a conservative estimate of $^4He/N_2$ measurement uncertainty. This precision is more than sufficient to resolve the expected per mille

level changes in He/N_2 since the 1970s. Measurements of O_2/N_2, Ar/N_2, and CO_2 in high-pressure cylinders were made using instrumentation and methods described by Keeling et al. (1998) and Keeling et al. (2004). These data have a 1σ reproducibility of 2 per meg, 3 per meg and 0.03 ppm in O_2/N_2, Ar/N_2, and CO_2, respectively. CO_2 readings were taken from a Picarro G2401 analyzer for samples with CO_2 below 200 ppm due to concerns about the calibration validity of the primary instrumentation at such low CO_2 concentrations. Measurements of O_2/N_2, Ar/N_2, and CO_2 in Essex tanks were analyzed using the same method but using a second analysis system that included a separate a GV Isoprime mass spectrometer and a Licor Li-6251 CO_2 analyzer. The second instrument requires $\sim$10 times less gas for analysis, thus reducing sample usage. Repeatability of Ar/N_2, O_2/N_2, and CO_2 measurements on the second system was 6 per meg, 2 per meg and 0.02 ppm (1σ), respectively. The secondary mass spectrometer was calibrated with respect to the primary instrument by repeat measurements of a single standard.

4.3.4 Helium leakage testing

The He/N_2 content of compressed air stored in high-pressure cycliners may potentially have decreased over time due to preferential permeation of He relative to N_2 through elastomeric seals, such as elastomeric valve seats and teflon tape for pipe threads on the head valves. To quantify the relevant He permeation rates, we exposed the cylinder head valves of several teflon-sealed and o-ring-sealed cylinders to 1–2 atmospheres of pure helium for 4–6 weeks. This process reverses and amplifies the partial pressure gradient of He between the environment and the cylinder, thus accelerating permeation. A leak sufficient to produce a 1 per meg drift in 1 year during storage, would yield a drift of roughly 10 per meg per day in the experiment. Cylinders were analyzed before and after exposure to the excess helium, allowing an additional month for the cylinder to rest after exposure before follow-on analysis.

The drift rates in the experiment were scaled downwards by the ratio of the natural to amplified helium gradients to assess the expected actual drift rates of these tanks.

The permeation rates for select cylinders are summarized in Table 3.2 and constrain equivalent $^4He/N_2$ loss rates in our samples to 3 per meg or less per year. In contrast, cylinder ND01645 is suspected to have a compromised seal and produced a leak rate of 215 per meg per year, demonstrating the sensitivity of our test setup.

We expect the He/N_2 drift rates of the Essex tanks are comparable or smaller than that of the high-pressure cylinders. Essex tanks are sealed by all-metal valves connected to the tank body either via metal-to-metal Swagelok connections or Teflon tape seals on pipe threads. Our tests with high-pressure cylinders suggest that Teflon tape produces sufficiently tight seals to prevent problematic drift. Furthermore, we see no evidence in the time series for a dependence of $^4He/N_2$ on the seal type (see also Fig. 4.4).

Table 4.1: Summary of experimental conditions for helium permeation experiments with high-pressure cylinders.

Cylinder Name	Seal type	Duration (days)	^{4}He pressure differential (Pa)	$^4He/N_2$ change (per meg)	Tank pressure (MPa)	Estimated $^4He/N_2$ drift rate (per meg y^{-1})
CDK10068Q	NPT	37.98	1.08E+05	262.32	11.03	1.33
CDK34816Q	NPT	37.98	1.08E+05	446.1	5.38	1.1
CDK3758Q	NPT	37.98	1.08E+05	108.65	9.65	0.48
CDK7357Q	NPT	39.38	2.05E+05	387.71	13.79	1.26
ND33777	NPT	37.98	1.08E+05	154.12	13.79	0.98
cc105762	Metal o-ring	47.06	1.84E+05	1769.4	7.58	2.92
ND01645	Metal o-ring	4.71	2.05E+05	22963	4.83	215.38

4.3.5 $^4He/N_2$ artifactual fractionation correction

We apply a small correction to $^4He/N_2$ data from high-pressure cylinders based on an apparent correlation with biases in Ar/N_2 compared to true atmospheric concentrations:

$$\delta(^4He/N_2) = \delta(^4He/N_2)_{raw} + (2.02 \pm 0.12) \times [\Delta(Ar/N_2) - \Delta(Ar/N_2)_{2020}] \quad (4.3)$$

where $\delta(^4He/N_2)_{raw}$ are the uncorrected He/N_2 observations, $\Delta(Ar/N_2)$ is the Ar/N_2 anomaly, and $\Delta(Ar/N_2)_{2020}$ is the mean Ar/N_2 anomaly of cylinders in 2020. $\Delta(Ar/N_2)$ is defined as the difference between measured values in each cylinder and the true atmospheric value at the time of filling which was estimated based on extrapolating a fit to 15 years of flask data at La Jolla (Keeling et al., 2004) (Fig. 4.5). The correction coefficient is given by the slope of the best fit line (York et al., 2004) for the relationship between $\Delta(Ar/N_2)$ and the He/N_2 anomaly $\Delta(He/N_2)$ (Fig. 4.6). In the absence of a known atmospheric history, $\Delta(He/N_2)$ is instead defined as the deviation of each sample from a second order polynomial fit to the uncorrected $^4He/N_2$ data (Fig. 4.5). For an Ar/N_2 anomaly of 200±6 per meg, the correction adds an uncertainty of 20 per meg to our $^4He/N_2$ observation, increasing the overall uncertainty to 35 per meg. Data from samples with $\Delta(Ar/N_2)$ exceeding 200 per meg are rejected. Essex tank data are uncorrected. A mechanism for the combined fractionation of Ar/N_2 and He/N_2 remains unclear. However, similarly correlated Ar/N_2 and He/N_2 anomalies were observed in an experiment in which cylinders were filled through a 13x molecular sieve, pointing to adsorption as a key process responsible for the artifactual fractionation. Adsorption is also consistent with a near 1:1 relationship observed between $\Delta(Ar/N_2)$ and $\Delta(O_2/N_2)$, where the O_2/N_2 anomaly $\Delta(O_2/N_2)$ is defined analogously to $\Delta(Ar/N_2)$, but further work would be needed to confirm the adsorption hypothesis.

4.4 Results and Discussion

The observed change in atmospheric $^4He/N_2$ between 1974 and 2020 is ∼1.9 per mille, corresponding to an annual increase of 0.042±0.003 per mille (2σ error from bootstrapping) or 39±3 billion mol of ^4He (atmospheric ^4He inventory: 9.268×10^{14} mol, Fig. 4.2). This is two orders of magnitude greater than fluxes in the balanced natural background state characterized by slow crustal degassing and

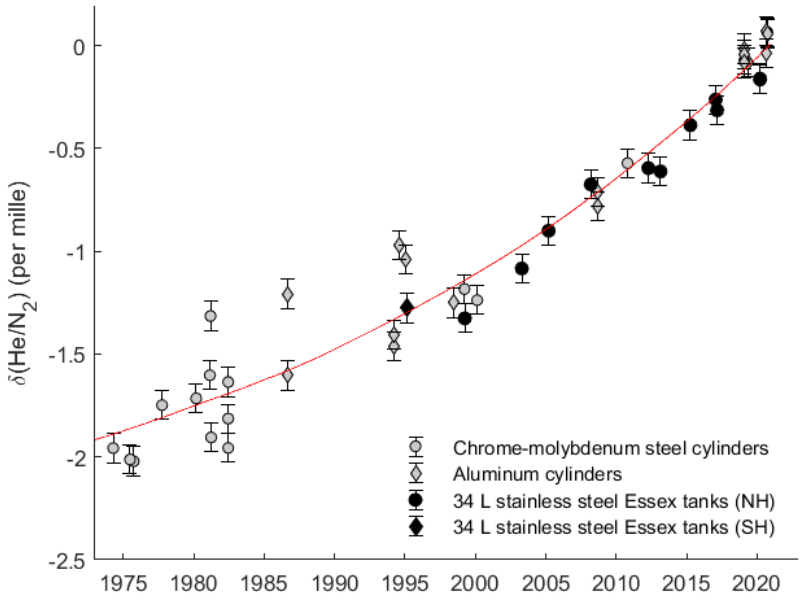

Figure 4.2: Atmospheric $^4He/N_2$ change relative to the average of samples from 2020 measured in high-pressure chrome-molybdenum steel cylinders (grey circles), aluminum cylinders (gray diamonds), 34 L stainless steel Essex tank filled in the Northern Hemisphere (NH, black circles) and one Essex tank filled at Cape Grim in the Southern Hemisphere (SH, black diamond) with 2σ error bars. Using independent observations of $\delta(Ar/N_2$ grey data points were corrected for a small bias introduced during sampling. The best-fit line (red) is obtained by scaling global cumulative natural gas emissions by a constant while maintaining the curvature of the emissions trend. The observed atmospheric buildup implies a mean helium content of 0.03% in natural gas assuming other fossil fuel contributions to the trend are negligible (Oliver et al., 1984)

He escape to space (Sano et al., 2013; Torgersen, 1989; Kockarts, 1973).

The spread of data points before 2000 is considerably larger than the analytical uncertainty and the scatter of data seen later in the record. This additional spread might reflect undocumented changes in the drying agent or could result from pumping on days with varying pollution levels. In contrast, Essex tanks were not subject to any chemical purification during sampling, which is reflected by their lower inter-sample

variability. Results from tanks G-038 filled at Cape Grim in 1995 on a different pumping system agree with the observations from the Northern Hemisphere.

The atmospheric $^4He/N_2$ trend may be explained by documented emissions of natural gas. We estimate total global emissions of natural gas by summing the emissions from (i) natural gas production, (ii) flaring, and (iii) fugitive fossil methane emissions, where (i) and (ii) are from the Global Carbon Budget (Friedlingstein et al., 2019; Gilfillan et al., 2019) and (iii) is from Hoesly et al. (2020) (Fig. 4.7). The fossil CH_4 emissions reported by Hoesly et al. (2020) were adjusted to bring the estimate in agreement with observed mean fossil CH_4 emissions reported by Hmiel et al. (2020) and multiplied by 1.25 to account for non-CH_4 components of natural gas. All emission records are extrapolated to 2021 using a smoothing spline. We fit a trendline to the atmospheric $^4He/N_2$ history (Fig. 4.2 red line) that is directly proportional to the total global natural gas emissions which yields a scale factor that corresponds to a mean ^{4}He content of 0.030±0.002% in natural gas (mol ^{4}He per mol C). This estimate of the helium content is considerably lower than values of 0.1% and 0.25% commonly used for global and U.S. natural gas in bottom-up estimates of the anthropogenic helium release (Oliver et al., 1984; Zartman et al., 1961; Pierson-Wickmann et al., 2001). Little is known about the helium content of oil or coal, and an additional source of helium from other fossil fuels would imply a lower mean helium content of natural gas. However, Oliver et al. (1984) showed that coal likely makes a negligible contribution to overall helium emissions due to its shorter age and insufficient uranium content. Furthermore, a large fraction of helium associated with oil and coal is presumably emitted as associated petroleum gas or coalbed methane and thus already properly accounted for in our estimate of fugitive emissions, flaring, or natural gas production. Nevertheless, further work on the helium content of different fossil fuels is needed to definitively attribute helium emissions to its sources.

Commercial usage of helium for manufacturing, research and medical equipment

cannot explain the atmospheric helium trend. Global helium production from 2010 to 2014 was between 5-8$\times 10^9$ mol y^{-1}(Mohr and Ward, 2014; Boucher et al., 2018). This corresponds to an increase in $^4He/N_2$ of roughly 0.005–0.008 per mille y^{-1}, or just 9–15% of the observed $\sim$0.054–0.057 per mille y^{-1} increase between 2010 and 2014, demonstrating that only a small fraction of the He extracted with fossil fuel is captured for commercial use. Other processes including groundwater discharge and stratospheric circulation changes can modulate tropospheric ^4He abundance but are likely too small to be responsible for the observed trend. Changes in the tropospheric $^4He/N_2$ caused by an acceleration of stratospheric circulation are likely smaller than 0.5 per meg y^{-1} (Birner et al., 2020a). The impact from natural degassing of fossil groundwater that has accumulated crustal He in regions previously frozen during the last glacial is likely of similar magnitude (Pierson-Wickmann et al., 2001; Brennwald et al., 2013). Likewise, we estimate that the effect of human groundwater use on He/N_2 is likely smaller than 1 per meg y^{-1}. Helium concentrations in groundwater typically fall between 10^{-8} and 10^{-5} cm^3(STP He) $cm^{-3}(H_2O)$ depending on the age of the water and geological setting (e.g., Datta et al., 1980; Kulongoski et al., 2008, 2005; Torgersen and Clarke, 1985). Human groundwater usage was 952 km^3 y^{-1} in 2010 (Wada and Bierkens, 2014) which places an upper limit on the degassing of helium from extracted groundwater of around 4.3×10^8 mol y^{-1} or 0.46 per meg y^{-1}.

The observed $^4He/N_2$ trend is generally lower than the estimated anthropogenic impact in most bottom-up ^4He budgets (Pierson-Wickmann et al., 2001; Oliver et al., 1984; Sano et al., 2013) and different from recently published helium isotope trend estimates (Fig. 4.3). Our observations are marginally consistent with an $^3He/^4He$ trends of -0.0095$\pm$0.033 per mille y^{-1} (2σ, effusion-corrected) suggested by Mabry et al. (2015), but disagree with results of +0.019$\pm$0.042 and +0.017$\pm$0.032 per mille y^{-1} (2σ) published by Boucher et al. (2018) and Lupton and Evans (2013).

In conjunction with previous studies of changes in atmospheric $^3He/^4He$, the observed $^4He/N_2$ trend puts important constraints on the release of ^3He to the at-

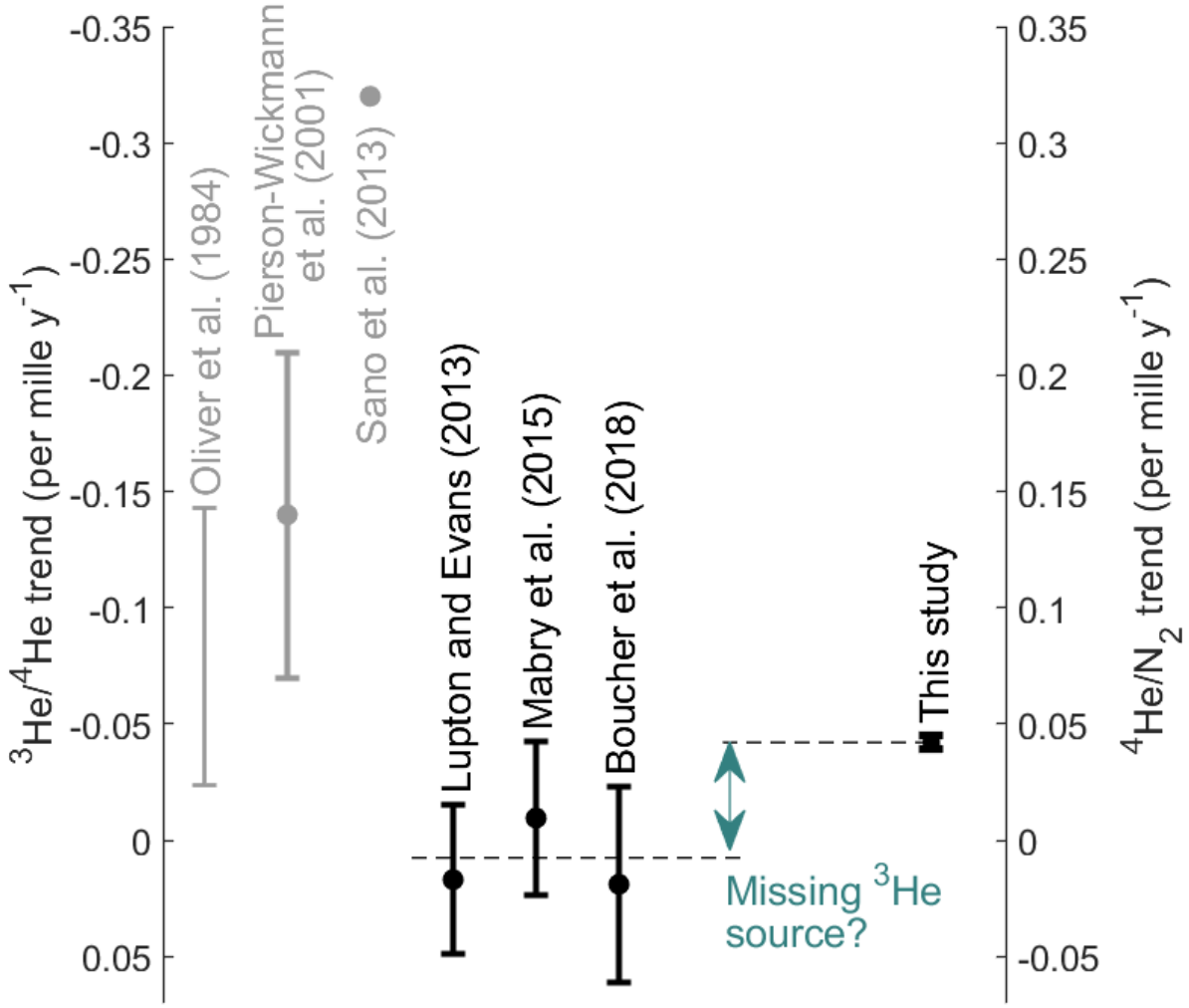

Figure 4.3: Predicted (gray) and observed trend (black) in atmospheric ^{3}He/^{4}He with 2σ error bars compared to the ^{4}He/N$_2$ trend measured. Dashed lines show the variance-weighted mean observed trend in ^{3}He/^{4}He and ^{4}He/N$_2$. Note the different orientation of the y-axes.

mosphere (Fig. 4.3). Averaging three independent observation of the ^{3}He/^{4}He trend weighted by variance (Boucher et al., 2018; Mabry et al., 2015; Lupton and Evans, 2013) yields a best estimate of $+8\pm20$ per meg y^{-1} (2σ). To explain the observed

trend in helium isotopes and $^4He/N_2$, a rise of $3He/N_2$ by 49±20 per meg y^{-1} is needed, which is equivalent to an additional release of about 63000±25000 mol ^3He per year into the atmosphere (atmospheric ^3He inventory: 1.27×10^9 mol). This increase is an order of magnitude greater than estimates of the natural ^3He flux into the atmosphere (Torgersen, 1989). One known anthropogenic source of ^3He is the radioactive decay of tritium from nuclear weapons testing and the aging of nuclear warheads. However, so far this radiogenic production of ^3He has been estimated to only account for ∼2700 mol y^{-1} or 4% of the required source (Boucher et al., 2018). Although the current analytical uncertainty in helium isotope analyses is limiting, our results suggest a large, currently unidentified source of ^3He to the atmosphere.

4.5 Conclusions

Measurements of the $^4He/N_2$ ratio in 46 high-pressure samples of old air using a new mass spectrometric technique (Birner et al., 2020a) reveal an atmospheric buildup of ^4He at 0.042±0.003 per mille y^{-1} (2σ), or 39±3 billion mol per year between 1974 and 2020. The atmospheric rise of $^4He/N_2$ accelerates from roughly 0.02 to 0.065 per mille y^{-1} over the record, matching the exponential rise in fossil fuel exploitation. Assuming helium release associated with natural gas emissions is the primary cause of the observed trend implies a mean helium content in natural gas of 0.030±0.002%, which is an order of magnitude less than commonly used estimates (Oliver et al., 1984; Zartman et al., 1961). A comparison of our results with previous observations of a near-zero trend in atmospheric $^3He/^4He$ (Mabry et al., 2015; Boucher et al., 2018; Lupton and Evans, 2013) suggests a so-far unidentified source of ^3He.

4.6 Appendix A: supplementary material

Appendix A is a reproduction of the supplementary materials to this paper:

Tank or cylinder pressure dependence of $^4He/N_2$

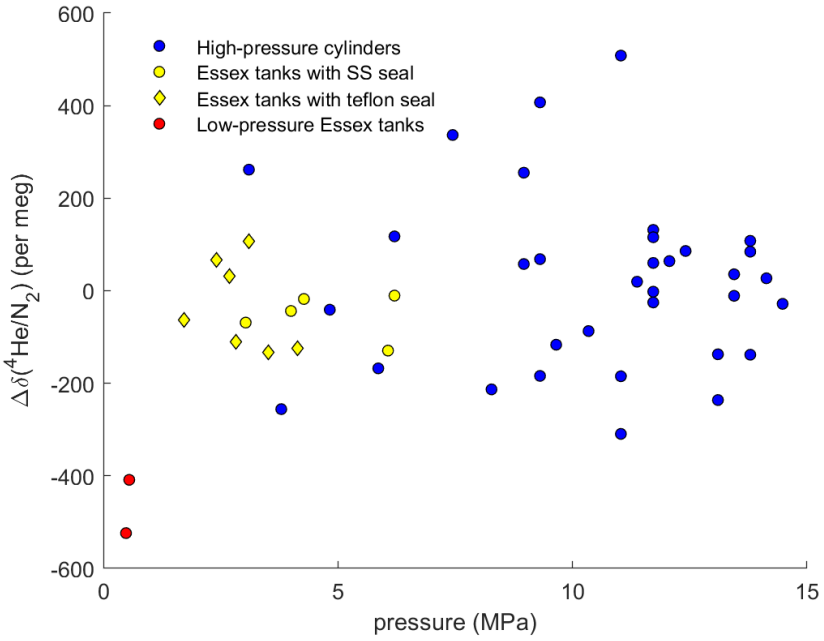

Figure 4.4: Relationship between pressure and the $^4He/N_2$ anomaly defined as the difference between the measured $^4He/N_2$ in each sample and our estimate of the atmospheric change (i.e, best fit line in Fig. 4.5). Essex tanks (yellow circles and diamonds) and high-pressure cylinders (blue circles) show no clear pressure dependence above 1.5 MPa. Two Essex tanks (red circles) with pressure below 1 MPa are clear outliers and their data are rejected. The $^4He/N_2$ anomaly in Essex tanks does not vary systematically between tanks using all stainless-steel seals (SS, yellow circles) and tanks using Teflon tape seals on tapered threads (yellow diamonds).

Time series of fractionation-uncorrected data

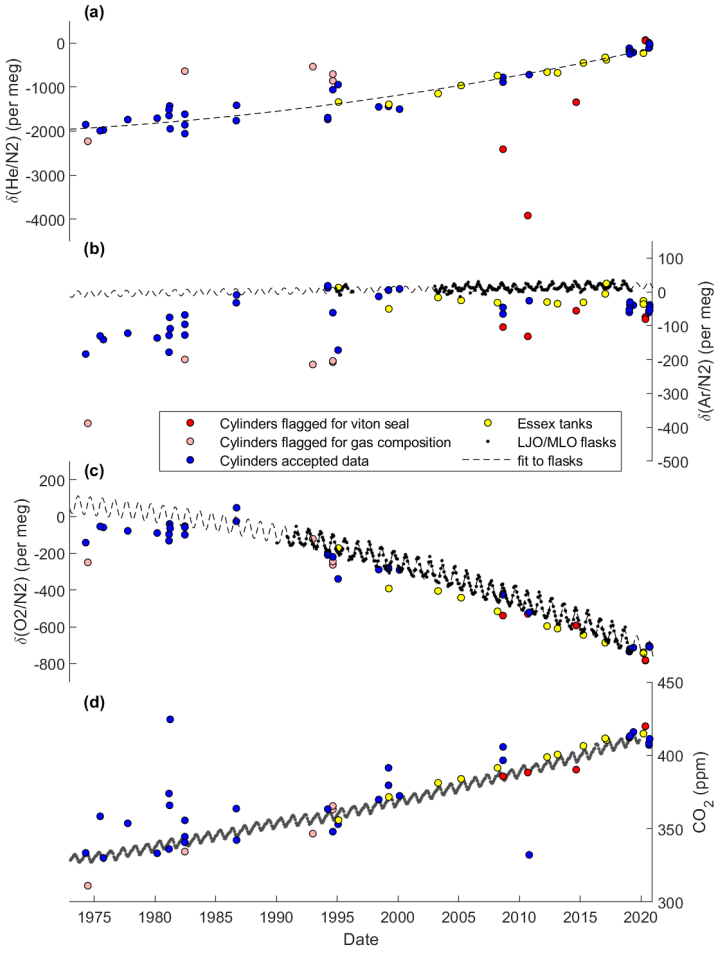

Figure 4.5: Uncorrected timeseries of (a) He/N_2, (b) Ar/N_2, (c) O_2/N_2 and (d) CO_2 in our samples. Monthly means of flask observations from La Jolla (LJO) and Mauna Loa (MLO) are shown for comparison with a polynomial fit of the trend and a one harmonic seasonal cycle. Results from high-pressure cylinders (blue circles) and Essex tanks (yellow circles) are shown separately. Data were quality screen as described in the text and samples rejected based on Viton seals (dark red circles) or Ar/N_2 deviations greater than 200 per meg from the fit to flask data (light red circles).

Relationships between anomalies in O_2/N_2, Ar/N_2, and $^4He/N_2$

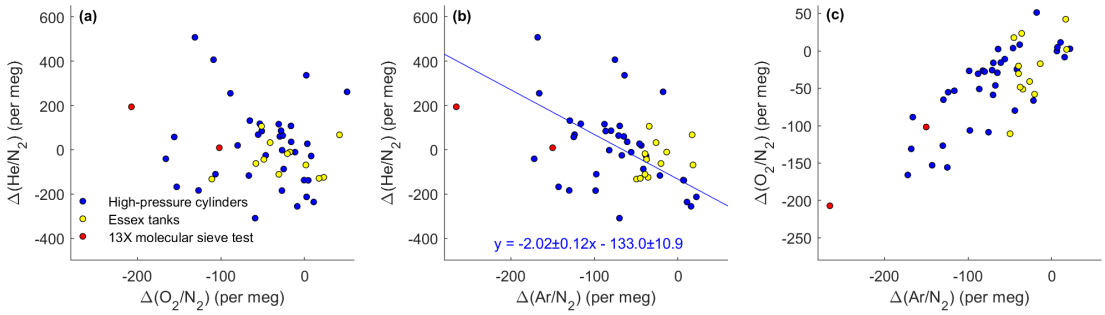

Figure 4.6: Relationships between (a) O_2/N_2 anomaly $\Delta(O_2/N_2)$ and $^4He/N_2$ anomaly $\Delta(^4He/N_2)$, (b) Ar/N_2 anomaly $\Delta(Ar/N_2)$ and $\Delta(^4He/N_2)$, and (c) $\Delta(Ar/N_2)$ and $\Delta(O_2/N_2)$. Best fit lines are calculated excluding data from Essex tanks and using the method of York et al. (2004). Red circles show results from test measurements of cylinders filled through 13X mole sieve previously used for different periods of time.

Total cumulative natural gas emissions

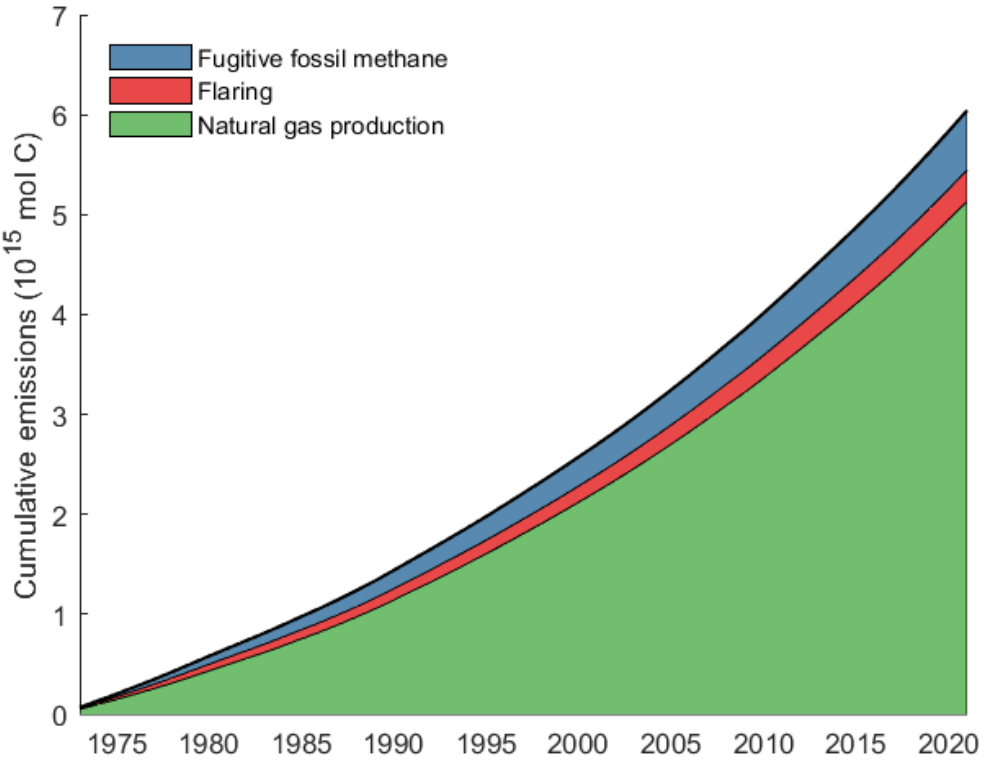

Figure 4.7: Cumulative global natural gas emissions from different sources. Data for natural gas production and flaring are from the Global Carbon Budget (Friedlingstein et al., 2019; Gilfillan et al., 2019). Data for fugitive fossil CH_4 emissions (Hoesly et al., 2020) were rescaled to bring them into agreement with observed mean fossil CH_4 emissions in 2003–2012 reported by Hmiel et al. (2020) and multiplied by 1.25 to account for carbon compounds other than CH_4 present in natural gas.

Table 4.2: Summary of old air sample information from high-pressure cylinders and Essex tanks. "Best Date" is an estimated, most representative pumping date for the air sample based on mixing proportions. LJO = La Jolla, TH = Trinidad Head, CMS = chrome-molybdenum steel, AL = aluminum, SS = stainless steel

ID	**Best Date**	**Content**	**All Pumping Dates**	**Pumping Location**	**Pump Type**	**Drying Agent**	**Seal Material**	**Tank Material**	**Pressure (Mpa)**
CDK35380Q	18-Apr-74	temp. stored air, $-CO_2$	1-Apr-74	LJO	Keeling RIX	?	Teflon tape	CMS	4.8
CDK34816Q	21-Jun-74	ambient air, $+N_2$	1-Jun-74	LJO	Keeling RIX	?	Teflon tape	CMS	5.4
CDK35378Q	27-Jun-75	temp. stored air, $+CO_2$	1-Jun-75	LJO	Keeling RIX	?	Teflon tape	CMS	9.3
CDK35354Q	1-Oct-75	temp. stored air, $-CO_2$	1-Oct-75	LJO	Keeling RIX	?	Teflon tape	CMS	5.9
CDK63981Q	4-Oct-77	ambient air, $+CO_2$	1-Oct-77	LJO	Keeling RIX	?	Teflon tape	CMS	9
CDK63968Q	6-Mar-80	ambient air	1-Mar-80	LJO	Keeling RIX	?	Teflon tape	CMS	9.3
CDK15891Q	26-Feb-81	ambient air, $+CO_2$	1-Feb-81	LJO	Keeling RIX	?	Teflon tape	alumnium	6.2
cc15883Q	26-Feb-81	mix of ambient air $+CO_2$ and ambient air $-CO_2$	10-Feb-81 & 26-Feb-81	LJO	Keeling RIX & Corblin	?	Teflon tape	CMS	9
CDK62817Q	15-Mar-81	mix of ambient air $+CO_2$ and ambient air $-CO_2$	26-Feb-81 & 26-Mar-81	LJO	Corblin	?	Teflon tape	CMS	7.4
CDK62829Q	1-Apr-81	mix of 2x ambient air, $+CO_2$	early 1981 & 3-Apr-81	LJO	Keeling RIX	?	Teflon tape	CMS	11
CDK10068Q	16-Jun-82	mix of 3x ambient air, $+CO_2$	16-Jun-82 & 2x 30-Mar-82	LJO	Keeling RIX and Corblin	?	Teflon tape	CMS	11
CDK2425	16-Jun-82	mix of 2x ambient air, $-CO_2$	16-Jun-82 & 16-Jun-82	LJO	Keeling RIX & Corblin	?	Teflon tape	CMS	10
CDK3758Q	16-Jun-82	mix of 2x ambient air, $+CO_2$	16-Jun-82 & 16-Jun-82	LJO	Corblin	?	Teflon tape	CMS	9.7
CDK75902Q	16-Jun-82	ambient air , $+CO_2$	1-Jun-82	LJO	Keeling RIX	?	Teflon tape	CMS	11.7
ha6999	10-Sep-86	ambient air	1-Sep-86	LJO	Keeling RIX	?	Teflon tape	AL	10.3
ha7014	18-Sep-86	ambient air	1-Sep-86	LJO	Keeling RIX	?	Teflon tape	AL	3.1
ND01598	29-Dec-92	CO2 free ambient air, $+O_2$, $+CO_2$	1-Dec-92	NCAR	?	Ascarite, ?	Metal o-ring	AL	6.9
cc70015	22-Mar-94	ambient air, $+N_2O$,$+CO_2$	1-Mar-94	LJO	Keeling RIX	Aquasorb®	Teflon tape	AL	3.8
cc70345	22-Mar-94	ambient air, $+N_2O$,$+CO_2$	1-Mar-94	LJO	Keeling RIX	Aquasorb®	Teflon tape	AL	8.3

Continued on next page

Table 4.2 – *Continued from previous page*

ID	Best Date	Content	All Pumping Dates	Pumping Location	Pump Type	Drying Agent	Seal Material	Tank Material	Pressure (Mpa)
cc105762	22-Aug-94	ambient air	1-Aug-94	LJO	Keeling RIX	?	Metal o-ring	AL	7.6
cc106697	22-Aug-94	ambient air	1-Aug-94	LJO	Keeling RIX	?	Teflon tape	AL	5.5
cc106703	22-Aug-94	ambient air	1-Aug-94	LJO	Keeling RIX	?	Teflon tape	AL	9.3
ND02698	26-Jan-95	ambient air	1-Jan-95	LJO	Keeling RIX	?	Teflon tape	AL	11
EssexG-038	8-Feb-95	ambient air, not dried	1-Feb-95	Cape Grim	cryogenic pump	none	Teflon tape	SS	2.4
LL9082	2-Jun-98	ambient air	1-Jun-98	LJO	AGAGE RIX	Aquasorb®	Teflon tape	AL	9.7
CDK4287Q	23-Mar-99	mix of 2x ambient air, $+CO_2$	23-Mar-99 & 23-Mar-99	LJO	Keeling RIX & Corblin	?	Teflon tape	CMS	13.1
CDK7357Q	23-Mar-99	mix of 2x ambient air, $-CO_2$	23-Mar-99 & 14-Sep-99	LJO	Keeling RIX & Corblin	?	Teflon tape	CMS	13.8
EssexJ-040	1-Apr-99	ambient air, not dried	1-Apr-99	LJO	AGAGE RIX	none	Teflon tape	SS	3.5
CDK6074Q	17-Feb-00	ambient air	1-Feb-00	LJO	Keeling RIX	?	Teflon tape	CMS	13.1
EssexT-003A	20-Apr-03	ambient air, not dried	1-Apr-03	TH	AGAGE RIX	none	Teflon tape	SS	1.7
EssexT-004	14-Mar-05	ambient air, not dried	1-Mar-05	TH	AGAGE RIX	none	Teflon tape	SS	2.7
EssexT-007	12-Mar-08	ambient air, not dried	1-Mar-08	TH	AGAGE RIX	none	Teflon tape	SS	3.1
ND32982	25-Aug-08	mix of 2x ambient air and 2006 CO2 free air	2006 & 18-Aug to 25-Aug-08 & 22-Sep-08	LJO	Keeling RIX & Corblin	?	Viton o-ring	AL	10.7
ND33676	25-Aug-08	mix of 2x ambient air, $+CO_2$	18-Aug to 25-Aug-08 & 18-Aug to 25-Aug-08	LJO	RIX and Corblin	?	Teflon tape	AL	11.7
ND33777	25-Aug-08	mix of 2x ambient air	18-Aug to 25-Aug-08 & 18-Aug to 25-Aug-08	LJO	RIX and Corblin	?	Teflon tape	AL	13.8

Continued on next page

Table 4.2 – *Continued from previous page*

ID	Best Date	Content	All Pumping Dates	Pumping Location	Pump Type	Drying Agent	Seal Material	Tank Material	Pressure (Mpa)
ND01645	9-Sep-10	ambient air, $+CO_2$, compromised seal	1-Sep-10	LJO	Keeling RIX	?	Metal o-ring	AL	4.8
CDK7364	21-Oct-10	ambient air, $-CO_2$	1-Oct-10	LJO	Keeling RIX	?	Teflon tape	CMS	11.4
EssexT-011B	11-Apr-12	ambient air, not dried	1-Apr-12	LJO	AGAGE RIX	none	SS	SS	4
EssexT-012	20-Feb-13	ambient air, not dried	1-Feb-13	LJO	AGAGE RIX	none	Teflon tape	SS	2.8
ND17376	3-Sep-14	ambient air	1-Sep-14	LJO	Keeling RIX	$Mg(ClO_4)_2$	Viton o-ring	AL	9
EssexT-013	7-Apr-15	ambient air, not dried	1-Apr-15	LJO	AGAGE RIX	none	SS	SS	4.3
EssexLJ-139	24-Jan-17	ambient air, not dried	1-Jan-17	LJO	AGAGE RIX	none	SS	SS	6.2
EssexJ-209	28-Feb-17	ambient air, not dried	1-Feb-17	LJO	AGAGE RIX	none	SS	SS	3
ND59724	18-Jan-19	ambient air	1-Jan-19	LJO	Keeling RIX	$Mg(ClO_4)_2$	Teflon tape	AL	13.8
ND59728	18-Jan-19	ambient air	1-Jan-19	LJO	Keeling RIX	$Mg(ClO_4)_2$	Teflon tape	AL	13.4
ND59730	5-Feb-19	ambient air	1-Feb-19	LJO	Keeling RIX	$Mg(ClO_4)_2$	Teflon tape	AL	14.1
ND59731	5-Feb-19	ambient air	1-Feb-19	LJO	Keeling RIX	$Mg(ClO_4)_2$	Teflon tape	AL	14.5
ND28178	19-May-19	ambient air	1-May-19	LJO	Keeling RIX	$Mg(ClO_4)_2$	Teflon tape	AL	13.4
Essex5390	17-Mar-20	ambient air, not dried	1-Mar-20	LJO	AGAGE RIX	none	Teflon tape	SS	4.1
EssexLJ-174	17-Mar-20	ambient air, not dried	1-Mar-20	LJO	AGAGE RIX	none	Teflon tape	SS	0.5
EssexLJ-177	17-Mar-20	ambient air, not dried	1-Mar-20	LJO	AGAGE RIX	none	SS	SS	0.6
EssexMIT7547	17-Mar-20	ambient air, not dried	1-Mar-20	LJO	AGAGE RIX	none	SS	SS	6.1
cc113311	15-May-20	ambient air	1-May-20	LJO	Keeling RIX	$Mg(ClO_4)_2$	Viton o-ring	AL	NaN
cc173464	15-May-20	ambient air	1-May-20	LJO	Keeling RIX	$Mg(ClO_4)_2$	Viton o-ring	AL	12.4
JB03350	1-Sep-20	test: air filled through 13X molecular sieve	1-Sep-20	LJO	Keeling RIX	13X molecular sieve	Teflon tape	AL	11.7
JB03682	1-Sep-20	ambient air	1-Sep-20	LJO	Keeling RIX	$Mg(ClO_4)_2$	Teflon tape	AL	11.7
JJ12920	1-Sep-20	ambient air, not dried	1-Sep-20	LJO	Keeling RIX	none	Teflon tape	AL	11.7
CDK465060	21-Sep-20	ambient air	1-Sep-20	LJO	Keeling RIX	$Mg(ClO_4)_2$	Teflon tape	CMS	11.7
JB03075	21-Sep-20	ambient air, not dried	1-Sep-20	LJO	Keeling RIX	none	Teflon tape	AL	12.1
JB03420-A	21-Sep-20	test: air filled through 13X molecular sieve	1-Sep-20	LJO	Keeling RIX	13X molecular sieve	Teflon tape	AL	12.4

Continued on next page

Table 4.2 – *Continued from previous page*

ID	Best Date	Content	All Pumping Dates	Pumping Location	Pump Type	Drying Agent	Seal Material	Tank Material	Pressure (Mpa)
JJ12924-A	21-Sep-20	ambient air	1-Sep-20	LJO	Keeling RIX	$Mg(ClO_4)_2$	Teflon tape	AL	12.4

4.7 Acknowledgements

We thank Ross Beaudette, Bill Paplawsky, Alan Seltzer, Sarah Shackleton, Jacob Morgan, Jessica Ng, Julia Dohner, Yuming Jin and Eric Morgan for comments and insightful discussions during the development and troubleshooting of the He/N_2 analysis method. We are grateful to Savannah Hatley, Adam Cox, and Timothy Lueker for locating many old cylinders and unearthing documentation of their history. This work would not have been possible without the support of Chris Harth who generously shared the AGAGE Essex tanks and advised on their use and history. We also thank Bill Paplawsky and Shane Clark for maintaining and operating the Ar/N_2, O_2/N_2 and CO_2 analysis systems in the Keeling laboratory. This work was supported by National Science Foundation grants MRI-1920369 and AGS-1940361.

Chapter 4, in part, is currently being prepared for publication of the material and is coauthored with Jeffrey Severinghaus, and Ralph Keeling. The dissertation author was the primary investigator and author of this material.

References

Banks, P. M. and Kockarts, G.: Aeronomy, Part B, Academic Press, New York, USA, 1 edn., 1973.

Birner, B., Chipperfield, M. P., Morgan, E. J., Stephens, B. B., Linz, M., Feng, W., Wilson, C., Bent, J. D., Wofsy, S. C., Severinghaus, J., and Ralph, F.: Gravitational separation of Ar/N2 and age of air in the lowermost stratosphere in airborne observations and a chemical transport model, Atmospheric Chemistry and Physics Discussions, pp. 1–34, doi:10.5194/acp-2020-95, 2020a.

Birner, B., Paplawsky, W., Severinghaus, J., and Keeling, R. F.: Measurements of atmospheric He/N2 as an indicator of fossil fuel extraction and strato-

spheric circulation, Atmospheric Measurement Techniques Discussions, pp. 1–25, doi:10.5194/amt-2020-313, 2020b.

Boucher, C., Marty, B., Zimmermann, L., and Langenfelds, R.: Atmospheric helium isotopic ratio from 1910 to 2016 recorded in stainless steel containers, Geochemical Perspectives Letters, 6, 23–27, doi:10.7185/geochemlet.1804, 2018.

Brennwald, M. S., Vogel, N., Figura, S., Vollmer, M. K., Langenfelds, R., Steele, L. P., Maden, C., and Kipfer, R.: Concentrations and isotope ratios of helium and other noble gases in the Earth's atmosphere during 1978 – 2011, Earth and Planetary Science Letters, 366, 27–37, doi:10.1016/j.epsl.2013.01.039, 2013.

Datta, P. S., Gupta, S. K., Jayasurya, A., Nijampurkar, V. N., Sharma, P., and Plusnin, M. I.: A survey of helium in ground water in parts of sabarmati basin in gujarat state and in the jaisalmer district, rajasthan, Hydrological Sciences Bulletin, 25, 183–193, doi:10.1080/02626668009491922, 1980.

Friedlingstein, P., Jones, M. W., O'Sullivan, M., Andrew, R. M., Hauck, J., Peters, G. P., Peters, W., Pongratz, J., Sitch, S., Le Quéré, C., DBakker, O. C., Canadell1, J. G., Ciais1, P., Jackson, R. B., Anthoni1, P., Barbero, L., Bastos, A., Bastrikov, V., Becker, M., Bopp, L., Buitenhuis, E., Chandra, N., Chevallier, F., Chini, L. P., Currie, K. I., Feely, R. A., Gehlen, M., Gilfillan, D., Gkritzalis, T., Goll, D. S., Gruber, N., Gutekunst, S., Harris, I., Haverd, V., Houghton, R. A., Hurtt, G., Ilyina, T., Jain, A. K., Joetzjer, E., Kaplan, J. O., Kato, E., Goldewijk, K. K., Korsbakken, J. I., Landschützer, P., Lauvset, S. K., Lefèvre, N., Lenton, A., Lienert, S., Lombardozzi, D., Marland, G., McGuire, P. C., Melton, J. R., Metzl, N., Munro, D. R., Nabel, J. E., Nakaoka, S. I., Neill, C., Omar, A. M., Ono, T., Peregon, A., Pierrot, D., Poulter, B., Rehder, G., Resplandy, L., Robertson, E., Rödenbeck, C., Séférian, R., Schwinger, J., Smith, N., Tans, P. P., Tian, H., Tilbrook, B., Tubiello, F. N., Van Der Werf, G. R., Wiltshire, A. J., and

Zaehle, S.: Global carbon budget 2019, Earth System Science Data, 11, 1783–1838, doi:10.5194/essd-11-1783-2019, 2019.

Gilfillan, D., Marland, G., Boden, T., and Andres, R.: Global, Regional, and National Fossil-Fuel CO2 Emissions, URL https://energy.appstate.edu/CDIAC, 2019.

Hmiel, B., Petrenko, V. V., Dyonisius, M. N., Buizert, C., Smith, A. M., Place, P. F., Harth, C., Beaudette, R., Hua, Q., Yang, B., Vimont, I., Michel, S. E., Severinghaus, J. P., Etheridge, D., Bromley, T., Schmitt, J., Faïn, X., Weiss, R. F., and Dlugokencky, E.: Preindustrial 14CH4 indicates greater anthropogenic fossil CH4 emissions, Nature, 578, 409–412, doi:10.1038/s41586-020-1991-8, 2020.

Hoesly, R. M., O'Rourke, P. R., Smith, S. J., Feng, L., Klimont, Z., Janssens-Maenhout, G., Pitkanen, T., Seibert, J. J., Vu, L., Andres, R. J., Bolt, R. M., Bond, T. C., Dawidowski, L., Kholod, N., Kurokawa, J.-i., Li, M., Liu, L., Lu, Z., Moura, M. C. P., Zhang, Q., Goldstein, B., and Muwan, P.: CEDS v_2019_12_23 Emission Data, doi:10.5281/ZENODO.3606753, 2020.

Keeling, R. F., Manning, A. C., McEvoy, E. M., and Shertz, S. R.: Methods for measuring changes in atmospheric O2 concentration and their application in southern hemisphere air, Journal of Geophysical Research, 103, 3381–3397, doi:10.1029/97JD02537, 1998.

Keeling, R. F., Blaine, T., Paplawsky, B., Katz, L., Atwood, C., and Brockwell, T.: Measurement of changes in atmospheric Ar/N_2 ratio using a rapid-switching, single-capillary mass spectrometer system, Tellus, 56B, 322–338, doi:10.1111/j.1600-0889.2004.00117.x, 2004.

Keeling, R. F., Manning, A. C., Paplawsky, W. J., and Cox, A. C.: On the long-term stability of reference gases for atmospheric O2/N2 and CO2 measurements,

Tellus B: Chemical and Physical Meteorology, 59B, 3–14, doi:10.1111/j.1600-0889.2006.00196.x, 2007.

Kockarts, G.: Helium in the terrestrial atmosphere, Space Science Reviews, 14, 723–757, doi:10.1007/BF00224775, 1973.

Kulongoski, J. T., Hilton, D. R., and Izbicki, J. A.: Source and movement of helium in the eastern Morongo groundwater Basin: The influence of regional tectonics on crustal and mantle helium fluxes, Geochimica et Cosmochimica Acta, 69, 3857–3872, doi:10.1016/j.gca.2005.03.001, 2005.

Kulongoski, J. T., Hilton, D. R., Cresswell, R. G., Hostetler, S., and Jacobson, G.: Helium-4 characteristics of groundwaters from Central Australia: Comparative chronology with chlorine-36 and carbon-14 dating techniques, Journal of Hydrology, 348, 176–194, doi:10.1016/j.jhydrol.2007.09.048, 2008.

Lupton, J. and Evans, L.: The atmospheric helium isotope ratio: Is it changing?, Geophysical Research Letters, 31, 1–4, doi:10.1029/2004GL020041, 2004.

Lupton, J. and Evans, L.: Changes in the atmospheric helium isotope ratio over the past 40 years, Geophysical Research Letters, 40, 6271–6275, doi:10.1002/2013GL057681, 2013.

Mabry, J. C., Lan, T., Boucher, C., Burnard, P. G., Brennwald, M. S., Langenfelds, R., and Marty, B.: No evidence for change of the atmospheric helium isotope composition since 1978 from re-analysis of the Cape Grim Air Archive, Earth and Planetary Science Letters, 428, 134–138, doi:10.1016/j.epsl.2015.07.035, 2015.

Mohr, S. and Ward, J.: Helium production and possible projection, Minerals, 4, 130–144, doi:10.3390/min4010130, 2014.

Mühle, J., Ganesan, A. L., Miller, B. R., Salameh, P. K., Harth, C. M., Greally, B. R., Rigby, M., Porter, L. W., Steele, L. P., Trudinger, C. M., Krummel,

P. B., O'Doherty, S., Fraser, P. J., Simmonds, P. G., Prinn, R. G., and Weiss, R. F.: Perfluorocarbons in the global atmosphere: Tetrafluoromethane, hexafluoroethane, and octafluoropropane, Atmospheric Chemistry and Physics, 10, 5145–5164, doi:10.5194/acp-10-5145-2010, 2010.

Oliver, B. M., Bradley, J. G., and Farrar IV, H.: Helium concentration in the Earth's lower atmosphere, Geochimica et Cosmochimica Acta, 48, 1759–1767, doi:10.1016/0016-7037(84)90030-9, 1984.

Pierson-Wickmann, A. C., Marty, B., and Ploquin, A.: Helium trapped in historical slags: A search for temporal variation of the He isotopic composition of air, Earth and Planetary Science Letters, 194, 165–175, doi:10.1016/S0012-821X(01)00554-4, 2001.

Prinn, R. G., Weiss, R. F., Fraser, P. J., Simmonds, P. G., Cunnold, D. M., Alyea, F. N., O'Doherty, S., Salameh, P., Miller, B. R., Huang, J., Wang, R. H., Hartley, D. E., Harth, C., Steele, L. P., Sturrock, G., Midgley, P. M., and McCulloch, A.: A history of chemically and radiatively important gases in air deduced from ALE/GAGE/AGAGE, Journal of Geophysical Research Atmospheres, 105, 17 751–17 792, doi:10.1029/2000JD900141, 2000.

Prinn, R. G., Weiss, R. F., Arduini, J., Arnold, T., Langley Dewitt, H., Fraser, P. J., Ganesan, A. L., Gasore, J., Harth, C. M., Hermansen, O., Kim, J., Krummel, P. B., Li, S., Loh, Z. M., Lunder, C. R., Maione, M., Manning, A. J., Miller, B. R., Mitrevski, B., Mühle, J., O'Doherty, S., Park, S., Reimann, S., Rigby, M., Saito, T., Salameh, P. K., Schmidt, R., Simmonds, P. G., Paul Steele, L., Vollmer, M. K., Wang, R. H., Yao, B., Yokouchi, Y., Young, D., and Zhou, L.: History of chemically and radiatively important atmospheric gases from the Advanced Global Atmospheric Gases Experiment (AGAGE), Earth System Science Data, 10, 985–1018, doi:10.5194/essd-10-985-2018, 2018.

Sano, Y., Wakita, H., Makide, Y., and Tominaga, T.: A ten-year decrease in the atmospheric helium isotope ratio possibly caused by human activity, Geophysical Research Letters, 16, 1371–1374, doi:10.1029/GL016i012p01371, 1989.

Sano, Y., Wakita, H., Makide, Y., and Tominaga, T.: Reply to Lupton and Graham, Geophysical Research Letters, 18, 486–4888, 1991.

Sano, Y., Furukawa, Y., and Takahata, N.: Atmospheric helium isotope ratio: Possible temporal and spatial variations, Geochimica et Cosmochimica Acta, 74, 4893–4901, doi:10.1016/j.gca.2010.06.003, 2010.

Sano, Y., Marty, B., and Burnard, P.: Noble Gases in the Atmosphere, in: The Noble Gases as Geochemical Tracers, edited by Burnard, P., pp. 17–31, Springer Berlin Heidelberg, 2nd edn., doi:10.1007/978-3-642-28836-4_2, 2013.

Torgersen, T.: Terrestrial helium degassing fluxes and the atmospheric helium budget: Implications with respect to the degassing processes of continental crust, Chemical Geology: Isotope Geoscience Section, 79, 1–14, doi:10.1016/0168-9622(89)90002-X, 1989.

Torgersen, T. and Clarke, W. B.: Helium accumulation in groundwater, I: An evaluation of sources and the continental flux of crustal 4He in the Great Artesian Basin, Australia, Geochimica et Cosmochimica Acta, 49, 1211–1218, doi:10.1016/0016-7037(85)90011-0, 1985.

Wada, Y. and Bierkens, M. F.: Sustainability of global water use: Past reconstruction and future projections, Environmental Research Letters, 9, doi:10.1088/1748-9326/9/10/104003, 2014.

York, D., Evensen, N. M., Martıinez, M. L., and De Basabe Delgado, J.: Unified equations for the slope, intercept, and standard errors of the best straight line, American Journal of Physics, 72, 367–375, doi:10.1119/1.1632486, 2004.

Zartman, R. E., Wasserburg, G. J., and Reynolds, J. H.: Helium, Argon, and Carbon in Some Natural Gases, Journal of Geophysical Research, 66, 277–306, doi:10.1029/jz066i001p00277, 1961.